Osaka University
graduate school of science

Doctoral Thesis

New insight into α clustering from knockout reaction analysis

---

Kazuki Yoshida

Research Center for Nuclear Physics (RCNP), Osaka University
Ibaraki, Osaka 567-0047, Japan

Defended on February 6, 2018

Supervisor:	Kazuyuki Ogata	RCNP
Chief Examiner:	Atsushi Hosaka	RCNP
Examiners:	Nomachi Masaharu	RCNP/Department of Physics
	Nori Aoi	RCNP
	Noriyoshi Ishii	RCNP
	Atsushi Tamii	RCNP

For my family

"*Now, here, you see, it takes all the running you can do, to keep in the same place. If you want to get somewhere else, you must run at least twice as fast as that!* "

–*The Red queen*, *Through the Looking Glass*, Lewis Carroll.

abstract

The proton (p) induced nucleon (N) or α knockout reactions, i.e., (p,pN) and (p,$p\alpha$), have been utilized as a probe for the single particle and α cluster states of nuclei. However, the validation of the distorted wave impulse approximation (DWIA) framework, which have been widely applied to those reaction analyses, is not yet done enough. In addition, how the single particle and α cluster wave functions are probed through the knockout reaction observables is not clearly shown.

One of the purpose of this thesis is to test the validity of the DWIA framework by comparing more sophisticated reaction models. In this purpose, knockout cross section obtained by DWIA is compared with the transfer-to-the-continuum (TC) model and the Faddeev/Alt-Grassberger-Sandhas (FAGS) calculations. As a result, the DWIA result agrees fairly well with both TC and FAGS results, and shown to be valid for the nucleon and α spectroscopy of nuclei. It has been also shown that the energy dependence of the distorting potentials gives a little difference in the knockout cross sections. On the other hand, it is shown that the relativistic treatment of the kinematics is essential for the quantitative discussion.

As for the α clustering studies, considering the *dual nature* of the shell model and cluster model wave functions, it is essential to probe the cluster amplitude at the nuclear surface. In this point of view, another purpose of this study is to reveal how the α cluster wave functions are reflected to the reaction observables, and how one can probe those states through the knockout reaction cross sections. For this purpose, a new concept, *the masking function*, is defined in this thesis. It clearly shows how the α cluster wave function is probed via the knockout reaction. Through the analyses on the masking function of the ^{20}Ne(p,$p\alpha$)^{16}O reaction, it is clearly shown that the cluster amplitude around the nuclear surface is safely probed through the α knockout reaction. The ^{120}Sn(p,$p\alpha$)^{116}Cd reaction is also investigated as an extreme case of the strong absorption. Through the investigations on the 1- and 2-dimensional knockout reaction amplitude, it is shown that the reaction has the sensitivity not only to the range but also the direction of the emitted α. In other words, α particle is knocked out from the limited region of the surface of the target nucleus in which direction the α is emitted. The ^{10}Be(p,$p\alpha$)^{6}He reaction is also investigated. In this study a cluster model wave function called the Tohsaki-Horiuchi-Schuck-Röpke (THSR) wave function is adopted as ^{10}Be and ^{6}He wave functions. Benefiting the flexibility of THSR wave function, the α knockout cross sections from the shell-like to gas-like states of ^{10}Be have been calculated. As a result, it is shown that one may safely distinguish how much the 2α cluster state is developed in ^{10}Be from the ^{10}Be(p,$p\alpha$)^{6}He cross section.

As a conclusion, the DWIA framework has been validated through the comparison with more sophisticated reaction theories. A new concept named masking function shows that one can define how the surface amplitude of the cluster wave function is probed through the knockout reactions, which is the essential feature for probing the spatially developed α cluster states. The knockout reaction is shown to be a good probe for the α clustering.

Acknowledgements

First of all, I express my biggest gratitude to my supervisor, Prof. Kazuyuki Ogata, for leading me to the researches on the nuclear reaction theories, and for his education with great patience. None of the works in this thesis would have been accomplished without his guidance. I am deeply thankful for Prof. Yoshiko Kanada-En'yo, Prof. Antonio M. Moro, Dr. Mengjiao Lyu, Mr. Mario Gómez-Ramos, and Mr. Yoshiki Chazono for very fruitful collaboration researches.

I appreciate Prof. Atsushi Hosaka and Prof. Noriyoshi Ishii for their broad view and knowledge across the neighboring fields of physics and valuable suggestions and comments on my research. I am very grateful to Prof. Kosho Minomo and Dr. Tokuro Fukui for teaching me the fundamental of the nuclear physics and how to proceed the research, as colleagues of our research group. I am very thankful for all staff members of the theory group at Research Center for Nuclear Physics (RCNP), especially for our secretaries Ms. Mika Tambara and Ms. Sachiko Karasuyama for providing me the comfortable and peaceful environment for the research. I was very happy to share my research life with my colleagues and students in the theory group at RCNP.

I would like to thank the financial support by RCNP and the Japan Society for the Promotion of Science (JSPS). The researches in this thesis are supported in part by Grant-in-Aid of the JSPS Fellowship (Grant No. 15J01392).

Finally, I would like to express special thanks to my parents, Nobuo and Atsuko, for always being supportive and for telling me the wonders of nature.

Kazuki Yoshida

Contents

List of Figures

List of Symbols

$\boldsymbol{R}$	Coordinate
$\boldsymbol{K}$	Momentum (wave number)
$\boldsymbol{L}$	Orbital angular momentum
M	z-projection of $\boldsymbol{L}$
$\boldsymbol{s}$	Spin, especially when $s = 1/2$
$\boldsymbol{J}$	Total angular momentum
I_i	Spin of particle i
μ_i	z-projection of I_i
$\mu_{i,\boldsymbol{r}}$	Projection of I_i along the direction of $\boldsymbol{r}$
h	Helicity
t_i	Isospin of particle i
ν_i	z-projection of t_i
$\eta_{I\mu}$	Spin wave function with spin I and its projection μ
$\zeta_{t\nu}$	Isospin wave function with isospin t and its projection ν
$\phi_{\boldsymbol{K}}$	Plane wave with asymptotic momentum of $\boldsymbol{K}$
$\chi^{\mu}_{\boldsymbol{K}}$	Distorted wave with asymptotic momentum of $\boldsymbol{K}$ and spin projection μ
ψ	Overlap of two states
φ_{nljm}	single-particle (or cluster) wave function with quantum numbers $nljm$
n	Principal quantum number of single-particle wave function
l	orbital angular momentum of single-particle wave function
j	total angular momentum of single-particle wave function
m	z-projection of l
μ_j	z-projection of j
S_i	Separation energy of particle $i = p, n, \alpha$
Ψ	Total wave function of a system
U_{ij}	Optical potential between particle i and j
P_L	Legendre polynomial of Lth order
Y_{LM}	Spherical harmonics
$D^{J}_{MM'}$	Wigner's D-matrix (See Appendix B)

Chapter 1

Introduction

1.1 Cluster picture of nuclei

One of the successful pictures of nuclei is the liquid drop model introduced by C. F. von Weizsäcker and H. A. Bethe [1, 2]. Their semi-empirical mass formula well explained the global trend of stable nuclei, e.g., the density and energy saturation properties. It also reproduced the β stability line of the nuclear chart. On the other hand, the liquid drop model fails to reproduce the magic numbers of nuclei, in which the nuclei are extraordinary stable. The magic numbers were explained by the shell model introduced by M. G. Mayer and J. H. D. Jensen [3–7]. Completely different from the liquid drop model, the shell model picture is very similar to that of the electron in the atomic systems. Nucleons in a nucleus are considered as independent particles moving in a one-body potential made by the nucleus. By adding the spin-orbit interaction to the central potential, they succeeded in reproducing the magic numbers. The nucleon spectroscopy based on this single-particle picture is one of the subjects in the nuclear physics. In Chap. 7 the current status of the nucleon spectroscopy through the nucleon knockout reactions is discussed.

In contrast to the shell-like picture of nuclei, the molecular-like picture has been successfully adopted to the nuclear structures. The idea of this picture arises from the fact that a nucleus breaks up into several subunits (clusters) of nuclei instead of breaking apart into nucleons by adding small energy. Based on this fact, in the molecular-like (cluster) picture, a nucleus is assumed to consist of several clusters instead of the nucleon degrees of freedom. Such cluster states are expected to be developed when the nucleons in each cluster are strongly bound forming a robust cluster, and the interactions (correlations) between the clusters are relatively weak.

A typical subunit in the nuclear physics is the α particle since nucleons are easily assembled to form the α particle which is a deeply bound system of two protons and two neutrons. From 1960s, α cluster states are found through nuclear reactions, in the light mass region in particular. ^{8}Be is a well known nucleus for α clustering. As shown in Fig. 1.1, the ground state of ^{8}Be has the 2α cluster structure because its ground state energy is located near the threshold energy to $\alpha + \alpha$. Furthermore, it is known that by adding neutrons to ^{8}Be, the valence neutrons play the role as the covalent bond between the 2α. In this point of view, systematic change in the cluster states of Be isotopes is interesting. In Chap. 6 the possibility of probing the size of the ^{10}Be (the distance between the 2α) with the α knockout cross sections is shown.

Not only in Be isotopes but also for various light nuclei the cluster states emerge when the energy of the nucleus is near the threshold energy to break up into the clusters. This is called the threshold energy rule. Based on this rule, the so-called Ikeda diagram, a schematic drawing of the cluster states of light nuclei is shown in Ref. [8]. It is still a question how far below the threshold the cluster states can be found, in the ground state in particular.

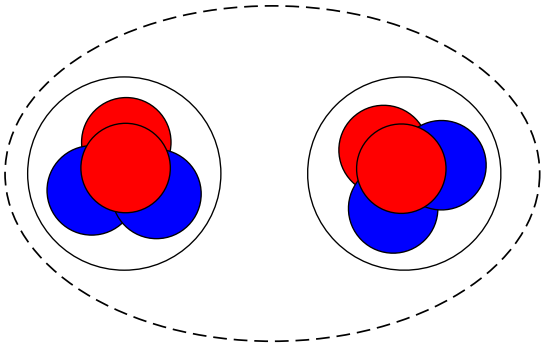

FIGURE 1.1: 2α cluster structure of ^{8}Be.

As shown in Fig. 1.2, it is known that in the α-α interaction there exists the so-called structural repulsive core [9] when the α-α distance is below about 1.8 fm, the region where 2α touch each other. This is because the α particle is made of nucleons,

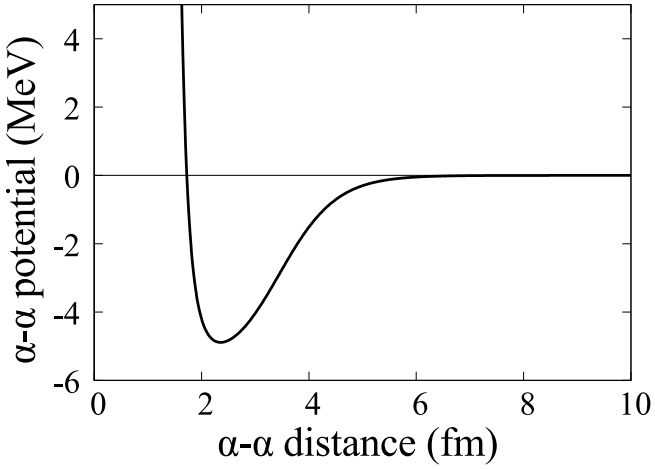

FIGURE 1.2: Shape of α-α potential.

and those in the α clusters cannot occupy the same state due to the Pauli principle. Because of this Pauli blocking (antisymmetrization) effect, the α clusters in short distance will *melt* and the cluster wave function may not have meaningful amplitude in the nuclear interior.

Another question in the cluster physics is that how much heavy mass region the cluster states appear. Recently, α cluster states of Sn isotopes have been theoretically predicted by S. Typel [10]. This prediction itself is interesting to see if the α cluster state can be formed in such heavy nuclei. Furthermore, this result may leave a significant effect on the nuclear equation of state, as discussed in Ref. [10]. The author suggested that the α particle abundance on the nuclear surface of Sn will be studied experimentally by the α knockout reactions. In order to answer to this suggestion, in chap. 4 the ^{120}Sn$(p,p\alpha)^{116}$Cd reaction is investigated to see how the α cluster amplitude on the surface of ^{120}Sn can be probed through the α knockout reaction.

Cluster models have been developed for decades. Recently, a cluster model called Tohsaki-Horiuchi-Schuck-Röpke (THSR) wave function [11] has been updated to describe not only $N\alpha$ nuclei but also nuclei consisting of α particles and valence neutrons. This model is adopted to the ^{10}Be$(p,p\alpha)^{6}$He studies in Chap. 6. There exist the microscopic cluster models, e.g., antisymmetrized molecular dynamics (AMD) [12–17] and fermionic molecular dynamics (FMD) [18–22]. In the AMD and FMD frameworks the

cluster states are constructed by the variational method based on the nucleon degrees of freedom. In this sense these models are more than the cluster model. Recently, the *ab initio* calculations also have been succeeded in describing the cluster states of light nuclei. More details on the cluster studies can be found in the Refs. [23–25].

Before moving on to the knockout reaction part, it should be noted that the shell model and the cluster model are not completely different pictures each other. As emphasized in Ref [23], according to the Bayman-Bohr theorem [26], the ground state wave function has the *dual* nature of both models; the $SU(3)$ shell model wave function for the ground state can be rewritten by the cluster wave function. In practice, however, convergence of the shell model calculation for describing the cluster states is very slow and obtaining the consistent result between the shell model and the cluster model is challenging. In Ref. [27], the authors have discussed how many quantum numbers of the harmonic oscillators are needed to describe the cluster states. It has been shown that only 66 % of the second 0^+ state of ^{12}C (3α cluster state called Hoyle state) can be described by the shell model even if the large quantum number of harmonic oscillator up to 22 is included.

1.2 knockout reactions

1.2.1 Reaction theories for knockout reactions

One of the most reliable reactions for probing the α cluster states is the proton induced α knockout reaction, i.e., (p,$p\alpha$). The schematic picture of the (p,$p\alpha$) is shown in Fig. 1.3. For describing this reaction, the distorted wave impulse approximation

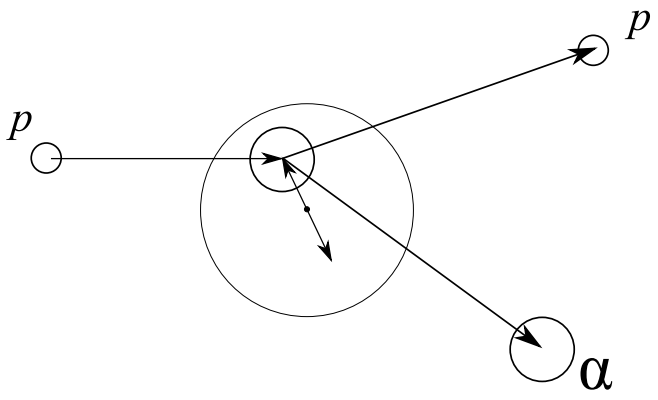

FIGURE 1.3: Schematic picture of the (p,$p\alpha$) reaction.

(DWIA) introduced in Chap. 2, has been widely applied to α knockout reaction analyses [28–35] in the same way as the nucleon knockout reactions [36–47]. The current status of the nucleon spectroscopy through the (p,pN) reaction analyses is discussed in Chap. 7. Although the DWIA framework has been widely applied to the knockout reaction analyses, it has not yet been validated enough. There only exist some preceding works [48–51] in which the DWIA calculations for the (p,pN) reaction are justified through the comparison with the Faddeev/Alt-Grassberger-Sandhas (FAGS) calculations [52–54]. The FAGS is a framework which gives the exact solution of the three-body scattering problem of a given Hamiltonian. It should be noted, however, the "DWIA" justified by the FAGS results in the preceding studies is the truncated model of the FAGS and it is different from the DWIA framework applied to the reaction analyses in practice.

Very recently, the Transfer-to-the-Continuum model (TC), which is a derivative of the continuum-discretized coupled-channels (CDCC) three-body wave function [55–57], has been developed for the description of the knockout reactions[58, 59]. Considering these situations of the reaction theories, it should be essential to test the validity and applicability of each framework. For this purpose, the benchmark of these three frameworks for the description of the (p,pN) reaction has been performed as shown in Chap. 3.

1.2.2 Knockout reaction as a probe for α clustering

One of the main subjects in this thesis is to investigate how the α cluster states are probed through nuclear reactions. As mentioned in Sec. 1.1, the α cluster may *melt* in the nuclear interior because of the Pauli blocking. Due to this effect, α cluster amplitude in the nuclear interior does not necessarily indicate the α clustering. Namely, α cluster wave function at around the center of the nucleus should not be probed with nor reflected to the reaction observables. In other words, the α cluster lying around the nuclear center is not a developed cluster state and not so much interesting. In this point of view, a direct measure of the spatially developed α cluster states, i.e., the large cluster amplitude at the nuclear surface, is in need. For this purpose, the availability of proton induced α knockout reaction, i.e., (p,$p\alpha$), is discussed in this thesis. In addition to the already mentioned α knockout reactions from ^{10}Be and ^{120}Sn, the peripherality of the ^{20}Ne(p,$p\alpha$)^{16}O reaction is investigated in Chap. 5. The masking function, which defines how the surface region of the cluster wave function is probed through the knockout reaction, is introduced.

It should be noted that the quasi-free (impulse) picture is expected to be valid in the knockout reactions. Therefore the α cluster state in the ground states can be probed through the α knockout reactions, not being affected by the coupling to the other states. This will be an advantage of the knockout reaction to other reactions in the investigation on the clustering of the ground states. As well as the (p,pN) process, the α can be treated as an inert particle during the α knockout reaction at intermediate energies. This is because α particle is a double-magic nucleus and its excited states hardly contribute to the (p,$p\alpha$) process.

1.3 Construction of the thesis

This thesis is constructed as follows. In Chap. 2, the formulation of the distorted wave impulse approximation is given in detail. The helicity formalism of the DWIA framework is also given. In Chap. 3, the validity of the DWIA framework is tested by comparing the calculated cross section of the ^{15}C(p,pn)^{14}C reaction between DWIA, the transfer-to-the-continuum model, and the Faddeev/Alt-Grassberger-Sandhas framework. The ambiguities coming from the absence of the energy dependence of the distorting potentials, and the relativistic treatment for the kinematics are also investigated. In Chap. 4, how the α cluster amplitude is probed through the ^{120}Sn(p,$p\alpha$)^{116}Cd is investigated. 1- and 2-dimensional distributions of the knockout reaction amplitude are shown. In Chap. 5, a new concept, *the masking function*, which profiles how the α cluster wave function is probed through the (p,$p\alpha$) reaction, is introduced. By applying the eikonal approximation, a simplified method to reproduce the masking function is given and the effective mean free path of the knockout reaction is defined. In Chap. 6, the ^{10}Be(p,$p\alpha$)^{6}He reaction is investigated. Tohsaki-Horiuchi-Schuck-Röpke (THSR) wave function is adopted for the description of ^{10}Be and ^{6}He and the knockout cross sections are calculated for the shell-like and gas-like cluster structures of ^{10}Be. In

Chap. 7, how one can pin down the single particle states and the spectroscopic factors through (p,pN) reactions are shown. The current status of the nucleon spectroscopy of unstable nuclei is also discussed. Finally in Chap. 8, the summary of this thesis is given.

Chapter 2

formulation

Contents

2.1 Distorted wave impulse approximation (DWIA) formalism

2.1.1 DWIA T-matrix

In this section the distorted wave impulse approximation (DWIA) formalism, which has been applied successfully to describing the A(a,a+b)B knockout reaction and its analysis, particularly to the nucleon knockout [36–47] and α knockout [28–35] reactions, is introduced.

For the latest review on (p,pN) reactions, see Ref. [60]. In the following formulation notations and labels are given in the same manner as in Ref. [60] as much as possible. In the present study the proton (p) induced nucleon (N) or α-particle (α) knockout reaction, i.e., (p,pN) and (p,$p\alpha$) are considered within a three-body reaction model. The incident proton, the emitted proton, and the knocked-out proton or α are referred to as particles 0, 1 and 2, respectively, and the target, the residue and the valence particle bound in the target are labeled as A, B and b, respectively. In Fig 2.1 the orientation of the axes for the reaction (a) and the definition of the coordinates (b) are shown.

We take the Jacobi coordinate of the 0-(2+B) system, i.e., $\boldsymbol{R}_0$ and $\boldsymbol{R}_2$ are chosen as independent coordinates. All quantities below are evaluated in the center-of-mass (G) frame unless otherwise specified. In the following, the Coulomb interaction is not discussed explicitly, but it is taken into account in the standard manner; if Coulomb interactions exists, the asymptotic behavior of scattering states is governed by the Coulomb wave function, instead of the plane wave. It should be noted, however, that one cannot handle them with the Gell-Mann-Goldberger transformation, because of

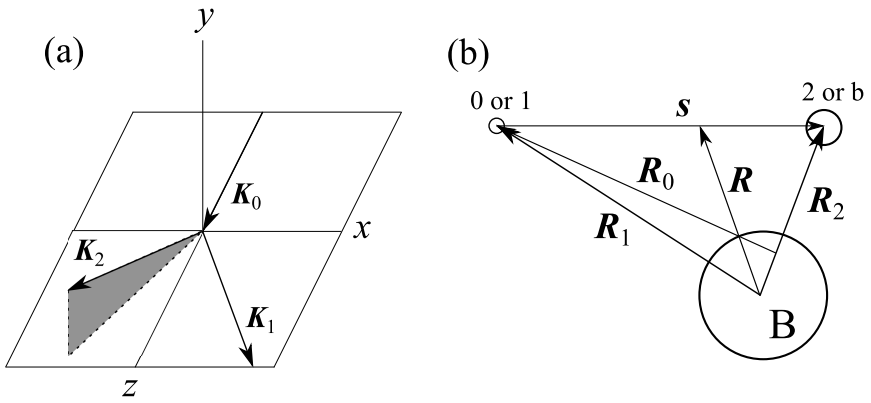

FIGURE 2.1: (a) Orientation of the axes for (p,pN) and (p,$p\alpha$) reactions. The momentum of the incident proton $\boldsymbol{K}_0$ is taken to be parallel with the z-axis and the emitted proton has its momentum $\boldsymbol{K}_1$ in the $x > 0$ region on the x-z plane. Only the momentum of the struck particle $\boldsymbol{K}_2$ is assumed to have a y-component. (b) Definition of the coordinates.

its long-range nature. The Møller operator (or often called the wave operator) does not exist for $1/R$ type Coulomb interactions.

Although the distorted wave and the transition matrix (T-matrix) in the practical calculation are described with the helicity representation, in the following discussion the ordinary quantization (here it is termed the JM representation) is taken to avoid unnecessary complications and confusions. The helicity representation of distorted waves and the T-matrix are introduced in Sec. 2.2.

The T-matrix in post form is given by

$$T_{\mu_1\mu_2\mu_{\rm B}\mu_0\mu_{\rm A}} = \left\langle \Psi^{\rm free}_{\rm 12B} \middle| V_f \Omega^{(+)}_0 \middle| \Psi^{\rm free}_{\rm 0A} \right\rangle, \tag{2.1}$$

$$\left|\Psi^{\rm free}_{\rm 0A}\right\rangle = \left|\phi_{\boldsymbol{K}_0}(\boldsymbol{R}_0)\eta^{(0)}_{1/2,\mu_0}\xi^{(0)}_{1/2,\nu_0}\Phi^{t_{\rm A}\nu_{\rm A}}_{I_{\rm A}\mu_{\rm A}}(\varepsilon_{\rm A},\xi_{\rm A})\right\rangle, \tag{2.2}$$

$$\left\langle \Psi^{\rm free}_{\rm 12B}\right| = \left\langle \phi_{\boldsymbol{K}_1}(\boldsymbol{R}_0)\eta^{(1)}_{1/2,\mu_1}\xi^{(2)}_{1/2.\nu_1}\phi_{\boldsymbol{K}_{\rm 2B}}(\boldsymbol{R}_2)\Phi^{t_2\nu_2}_{I_2\mu_2}(\varepsilon_2,\xi_2)\Phi^{t_{\rm B}\nu_{\rm B}}_{I_{\rm B}\mu_{\rm B}}(\varepsilon_{\rm B},\xi_{\rm B})\right|, \tag{2.3}$$

where $\phi_{\boldsymbol{K}_i}(\boldsymbol{R}_i)$ represents the plane wave state of particle $i = 0, 1, 2$ with respect to the coordinate $\boldsymbol{R}_i$. The momentum of particle i in the three-body G frame is denoted by $\boldsymbol{K}_i$, and $\boldsymbol{K}_{\rm 2B}$ is the relative momentum between particle 2 and B. $\eta^{(i)}_{1/2,\mu_i}$ ($\xi^{(i)}_{1/2,\nu_i}$) represents the spin (isospin) wave function of particle $i = 0, 1$ with η_i (ν_i) being the z-projection value. The internal wave function of particle $j = 2$, B, A are denoted by $\Phi^{t_j\nu_j}_{I_j\mu_j}(\varepsilon_j,\xi_j)$, where I_j, t_j, ε_j and ξ_j are the spin, isospin, eigenenergy and internal coordinates, respectively. The superscript $(\pm)$ indicates the outgoing $(+)$ and incoming $(-)$ boundary conditions of the scattering waves.

$\Omega^{(+)}_0$ is the Møller operator which generates the distorted wave of particle 0 with respect to A as

$$\Omega^{(+)}_0 \left|\Psi^{\rm free}_{\rm 0A}\right\rangle = \left|\chi^{(+)\mu_0}_{\boldsymbol{K}_0}(\boldsymbol{R}_0)\xi^{(0)}_{1/2,\nu_0}\Phi^{t_{\rm A}\nu_{\rm A}}_{I_{\rm A}\mu_{\rm A}}(\varepsilon_{\rm A},\xi_{\rm A})\right\rangle. \tag{2.4}$$

$\chi^{(+)\mu_0}_{\boldsymbol{K}_0}(\boldsymbol{R}_0)$ is the distorted wave with μ_0 in the asymptotic region satisfying the Schrödinger equation of the initial state:

$$[T_{\boldsymbol{R}_0} + U_{0\mathrm{A}} - E_i]\, \chi^{(+)\mu_0}_{0,\boldsymbol{K}_0}(\boldsymbol{R}_0) = 0, \tag{2.5}$$

$$\chi^{(+)\mu_0}_{0,\boldsymbol{K}_0}(\boldsymbol{R}_0) = \sum_{\mu_0'} \chi^{(+)\mu_0'\mu_0}_{0,\boldsymbol{K}_0}(\boldsymbol{R}_0). \tag{2.6}$$

Here, $T_{\boldsymbol{R}_0}$, $U_{0\mathrm{A}}$ and E_i are the kinetic operator, an optical potential between particle 0 and A, and the scattering energy, respectively.

The transition interaction V_f is the sum of the pair interactions in the final state:

$$V_f = U_{1\mathrm{B}} + U_{2\mathrm{B}} + \tau_{12}, \tag{2.7}$$

where $U_{1\mathrm{B}}$ ($U_{2\mathrm{B}}$) is the optical potential between particle 1 (2) and B, and τ_{12} is the effective interaction between particle 1 and 2, based on the multiple scattering theory [61].

In the DWIA framework, the impulse approximation is applied to τ_{12}, i.e., $\tau_{12} \approx t_{12}$ where t_{12} is the effective interaction in free space, e.g., the Franey-Love effective interaction [62]. Instead of t_{12}, the Melbourne g-matrix interaction [63] can be used to take into account the in-medium effect on τ_{12}.

Since $U_{1\mathrm{B}}$ ($U_{2\mathrm{B}}$) is an optical potential corresponding to the coordinate $\boldsymbol{R}_1$ ($\boldsymbol{R}_2$), rewriting the product of the plane waves in the finial state as

$$\phi_{\boldsymbol{K}_1}(\boldsymbol{R}_0)\phi_{\boldsymbol{K}_{2\mathrm{B}}}(\boldsymbol{R}_2) = \frac{1}{(2\pi)^3}\exp\left[i\boldsymbol{K}_1\cdot\boldsymbol{R}_0\right]\exp\left[i\boldsymbol{K}_{2\mathrm{B}}\cdot\boldsymbol{R}_2\right] \tag{2.8}$$

$$= \frac{1}{(2\pi)^3}\exp\left[i\boldsymbol{K}_1\cdot\left(\boldsymbol{R}_1 - \frac{M_2}{M_2+M_\mathrm{B}}\boldsymbol{R}_2\right)\right] \times \exp\left[i\left(\frac{M_2}{M_2+M_\mathrm{B}}\boldsymbol{K}_1 + \boldsymbol{K}_2\right)\cdot\boldsymbol{R}_2\right] \tag{2.9}$$

$$= \frac{1}{(2\pi)^3}\exp\left[i\boldsymbol{K}_1\cdot\boldsymbol{R}_1\right]\exp\left[i\boldsymbol{K}_2\cdot\boldsymbol{R}_2\right] \tag{2.10}$$

$$= \phi_{\boldsymbol{K}_1}(\boldsymbol{R}_1)\phi_{\boldsymbol{K}_2}(\boldsymbol{R}_2) \tag{2.11}$$

helps the following discussion.

Applying the Gell-Mann-Goldberger transformation shown in Appendix A, $U_{1\mathrm{B}}$ and $U_{2\mathrm{B}}$ are consumed to distort the final state as

$$T_{\mu_1\mu_2\mu_\mathrm{B}\mu_0\mu_\mathrm{A}} = \left\langle \Psi^{(-)\mu_1\mu_2}_{\boldsymbol{K}_1\boldsymbol{K}_2}(\boldsymbol{R}_1,\boldsymbol{R}_2)\xi^{(1)}_{1/2,\nu_1}\Phi^{t_2\nu_2}_{I_2\mu_2}(\varepsilon_2,\xi_2)\Phi^{t_\mathrm{B}\nu_\mathrm{B}}_{I_\mathrm{B}\mu_\mathrm{B}}(\varepsilon_\mathrm{B},\xi_\mathrm{B}) \times \left|\tau_{12}\right|\chi^{(+)\mu_0}_{\boldsymbol{K}_0}(\boldsymbol{R}_0)\Phi^{t_\mathrm{A}\nu_\mathrm{A}}_{I_\mathrm{A}\mu_\mathrm{A}}(\varepsilon_\mathrm{A},\xi_\mathrm{A})\right\rangle, \tag{2.12}$$

where the scattering state $\Psi^{(-)\mu_1\mu_2}_{\boldsymbol{K}_1\boldsymbol{K}_2}(\boldsymbol{R}_1,\boldsymbol{R}_2)$ satisfies the three-body Schrödinger equation

$$[T_{\boldsymbol{R}_1} + T_{\boldsymbol{R}_2} + T_\mathrm{coup} + U^*_{1\mathrm{B}}(\boldsymbol{R}_1) + U^*_{2\mathrm{B}}(\boldsymbol{R}_2) - E_f]\, \Psi^{*(-)\mu_1\mu_2}_{\boldsymbol{K}_1\boldsymbol{K}_2}(\boldsymbol{R}_1,\boldsymbol{R}_2) = 0. \tag{2.13}$$

By using $\boldsymbol{K}_1 + \boldsymbol{K}_2 + \boldsymbol{K}_\mathrm{B} = 0$, which is the definition of the G frame, E_f can be rewritten as

$$E_f = \frac{\hbar^2}{2m_1}K_1^2 + \frac{\hbar^2}{2m_2}K_2^2 + \frac{\hbar^2}{2m_\mathrm{B}}K_\mathrm{B}^2 \tag{2.14}$$

$$= \frac{\hbar^2}{2\mu_{1\mathrm{B}}}K_1^2 + \frac{\hbar^2}{2\mu_{2\mathrm{B}}}K_2^2 + \frac{\hbar^2}{m_\mathrm{B}}\boldsymbol{K}_1\cdot\boldsymbol{K}_2, \tag{2.15}$$

where μ_{ij} is the reduced mass of particles i and j. The kinetic operators in Eq. (2.13) are defined by

$$T_{\boldsymbol{R}_1} = -\frac{\hbar^2}{2\mu_{1\mathrm{B}}}\boldsymbol{\nabla}^2_{\boldsymbol{R}_1}, \qquad T_{\boldsymbol{R}_2} = -\frac{\hbar^2}{2\mu_{2\mathrm{B}}}\boldsymbol{\nabla}^2_{\boldsymbol{R}_2}, \qquad T_\mathrm{coup} = -\hbar^2\frac{\boldsymbol{\nabla}_{\boldsymbol{R}_1}\cdot\boldsymbol{\nabla}_{\boldsymbol{R}_2}}{m_\mathrm{B}}, \tag{2.16}$$

which can be obtained as follows. Denoting the position of particle i by $\boldsymbol{r}_i$, one can easily find

$$\boldsymbol{R}_1 = \boldsymbol{r}_1 - \boldsymbol{r}_\mathrm{B}, \tag{2.17}$$

$$\boldsymbol{R}_2 = \boldsymbol{r}_2 - \boldsymbol{r}_\mathrm{B}, \tag{2.18}$$

$$\boldsymbol{R}_\mathrm{c.m.} = \frac{m_1\boldsymbol{r}_1 + m_2\boldsymbol{r}_2 + m_\mathrm{B}\boldsymbol{r}_\mathrm{B}}{m_\mathrm{tot}}, \tag{2.19}$$

where $m_\mathrm{tot} = m_1 + m_2 + m_\mathrm{B}$. Therefore

$$\boldsymbol{\nabla}_{\boldsymbol{r}_1} = \boldsymbol{\nabla}_{\boldsymbol{R}_1} + \frac{m_1}{m_\mathrm{tot}}\boldsymbol{\nabla}_{\boldsymbol{R}_\mathrm{c.m.}}, \tag{2.20}$$

$$\boldsymbol{\nabla}_{\boldsymbol{r}_2} = \boldsymbol{\nabla}_{\boldsymbol{R}_2} + \frac{m_2}{m_\mathrm{tot}}\boldsymbol{\nabla}_{\boldsymbol{R}_\mathrm{c.m.}}, \tag{2.21}$$

$$\boldsymbol{\nabla}_{\boldsymbol{r}_\mathrm{B}} = -\boldsymbol{\nabla}_{\boldsymbol{R}_1} - \boldsymbol{\nabla}_{\boldsymbol{R}_2} + \frac{m_\mathrm{B}}{m_\mathrm{tot}}\boldsymbol{\nabla}_{\boldsymbol{R}_\mathrm{c.m.}}, \tag{2.22}$$

and hence the kinetic operators in the final state in the G frame are given by

$$T_{\boldsymbol{r}_1} + T_{\boldsymbol{r}_2} + T_{\boldsymbol{r}_\mathrm{B}} - T_\mathrm{c.m.} = -\frac{\hbar^2\nabla^2_{\boldsymbol{r}_1}}{2m_1} - \frac{\hbar^2\nabla^2_{\boldsymbol{r}_2}}{2m_2} - \frac{\hbar^2\nabla^2_{\boldsymbol{r}_\mathrm{B}}}{2m_\mathrm{B}} + \frac{\hbar^2\nabla^2_{\boldsymbol{R}_\mathrm{c.m.}}}{2m_\mathrm{tot}} \tag{2.23}$$

$$= T_{\boldsymbol{R}_1} + T_{\boldsymbol{R}_2} + T_\mathrm{coup}, \tag{2.24}$$

where $T_\mathrm{c.m.}$ is the kinetic operator responsible for the center-of-mass (c.m.) motion.

Instead of solving Eq. (2.13) within the three-body Faddeev theory [52–54], the following semiclassical approximation is commonly adopted to T_coup to solve the problem effectively [38, 64]:

$$T_\mathrm{coup} \approx \hbar^2\frac{\boldsymbol{K}_1\cdot\boldsymbol{K}_2}{m_\mathrm{B}} \tag{2.25}$$

The uncertainty coming from this approximation can be neglected in many cases if m_B is sufficiently large. Equation (2.13) is then decoupled by Eq. (2.25) as

$$\Psi^{(-)\mu_1\mu_2}_{\boldsymbol{K}_1\boldsymbol{K}_2}(\boldsymbol{R}_1,\boldsymbol{R}_2) \approx \chi^{(-)\mu_1}_{1,\boldsymbol{K}_1}(\boldsymbol{R}_1)\chi^{(-)\mu_2}_{2,\boldsymbol{K}_2}(\boldsymbol{R}_2), \tag{2.26}$$

where

$$\left[T_{\boldsymbol{R}_1} + U^*_{1\mathrm{B}}(\boldsymbol{R}_1) - \frac{\hbar^2 K_1^2}{2\mu_{1\mathrm{B}}}\right] \chi^{(-)\mu_1}_{1,\boldsymbol{K}_1}(\boldsymbol{R}_1) = 0, \tag{2.27}$$

$$\left[T_{\boldsymbol{R}_2} + U^*_{2\mathrm{B}}(\boldsymbol{R}_2) - \frac{\hbar^2 K_2^2}{2\mu_{2\mathrm{B}}}\right] \chi^{(-)\mu_2}_{2,\boldsymbol{K}_2}(\boldsymbol{R}_2) = 0, \tag{2.28}$$

$$\chi^{(-)\mu_1}_{1,\boldsymbol{K}_1}(\boldsymbol{R}_1) = \sum_{\mu_1'} \chi^{(-)\mu_1'\mu_1}_{1,\boldsymbol{K}_1}(\boldsymbol{R}_1), \tag{2.29}$$

$$\chi^{(-)\mu_2}_{2,\boldsymbol{K}_2}(\boldsymbol{R}_2) = \sum_{\mu_2'} \chi^{(-)\mu_2'\mu_2}_{2,\boldsymbol{K}_2}(\boldsymbol{R}_2). \tag{2.30}$$

The distorted waves in the final state, $\chi^{(-)\mu_1}_{1,\boldsymbol{K}_1}$ and $\chi^{(-)\mu_2}_{2,\boldsymbol{K}_2}$, can be obtained in the similar manner to for $\chi^{(+)\mu_0}_{0,\boldsymbol{K}_0}$ but with the incoming boundary condition.

Now the T-matrix has the form

$$\begin{aligned} T_{\mu_1\mu_2\mu_\mathrm{B}\mu_0\mu_\mathrm{A}} = &\left\langle \chi^{(-)\mu_1}_{1,\boldsymbol{K}_1}(\boldsymbol{R}_1)\chi^{(-)\mu_2}_{2,\boldsymbol{K}_2}(\boldsymbol{R}_2)\xi^{(1)}_{1/2,\nu_1}\Phi^{t_2\nu_2}_{I_2\mu_2}(\varepsilon_2,\xi_2)\Phi^{t_\mathrm{B}\nu_\mathrm{B}}_{I_\mathrm{B}\mu_\mathrm{B}}(\varepsilon_\mathrm{B},\xi_\mathrm{B})\right. \\ &\times \left. \left| t_{12} \right| \chi^{(+)\mu_0}_{\boldsymbol{K}_0}(\boldsymbol{R}_0)\xi^{(0)}_{1/2,\nu_0}\Phi^{t_\mathrm{A}\nu_\mathrm{A}}_{I_\mathrm{A}\mu_\mathrm{A}}(\varepsilon_\mathrm{A},\xi_\mathrm{A})\right\rangle . \end{aligned} \tag{2.31}$$

Here the following assumptions are made in the DWIA framework.

1. B is inert and a spectator during the reaction,
2. When (p,$p\alpha$) reaction is considered, both particle 2 and b are approximated by the ground state of α in free space.

Equation (2.31) is then reduced to

$$\begin{aligned} T_{\mu_1\mu_2\mu_\mathrm{B}\mu_0\mu_\mathrm{A}} = &\left\langle \chi^{(-)\mu_1}_{1,\boldsymbol{K}_1}(\boldsymbol{R}_1)\chi^{(-)\mu_2}_{2,\boldsymbol{K}_2}(\boldsymbol{R}_2)\xi^{(1)}_{1/2,\nu_1}\right. \\ &\times \left. \left| t_{12} \right| \chi^{(+)\mu_0}_{\boldsymbol{K}_0}(\boldsymbol{R}_0)\xi^{(0)}_{1/2,\nu_0}\psi^{t_2\nu_2 t_\mathrm{B}\nu_\mathrm{B},t_\mathrm{A}\nu_\mathrm{A}}_{I_2\mu_2 I_\mathrm{B}\mu_\mathrm{B},I_\mathrm{A}\mu_\mathrm{A}}(\boldsymbol{R}_2)\right\rangle , \end{aligned} \tag{2.32}$$

where $\psi^{t_2\nu_2 t_\mathrm{B}\nu_\mathrm{B},t_\mathrm{A}\nu_\mathrm{A}}_{I_2\mu_2 I_\mathrm{B}\mu_\mathrm{B},I_\mathrm{A}\mu_\mathrm{A}}$ is the overlap between A and the (B+b) system,

$$\psi^{t_2\nu_2 t_\mathrm{B}\nu_\mathrm{B},t_\mathrm{A}\nu_\mathrm{A}}_{I_2\mu_2 I_\mathrm{B}\mu_\mathrm{B},I_\mathrm{A}\mu_\mathrm{A}}(\boldsymbol{R}_2) = \left\langle \Phi^{t_2\nu_2}_{I_2\mu_2}(\varepsilon_2,\xi_2)\Phi^{t_\mathrm{B}\nu_\mathrm{B}}_{I_\mathrm{B}\mu_\mathrm{B}}(\varepsilon_\mathrm{B},\xi_\mathrm{B}) \,\middle|\, \Phi^{t_\mathrm{A}\nu_\mathrm{A}}_{I_\mathrm{A}\mu_\mathrm{A}}(\varepsilon_\mathrm{A},\xi_\mathrm{A})\right\rangle . \tag{2.33}$$

One can expand $\Phi^{t_\mathrm{A}\mu_\mathrm{A}}_{I_\mathrm{A}\mu_\mathrm{A}}$ by $\{\Phi^{t_\mathrm{b}\nu_\mathrm{b}}_{I_\mathrm{b}\mu_\mathrm{b}}\}$ and $\{\Phi^{t_\mathrm{B}\nu_\mathrm{B}}_{I_\mathrm{B}\mu_\mathrm{B}}\}$, sets of eigenstates of b and B, respectively, with a coefficient $\vartheta^{nlj\nu_\mathrm{b}}_{I'_\mathrm{B}t'_\mathrm{B}\nu'_\mathrm{B};I_\mathrm{A}t_\mathrm{A}\nu_\mathrm{A}}$ as

$$\begin{aligned} \Phi^{t_\mathrm{A}\nu_\mathrm{A}}_{I_\mathrm{A}\mu_\mathrm{A}}(\varepsilon_\mathrm{A},\xi_\mathrm{A}) = &\sum\!\!\!\!\!\!\int_{\varepsilon_\mathrm{b}} \sum\!\!\!\!\!\!\int_{\varepsilon'_\mathrm{B}} \sum_{t_\mathrm{b}\nu_\mathrm{b}} \sum_{t'_\mathrm{B}\nu'_\mathrm{B}} \left(t'_\mathrm{B}\nu'_\mathrm{B}t_\mathrm{b}\nu_\mathrm{b}\middle|t_\mathrm{A}\nu_\mathrm{A}\right) \\ &\times \sum_{I_\mathrm{b}\mu_\mathrm{b}} \sum_{I'_\mathrm{B}\mu'_\mathrm{B}} \sum_{lj\mu_j} \vartheta^{nlj\nu_\mathrm{b}}_{I'_\mathrm{B}t'_\mathrm{B}\nu'_\mathrm{B};I_\mathrm{A}t_\mathrm{A}\nu_\mathrm{A}} \\ &\times \varphi_{nlj}(R_2)\left[Y_l(\hat{\boldsymbol{R}}_2)\otimes\Phi^{t_\mathrm{b}\nu'_\mathrm{b}}_{I_\mathrm{b}}(\varepsilon_\mathrm{b},\xi_\mathrm{b})\right]_{j\mu_j} \\ &\times \left(j\mu_j I'_\mathrm{B}\mu'_\mathrm{B}\middle|I_\mathrm{A}\mu_A\right)\Phi^{t'_\mathrm{B}\nu'_\mathrm{B}}_{I'_\mathrm{B}\mu'_\mathrm{B}}(\varepsilon'_\mathrm{B},\xi_\mathrm{B}), \end{aligned} \tag{2.34}$$

where

$$\left[Y_l(\hat{\boldsymbol{R}}_2)\otimes\Phi^{t_\mathrm{b}\nu'_\mathrm{b}}_{I_\mathrm{b}}(\varepsilon_\mathrm{b},\xi_\mathrm{b})\right]_{j\mu_j}\equiv\sum_{m\mu'_\mathrm{b}}\left(lmI_\mathrm{b}\mu'_\mathrm{b}|j\mu_j\right)Y_{lm}(\hat{\boldsymbol{R}}_2)\Phi^{t_\mathrm{b}\nu'_\mathrm{b}}_{I_\mathrm{b}\mu'_\mathrm{b}}(\varepsilon_\mathrm{b},\xi_\mathrm{b}). \tag{2.35}$$

$(abcd|ef)$ and Y_{lm} are the Clebsch-Gordan coefficient and the spherical harmonics, respectively. See Ref. [65] for the details. The single-particle (or cluster) state of b bound in A is characterized by the principal quantum number n, the orbital angular momentum $\boldsymbol{l}$, the total angular momentum $\boldsymbol{j}=\boldsymbol{l}+\boldsymbol{I}_\mathrm{b}$, and its projection μ_j.

Combining Eqs. (2.33) and (2.35), the T-matrix is reduced to

$$\begin{aligned}T_{\mu_1\mu_2\mu_\mathrm{B}\mu_0\mu_\mathrm{A}}=\Big\langle&\chi^{(-)\mu_1}_{1,\boldsymbol{K}_1}(\boldsymbol{R}_1)\chi^{(-)\mu_2}_{2,\boldsymbol{K}_2}(\boldsymbol{R}_2)\xi^{(1)}_{1/2,\nu_1}\Phi^{t_2\nu_2}_{I_2\mu_2}(\varepsilon_2,\xi_2)\\&\times|t_{12}|\,\chi^{(+),\mu_0}_{\boldsymbol{K}_0}(\boldsymbol{R}_0)\xi^{(0)}_{1/2,\nu_0}\sum_{lj\mu_j}S^{1/2}_{nlj\nu_\mathrm{b}}\left(j\mu_jI_\mathrm{B}\mu_\mathrm{B}|I_\mathrm{A}\mu_\mathrm{A}\right)\\&\times\varphi_{nlj}(R_2)\left[Y_l(\hat{\boldsymbol{R}}_2)\otimes\Phi^{t_\mathrm{b}\nu_\mathrm{b}}_{I_\mathrm{b}}(\varepsilon_\mathrm{b},\xi_\mathrm{b})\right]_{j\mu_j}\Big\rangle,\end{aligned} \tag{2.36}$$

where

$$S^{1/2}_{nlj\nu_\mathrm{b}}\equiv\left(t_\mathrm{B}\nu_\mathrm{B}t_\mathrm{b}\nu_\mathrm{b}|t_\mathrm{A}\nu_\mathrm{A}\right)\vartheta^{nlj\nu_\mathrm{b}}_{I_\mathrm{B}t_\mathrm{B}\nu_\mathrm{B};I_\mathrm{A}t_\mathrm{A}\nu_\mathrm{A}} \tag{2.37}$$

is the spectroscopic amplitude, and its square norm is the spectroscopic factor $S_{nlj\nu_\mathrm{b}}$.

2.1.2 Triple differential cross section and momentum distribution

The infinitesimal cross section of a three-body channel is given by

$$d\sigma=\frac{(2\pi)^4}{\hbar v_i}d\boldsymbol{K}_1d\boldsymbol{K}_2\delta(E_f-E_i)\frac{1}{(2s_0+1)(2I_\mathrm{A}+1)}\sum_{\mu_1\mu_2\mu_\mathrm{B}\mu_0\mu_\mathrm{A}}|T_{\mu_1\mu_2\mu_\mathrm{B}\mu_0\mu_\mathrm{A}}|^2\,. \tag{2.38}$$

The Dirac delta function $\delta(E_f-E_i)$ guarantees the energy conservation between the initial and final states. Note that the momentum conservation of the system is already taken into account in Eq. (2.38). The spin of particle 0 is $s_0=1/2$, and its relative velocity v_i to A is given by

$$v_i=\hbar c^2\frac{K^\mathrm{L}_0}{E^\mathrm{L}_0}. \tag{2.39}$$

The quantities with superscript L are evaluated in the laboratory (L) frame.

Unless spin projection values of A and B are not specified experimentally, the summation over μ_A and μ_B leads to a simple result when the square norm of $T_{\mu_1\mu_2\mu_\mathrm{B}\mu_0\mu_\mathrm{A}}$ is taken. Since μ_A and μ_B appear only in the Clebsch-Gordan coefficient in Eq. (2.36), the relation

$$\sum_{\mu_\mathrm{A}\mu_\mathrm{B}}\left(j'\mu'_jI_\mathrm{B}\mu_\mathrm{B}|I_\mathrm{A}\mu_\mathrm{A}\right)\left(j\mu_jI_\mathrm{B}\mu_\mathrm{B}|I_\mathrm{A}\mu_\mathrm{A}\right)=\frac{2I_\mathrm{A}+1}{2j+1}\delta_{j'j}\delta_{\mu'_j\mu_j} \tag{2.40}$$

can be utilized. Equation (2.36) and (2.38) are then reduced to

$$d\sigma=\frac{(2\pi)^4}{\hbar v_i}d\boldsymbol{K}_1d\boldsymbol{K}_2\delta(E_f-E_i)\frac{1}{(2s_0+1)}\sum_{lj}\sum_{\mu_1\mu_2\mu_0\mu_j}\frac{1}{(2j+1)}\left|T_{\mu_1\mu_2\mu_0\mu_j}\right|^2, \tag{2.41}$$

where

$$T_{\mu_1\mu_2\mu_0\mu_j} = S^{1/2}_{nlj\nu_\mathrm{b}} \left\langle \chi^{(-)\mu_1}_{1,\boldsymbol{K}_1}(\boldsymbol{R}_1)\chi^{(-)\mu_2}_{2,\boldsymbol{K}_2}(\boldsymbol{R}_2)\xi^{(1)}_{1/2,\nu_1}\Phi^{t_2\nu_2}_{I_2\mu_2}(\varepsilon_2,\xi_2)\Big|t_{12}\Big| \right.$$
$$\left. \times\ \chi^{(+),\mu_0}_{\boldsymbol{K}_0}(\boldsymbol{R}_0)\xi^{(0)}_{1/2,\nu_0}\varphi_{nlj}(R_2)\left[Y_l(\hat{\boldsymbol{R}}_2)\otimes\Phi^{t_\mathrm{b}\nu_\mathrm{b}}_{I_\mathrm{b}}(\varepsilon_\mathrm{b},\xi_\mathrm{b})\right]_{j\mu_j}\right\rangle. \tag{2.42}$$

In the following, the triple differential cross section (TDX) of the form

$$\frac{d^3\sigma^\mathrm{L}}{dE^\mathrm{L}_1 d\Omega^\mathrm{L}_1 d\Omega^\mathrm{L}_2}, \tag{2.43}$$

is derived from Eq. (2.41), where E^L_i and Ω^L_i are the total energy and the solid angle of particle i in the L frame, respectively. It should be noted that dE_i is equivalent to dT_i, since the relation between E_i and its kinetic part T_i is given by

$$E_i = \sqrt{(\hbar K_i)^2 + (m_i c^2)^2} = T_i + m_i c^2. \tag{2.44}$$

Using Eq. (2.44), $d\boldsymbol{K}_i$ is reduced to

$$\begin{aligned} d\boldsymbol{K}_i &= K_i^2 dK_i d\Omega_i \\ &= K_i^2 \left(\frac{dK_i}{dE_i}\right) dE_i d\Omega_i \\ &= \frac{K_i E_i}{(\hbar c)^2} dE_1 d\Omega_i, \end{aligned} \tag{2.45}$$

hence

$$d\boldsymbol{K}_1 d\boldsymbol{K}_2 \delta(E_f - E_i) = \frac{K_1 E_1}{(\hbar c)^2} dE_1 d\Omega_1 \frac{K_2 E_2}{(\hbar c)^2} dE_2 d\Omega_2 \delta(E_f - E_i). \tag{2.46}$$

Applying the following relation of the δ function:

$$\delta(f(x)) = \frac{1}{|f'(a)|}\delta(x-a), \tag{2.47}$$

one obtains

$$\delta(E_f - E_i)dE_2 = \left[\frac{\partial(E_f - E_i)}{\partial E'_2}\right]^{-1} \delta(E_2 - E'_2)dE_2. \tag{2.48}$$

The partial differential in Eq. (2.48) can be obtained by

$$\begin{aligned}
\frac{\partial(E_f - E_i)}{\partial E_2} &= \frac{\partial}{\partial E_2}(E_1 + E_2 + E_\mathrm{B} + S_\mathrm{b} - E_i) \\
&= 1 + \frac{\partial K_2}{\partial E_2}\frac{\partial}{\partial K_2}(E_1 + E_\mathrm{B} + S_\mathrm{b} - E_i) \\
&= 1 + \frac{\partial K_2}{\partial E_2}\frac{\partial}{\partial K_2}\left(\sqrt{(m_\mathrm{B}c^2)^2 + (\hbar c)^2 K_\mathrm{B}^2}\right) \\
&= 1 + \frac{\partial K_2}{\partial E_2}\frac{\partial}{\partial K_2}\left(\sqrt{(m_\mathrm{B}c^2)^2 + (\hbar c)^2 (\boldsymbol{K}_1 + \boldsymbol{K}_2)^2}\right) \\
&= 1 + \frac{E_2}{(\hbar c)^2 K_2}\frac{1}{2E_\mathrm{B}}(\hbar c)^2(2K_2 + 2K_1\cos\theta_{12}) \\
&= 1 + \frac{E_2}{E_\mathrm{B}}\frac{K_2 + K_1\cos\theta_{12}}{K_2} \\
&= 1 + \frac{E_2}{E_\mathrm{B}}\frac{\boldsymbol{K}_1\cdot\boldsymbol{K}_2}{K_2^2},
\end{aligned} \tag{2.49}$$

where S_b and θ_{12} are the separation energy of b from A and the opening angle between $\boldsymbol{K}_1$ and $\boldsymbol{K}_2$, respectively. Note that $\boldsymbol{K}_\mathrm{B} = -(\boldsymbol{K}_1 + \boldsymbol{K}_2)$ because of in the center-of-mass system. From Eqs. (2.46) and (2.49), one obtains

$$\begin{aligned}
d\boldsymbol{K}_1\boldsymbol{K}_2\delta(E_f - E_i) &= \frac{K_1K_2E_1E_2}{(\hbar c)^4}\left[1 + \frac{E_2}{E_\mathrm{B}} + \frac{E_2}{E_\mathrm{B}}\frac{\boldsymbol{K}_1\cdot\boldsymbol{K}_2}{K_2^2}\right]^{-1} dE_1 d\Omega_1 d\Omega_2 \\
&= F_\mathrm{kin} dE_1 d\Omega_1 d\Omega_2
\end{aligned} \tag{2.50}$$

and the TDX in the G frame is given by

$$\frac{d^3\sigma}{dE_1 d\Omega_1 d\Omega_2} = F_\mathrm{kin}\frac{(2\pi)^4}{\hbar v_i}\sum_{lj}\sum_{\mu_1\mu_2\mu_0\mu_j}\frac{1}{2(2j+1)}\left|T_{\mu_1\mu_2\mu_0\mu_j}\right|^2. \tag{2.51}$$

Since experimental data are given in the L frame in general, the TDX should be converted by the Jacobian $J_{\mathrm{G}\to\mathrm{L}}$ from the L to the G frame, which is shown in Appendix C. Thus the TDX in the L frame is given by

$$\frac{d^3\sigma}{dE_1^\mathrm{L} d\Omega_1^\mathrm{L} d\Omega_2^\mathrm{L}} = J_{\mathrm{G}\to\mathrm{L}} F_\mathrm{kin}\frac{(2\pi)^4}{\hbar v_i}\sum_{lj}\sum_{\mu_1\mu_2\mu_0\mu_j}\frac{1}{2(2j+1)}\left|T_{\mu_1\mu_2\mu_0\mu_j}\right|^2. \tag{2.52}$$

Since the momentum of the residual nucleus B is directly related to the single-particle or cluster motion inside the target nucleus, the momentum distribution of B is a good alternative quantity for such studies. The momentum distribution of B in the A-rest frame is defined by

$$\frac{d\sigma}{d\boldsymbol{K}_\mathrm{B}^\mathrm{A}} = \int d\boldsymbol{K}_1^\mathrm{A} d\boldsymbol{K}_2^\mathrm{A}\delta(E_f^\mathrm{A} - E_i^\mathrm{A})\delta(\boldsymbol{K}_f^\mathrm{A} - \boldsymbol{K}_i^\mathrm{A})\frac{d^3\sigma}{dE_1 d\Omega_1^\mathrm{A} d\Omega_2^\mathrm{A}}, \tag{2.53}$$

where quantities with superscript A are evaluated in the A-rest frame, and the TDX in that frame is obtained by

$$\frac{d^3\sigma}{dE_1^\mathrm{A} d\Omega_1^\mathrm{A} d\Omega_2^\mathrm{A}} = J_{\mathrm{G}\to\mathrm{A}}\frac{d^3\sigma}{dE_1 d\Omega_1 d\Omega_2}, \tag{2.54}$$

with $J_{\mathrm{G}\to\mathrm{A}}$ being the Jacobian from the G to the A-rest frame. From this expression of the momentum distribution, the so-called longitudinal momentum distribution (LMD), sometimes called the parallel momentum distribution (PMD), is obtained by

$$\frac{d\sigma}{dK^{\mathrm{A}}_{\mathrm{B}z}} = 2\pi \int dK^{\mathrm{A}}_{\mathrm{B}b} K^{\mathrm{A}}_{\mathrm{B}b} \frac{d\sigma}{d\boldsymbol{K}^{\mathrm{A}}_{\mathrm{B}}}. \tag{2.55}$$

Note that $\boldsymbol{K}^{\mathrm{A}}_{\mathrm{B}}$ is now described in the cylindrical coordinate, i.e.,

$$\boldsymbol{K}^{\mathrm{A}}_{\mathrm{B}} = (K^{\mathrm{A}}_{\mathrm{B}b}, K^{\mathrm{A}}_{\mathrm{B}\phi}, K^{\mathrm{A}}_{\mathrm{B}z}), \tag{2.56}$$

$$d\boldsymbol{K}^{\mathrm{A}}_{\mathrm{B}} = K^{\mathrm{A}}_{\mathrm{B}b}\, dK^{\mathrm{A}}_{\mathrm{B}b}\, dK^{\mathrm{A}}_{\mathrm{B}\phi}\, dK_{\mathrm{B}z}. \tag{2.57}$$

Similarly, the transverse momentum distribution (TMD) is utilized:

$$\frac{d\sigma}{K^{\mathrm{A}}_{\mathrm{B}b} dK^{\mathrm{A}}_{\mathrm{B}b}} = 2\pi \int dK^{\mathrm{A}}_{\mathrm{B}z} \frac{d\sigma}{d\boldsymbol{K}^{\mathrm{A}}_{\mathrm{B}}}. \tag{2.58}$$

Describing $\boldsymbol{K}^{\mathrm{A}}_{\mathrm{B}}$ in the Cartesian coordinate, i.e.,

$$\boldsymbol{K}^{\mathrm{A}}_{\mathrm{B}} = (K^{\mathrm{A}}_{\mathrm{B}x}, K^{\mathrm{A}}_{\mathrm{B}y}, K^{\mathrm{A}}_{\mathrm{B}z}), \tag{2.59}$$

$$d\boldsymbol{K}^{\mathrm{A}}_{\mathrm{B}} = dK^{\mathrm{A}}_{\mathrm{B}x}\, dK^{\mathrm{A}}_{\mathrm{B}y}\, dK^{\mathrm{A}}_{\mathrm{B}z}, \tag{2.60}$$

another definition of the TMD is sometimes given by

$$\frac{d\sigma}{dK^{\mathrm{A}}_{\mathrm{B}x}} = \int dK^{\mathrm{A}}_{\mathrm{B}y}\, dK^{\mathrm{A}}_{\mathrm{B}z} \frac{d\sigma}{d\boldsymbol{K}^{\mathrm{A}}_{\mathrm{B}}}. \tag{2.61}$$

2.1.3 Local semi-classical approximation and asymptotic momentum approximation to DWIA T-matrix

The propagation of a distorted wave $\chi_{\boldsymbol{K}}$ from $\boldsymbol{R}$ to $\boldsymbol{R}+\boldsymbol{s}$ can be described by

$$\chi_{\boldsymbol{K}}(\boldsymbol{R}+\boldsymbol{s}) = \chi_{\boldsymbol{K}}(\boldsymbol{R}) e^{i\boldsymbol{K}(\boldsymbol{R})\cdot\boldsymbol{s}}. \tag{2.62}$$

For a given $\boldsymbol{s}$, one may always find a *complex* function $\boldsymbol{K}(\boldsymbol{R})$ which satisfies the equation above, but instead, there are several choices for approximating $\boldsymbol{K}(\boldsymbol{R})$ appropriate for only small distance s. An ideal way in the DWIA framework will be the so-called local semi-classical approximation (LSCA) [66, 67]. When the distorted wave $\chi_{\boldsymbol{K}}(\boldsymbol{R})$ is a solution of the Schrödinger equation with an optical potential $U(\boldsymbol{R})$:

$$\left[-\frac{\hbar^2}{2\mu}\nabla^2 + U(\boldsymbol{R})\right] \chi_{\boldsymbol{K}}(\boldsymbol{R}) = E\chi_{\boldsymbol{K}}(\boldsymbol{R}), \tag{2.63}$$

the LSCA assumes that the norm of the local momentum $\boldsymbol{K}(\boldsymbol{R})$ is the real part of a complex momentum $\boldsymbol{k}_c(\boldsymbol{R})$. The magnitude of $\boldsymbol{k}_c(\boldsymbol{R})$ is determined by the local energy conservation

$$\left[\frac{\hbar k_c^2(\boldsymbol{R})}{2\mu} + U(\boldsymbol{R})\right] = E \tag{2.64}$$

and its direction to be parallel with the flux direction of $\chi_{\boldsymbol{K}}(\boldsymbol{R})$, i.e.,

$$\hat{\boldsymbol{K}}(\boldsymbol{R}) \parallel \mathrm{Re}\left[\chi^*_{\boldsymbol{K}}(\boldsymbol{R})\nabla\chi_{\boldsymbol{K}}(\boldsymbol{R})\right] \parallel \hat{\boldsymbol{j}}(\boldsymbol{R}). \tag{2.65}$$

The LSCA is shown to be valid for about $s < 2.0$ fm for proton scattering above 50 MeV in Refs. [68, 69].

The coordinates $\boldsymbol{R}_0$, $\boldsymbol{R}_1$ and $\boldsymbol{R}_2$ can be rewritten in terms of $\boldsymbol{R}$ and $\boldsymbol{s}$ as

$$\begin{aligned}\boldsymbol{R}_0 &= \boldsymbol{R}_1 - \frac{m_2}{m_\mathrm{A}}\boldsymbol{R}_2 \\ &= \left(1 - \frac{m_2}{m_\mathrm{A}}\right)\boldsymbol{R} + \frac{m_2}{m_1+m_2}\left(1 + \frac{m_1}{m_\mathrm{A}}\right)\boldsymbol{s} \\ &\equiv (1-\alpha_R)\boldsymbol{R} + \alpha_{0s}\boldsymbol{s}, \qquad (2.66)\\ \boldsymbol{R}_1 &= \boldsymbol{R} + \frac{m_2}{m_1+m_2}\boldsymbol{s} \equiv \boldsymbol{R} + \alpha_{1s}\boldsymbol{s}, \qquad (2.67)\\ \boldsymbol{R}_2 &= \boldsymbol{R} - \frac{m_1}{m_1+m_2}\boldsymbol{s} \equiv \boldsymbol{R} - \alpha_{2s}\boldsymbol{s}, \qquad (2.68)\end{aligned}$$

where m_i is the mass of particle i. Applying the LSCA to the distorted waves then results in

$$\chi^{(+)\mu_0'\mu_0}_{0,\boldsymbol{K}_0}(\boldsymbol{R}_0) \approx \chi^{(+)\mu_0'\mu_0}_{0,\boldsymbol{K}_0}(\boldsymbol{R}) e^{-i\alpha_R \boldsymbol{K}_0(\boldsymbol{R})\cdot\boldsymbol{R}} e^{i\alpha_{0s}\boldsymbol{K}_0(\boldsymbol{R})\cdot\boldsymbol{s}}, \qquad (2.69)$$

$$\chi^{(-)\mu_1'\mu_1}_{1,\boldsymbol{K}_1}(\boldsymbol{R}_1) \approx \chi^{(-)\mu_1'\mu_1}_{1,\boldsymbol{K}_1}(\boldsymbol{R}) e^{i\alpha_{1s}\boldsymbol{K}_1(\boldsymbol{R})\cdot\boldsymbol{s}}, \qquad (2.70)$$

$$\chi^{(-)\mu_2'\mu_2}_{2,\boldsymbol{K}_2}(\boldsymbol{R}_2) \approx \chi^{(-)\mu_2'\mu_2}_{2,\boldsymbol{K}_2}(\boldsymbol{R}) e^{-i\alpha_{2s}\boldsymbol{K}_2(\boldsymbol{R})\cdot\boldsymbol{s}}. \qquad (2.71)$$

On the other hand, the Fourier transformation to the bound state wave function reads

$$\begin{aligned}\varphi_{nljm}(\boldsymbol{R}_2) &\equiv \varphi_{nlj}(R_2) Y_{lm}(\hat{\boldsymbol{R}}_2) \\ &= \frac{1}{(2\pi)^{3/2}} \int d\boldsymbol{K}_\mathrm{b} \tilde{\varphi}_{nljm}(\boldsymbol{K}_\mathrm{b}) e^{i\boldsymbol{K}_\mathrm{b}\cdot\boldsymbol{R}_2} \\ &= \frac{1}{(2\pi)^{3/2}} \int d\boldsymbol{K}_\mathrm{b} \tilde{\varphi}_{nljm}(\boldsymbol{K}_\mathrm{b}) e^{i\boldsymbol{K}_\mathrm{b}\cdot\boldsymbol{R}} e^{-\alpha_{2s} i\boldsymbol{K}_\mathrm{b}\cdot\boldsymbol{s}}. \qquad (2.72)\end{aligned}$$

Inserting Eqs. (2.69)–(2.72) into Eq. (2.42) one obtains

$$\begin{aligned}T_{\mu_1\mu_2\mu_0\mu_j} = S^{1/2}_{nlj\nu_\mathrm{b}} \frac{1}{(2\pi)^{3/2}} \sum_{\mu_1'\mu_2'\mu_0'} \int d\boldsymbol{K}_\mathrm{b} \int d\boldsymbol{R}\, \chi^{*(-)\mu_1'\mu_1}_{1,\boldsymbol{K}_1}(\boldsymbol{R}) \chi^{*(-)\mu_2'\mu_2}_{2,\boldsymbol{K}_2}(\boldsymbol{R}) \\ \times \tilde{t}^{\mu_1'\mu_2'\nu_1\nu_2,\mu_0'\mu_\mathrm{b}\nu_0\nu_\mathrm{b}}_{12}(\boldsymbol{\kappa}', \boldsymbol{\kappa}; \boldsymbol{R})\, \chi^{(+)\mu_0'\mu_0}_{0,\boldsymbol{K}_0}(\boldsymbol{R})\, e^{-i\alpha_R \boldsymbol{K}_0\cdot\boldsymbol{R}} e^{i\boldsymbol{K}_\mathrm{b}\cdot\boldsymbol{R}} \\ \times \sum_m (lmI_\mathrm{b}\mu_\mathrm{b}|j\mu_j)\, \tilde{\varphi}_{nlj\mu_j}(\boldsymbol{K}_\mathrm{b}), \qquad (2.73)\end{aligned}$$

where

$$\begin{aligned}&\tilde{t}^{\mu_1'\mu_2'\nu_1\nu_2,\mu_0'\mu_\mathrm{b}\nu_0\nu_\mathrm{b}}_{12}(\boldsymbol{\kappa}', \boldsymbol{\kappa}; \boldsymbol{R}) \\ &\quad = \left\langle e^{i\boldsymbol{\kappa}'(\boldsymbol{R})\cdot\boldsymbol{s}} \eta^{(1)}_{1/2,\mu_1'} \xi^{(1)}_{1/2,\nu_1} \Phi^{t_2\nu_2}_{I_2\mu_2}(\varepsilon_2, \xi_2) \,\middle|\, t_{12} \,\middle|\, e^{i\boldsymbol{\kappa}(\boldsymbol{R})\cdot\boldsymbol{s}} \eta^{(0)}_{1/2,\mu_0'} \xi^{(0)}_{1/2,\nu_0} \Phi^{t_\mathrm{b}\nu_\mathrm{b}}_{I_\mathrm{b}\mu_\mathrm{b}}(\varepsilon_\mathrm{b}, \xi_\mathrm{b}) \right\rangle \qquad (2.74)\end{aligned}$$

and the local relative momentum of particles 0 and b (particles 1 and 2) in the initial (final) state, $\boldsymbol{\kappa}$ ($\boldsymbol{\kappa}'$), is given by

$$\boldsymbol{\kappa}(\boldsymbol{R}) = \alpha_{0s}\boldsymbol{K}_0(\boldsymbol{R}) - \alpha_{2s}\boldsymbol{K}_\mathrm{b}(\boldsymbol{R}), \qquad (2.75)$$

$$\boldsymbol{\kappa}'(\boldsymbol{R}) = \alpha_{1s}\boldsymbol{K}_1(\boldsymbol{R}) - \alpha_{2s}\boldsymbol{K}_2(\boldsymbol{R}). \qquad (2.76)$$

By assuming the momentum conservation of the two colliding particles:

$$\frac{m_{\rm A}+m_1}{m_{\rm A}}\boldsymbol{K}_0(\boldsymbol{R})+\boldsymbol{K}_{\rm b}(\boldsymbol{R})\approx\boldsymbol{K}_1(\boldsymbol{R})+\boldsymbol{K}_2(\boldsymbol{R}), \tag{2.77}$$

$\boldsymbol{K}_{\rm b}(\boldsymbol{R})$ and $\boldsymbol{\kappa}(\boldsymbol{R})$ are determined by the asymptotic momenta of the scattering particles, $\boldsymbol{K}_0$, $\boldsymbol{K}_1$ and $\boldsymbol{K}_2$, and hence no term except $\varphi_{nlj\mu_j}(\boldsymbol{K}_{\rm b})$ depends on $\boldsymbol{K}_{\rm b}$. Through the inverse Fourier transform,

$$\begin{aligned}T_{\mu_1\mu_2\mu_0\mu_j}=S^{1/2}_{nlj\nu_{\rm b}}\sum_{\mu_1'\mu_2'\mu_0'}\int d\boldsymbol{R}\,\chi^{*(-)\mu_1'\mu_1}_{1,\boldsymbol{K}_1}(\boldsymbol{R})\chi^{*(-)\mu_2'\mu_2}_{2,\boldsymbol{K}_2}(\boldsymbol{R})\\ \times\tilde{t}^{\mu_1'\mu_2'\nu_1\nu_2,\mu_0'\mu_{\rm b}\nu_0\nu_{\rm b}}_{12}(\boldsymbol{\kappa}',\boldsymbol{\kappa};\boldsymbol{R})\,\chi^{(+)\mu_0'\mu_0}_{0,\boldsymbol{K}_0}(\boldsymbol{R})\,e^{-i\alpha_R\boldsymbol{K}_0\cdot\boldsymbol{R}}\\ \times\sum_m(lmI_{\rm b}\mu_{\rm b}|j\mu_j)\,\varphi_{nlj\mu_j}(\boldsymbol{R})\end{aligned} \tag{2.78}$$

is obtained.

As an alternative to the LSCA, further simplification, which is termed the asymptotic momentum approximation (AMA) in Ref [35], has been widely applied to the DWIA analyses. In the AMA, the local momentum $\boldsymbol{K}_i(\boldsymbol{R})$ $(i=0,1,2)$ is replaced by its asymptotic momentum $\boldsymbol{K}_i$. Therefore $\tilde{t}_{12}(\boldsymbol{R})$ no longer depends on $\boldsymbol{R}$ and can be factorized out of the $\boldsymbol{R}$ integration as

$$\begin{aligned}T_{\mu_1\mu_2\mu_0\mu_j}\approx S^{1/2}_{nlj\nu_{\rm b}}\sum_{\mu_1'\mu_2'\mu_0'}\tilde{t}^{\mu_1'\mu_2'\nu_1\nu_2,\mu_0'\mu_{\rm b}\nu_0\nu_{\rm b}}_{12}(\boldsymbol{\kappa}',\boldsymbol{\kappa})\\ \times\int d\boldsymbol{R}\,\chi^{*(-)\mu_1'\mu_1}_{1,\boldsymbol{K}_1}(\boldsymbol{R})\chi^{*(-)\mu_2'\mu_2}_{2,\boldsymbol{K}_2}(\boldsymbol{R})\chi^{(+)\mu_0'\mu_0}_{0,\boldsymbol{K}_0}(\boldsymbol{R})\,e^{-i\alpha_R\boldsymbol{K}_0\cdot\boldsymbol{R}}\\ \times\sum_m(lmI_{\rm b}\mu_{\rm b}|j\mu_j)\,\varphi_{nlj\mu_j}(\boldsymbol{R}).\end{aligned} \tag{2.79}$$

In most cases the effective interaction t_{12} and its matrix element $\tilde{t}_{12}$ are defined in the center-of-mass frame of particles 1 and 2 (the t frame). The transformation from the t frame to the G frame can be carried out by multiplying $\tilde{t}_{12}$ by the so-called Møller factor

$$f_{\rm Møl}=\left(\frac{E_1^{\rm t}E_2^{\rm t}E_0^{\rm t}E_{\rm b}^{\rm t}}{E_1E_2E_0E_{\rm b}}\right)^{1/2}. \tag{2.80}$$

2.1.4 On-shell approximation and DWIA T-matrix without spin-orbit force

When the spin-orbit interaction of distorting potentials is absent and the off-the-energy-shell (on-shell) approximation is adopted to $\tilde{t}_{12}$, the elastic cross section of particles 1 and 2 can be used instead of $\tilde{t}_{12}$. Since the collision between particles 0 and b (particles 1 and 2) occurs in the target nucleus, nucleon-nucleon matrix element is in general in an off-the-energy-shell (off-shell) that is difficult to handle. One of the most common methods to make an on-shell approximation is, keeping the direction of $\boldsymbol{\kappa}$, to replace the norm κ with that of κ', i.e.,

$$\boldsymbol{\kappa}\approx\kappa'\hat{\boldsymbol{\kappa}}. \tag{2.81}$$

This is termed the final energy prescription. The opposite way

$$\boldsymbol{\kappa}' \approx \kappa \hat{\boldsymbol{\kappa}}' \tag{2.82}$$

is also possible, which is called the initial energy prescription. The former is commonly adopted and known to make the resulting observables agree well with experimental data, because the momenta of particles 1 and 2 in emission are directly measured by experiments, while in the latter an assumption or interpretation like Eq. (2.77) is needed to fix $\boldsymbol{K}_{\rm b}$ and $\boldsymbol{\kappa}$. There exists another on-shell approximation, which is called average prescription: it rescales the norms of $\boldsymbol{\kappa}$ and $\boldsymbol{\kappa}'$ by

$$\boldsymbol{\kappa} \approx \sqrt{\frac{\kappa^2+\kappa'^2}{2}}\hat{\boldsymbol{\kappa}}, \tag{2.83}$$

$$\boldsymbol{\kappa}' \approx \sqrt{\frac{\kappa^2+\kappa'^2}{2}}\hat{\boldsymbol{\kappa}}', \tag{2.84}$$

so that they give an averaged relative energy

$$E_{\rm ave} = \frac{\hbar^2(\kappa^2+\kappa'^2)/2}{2\mu_{12}}. \tag{2.85}$$

In the situation that there are no spin-orbit term in distorting potentials, the distorted waves have no spin-flipped component and the T-matrix of Eq. (2.78) is reduced to

$$\begin{aligned} T_{\mu_1\mu_2\mu_0\mu_j} = S^{1/2}_{nlj\nu_{\rm b}} \int d\boldsymbol{R}\, &\chi^{*(-)\mu_1\mu_1}_{1,\boldsymbol{K}_1}(\boldsymbol{R})\chi^{*(-)\mu_2\mu_2}_{2,\boldsymbol{K}_2}(\boldsymbol{R}) \\ &\times \tilde{t}^{\mu_1\mu_2\nu_1\nu_2,\mu_0\mu_{\rm b}\nu_0\nu_{\rm b}}_{12}(\boldsymbol{\kappa}',\boldsymbol{\kappa};\boldsymbol{R})\, \chi^{(+)\mu_0\mu_0}_{0,\boldsymbol{K}_0}(\boldsymbol{R})\, e^{-i\alpha_R \boldsymbol{K}_0\cdot\boldsymbol{R}} \\ &\times \sum_m (lmI_{\rm b}\mu_{\rm b}|j\mu_j)\, \varphi_{nlj\mu_j}(\boldsymbol{R}). \end{aligned} \tag{2.86}$$

When taking the norm square of Eq. (2.86), an averaging prescription for $\mu_{\rm b}$ is made:

$$\begin{aligned} &\tilde{t}^{*\mu_1\mu_2\nu_1\nu_2,\mu_0\mu'_{\rm b}\nu_0\nu_{\rm b}}_{12}(\boldsymbol{\kappa}',\boldsymbol{\kappa};\boldsymbol{R})\, \tilde{t}^{\mu_1\mu_2\nu_1\nu_2,\mu_0\mu_{\rm b}\nu_0\nu_{\rm b}}_{12}(\boldsymbol{\kappa}',\boldsymbol{\kappa};\boldsymbol{R}) \\ &\quad\approx \frac{1}{2I_{\rm b}+1}\sum_{\bar{\mu}_{\rm b}} \left|\tilde{t}^{\mu_1\mu_2\nu_1\nu_2,\mu_0\bar{\mu}_{\rm b}\nu_0\nu_{\rm b}}_{12}(\boldsymbol{\kappa}',\boldsymbol{\kappa};\boldsymbol{R})\right|^2 \delta_{\mu'_{\rm b}\mu_{\rm b}}, \end{aligned} \tag{2.87}$$

Once the on-shell approximation, for example Eq. (2.81), is adopted, the scattering angle $\theta_{12}(\boldsymbol{R})$ and the energy $E_{12}(\boldsymbol{R})$ of the elementary process can be fixed by

$$E_{12}(\boldsymbol{R}) = \frac{\hbar^2\kappa'^2(\boldsymbol{R})}{2\mu_{12}}, \tag{2.88}$$

$$\cos\theta_{12}(\boldsymbol{R}) = \frac{\boldsymbol{\kappa}'(\boldsymbol{R})\cdot\boldsymbol{\kappa}(\boldsymbol{R})}{\kappa'(\boldsymbol{R})\kappa(\boldsymbol{R})}. \tag{2.89}$$

Since $\tilde{t}^{\mu_1\mu_2\nu_1\nu_2,\mu_0\bar{\mu}_{\rm b}\nu_0\nu_{\rm b}}_{12}(\boldsymbol{\kappa}',\boldsymbol{\kappa};\boldsymbol{R})$ is related to the elastic cross section of particles 1 and 2 as

$$\frac{d\sigma_{12}}{d\Omega_{12}}(\theta_{12}(\boldsymbol{R}),E_{12}(\boldsymbol{R})) = \frac{\mu_{12}^2}{(2\pi\hbar^2)^2}\frac{1}{2}\frac{1}{2I_{\rm b}+1}\sum_{\mu_1\mu_2\mu_0\bar{\mu}_{\rm b}} \left|\tilde{t}^{\mu_1\mu_2\nu_1\nu_2,\mu_0\bar{\mu}_{\rm b}\nu_0\nu_{\rm b}}_{12}(\boldsymbol{\kappa}',\boldsymbol{\kappa};\boldsymbol{R})\right|, \tag{2.90}$$

Eq. (2.52) is reduced to

$$\frac{d^3\sigma}{dE_1^{\rm L}d\Omega_1^{\rm L}d\Omega_2^{\rm L}} = J_{\rm G\to L}F_{\rm kin}\frac{(2\pi)^4}{\hbar v_i}\frac{(2\pi\hbar^2)^2}{\mu_{12}}\sum_{lj}\frac{1}{2l+1}S_{nlj\nu_{\rm b}} \times \sum_m \left| \int d\boldsymbol{R}\chi^{*(-)\mu_1\mu_1}_{1,\boldsymbol{K}_1}(\boldsymbol{R})\chi^{*(-)\mu_2\mu_2}_{2,\boldsymbol{K}_2}(\boldsymbol{R})\chi^{(+)\mu_0\mu_0}_{0,\boldsymbol{K}_0}(\boldsymbol{R})e^{-i\alpha_R\boldsymbol{K}_0\cdot\boldsymbol{R}} \times \varphi_{nlj\mu_j}(\boldsymbol{R})\sqrt{\frac{d\sigma_{12}}{d\Omega_{12}}(\theta_{12}(\boldsymbol{R}),E_{12}(\boldsymbol{R}))}\right|^2, \tag{2.91}$$

where use has been made of

$$\sum_{\mu_j\mu_{\rm b}}\left(lm'I_{\rm b}\mu_{\rm b}|j\mu_j\right)\left(lmI_{\rm b}\mu_{\rm b}|j\mu_j\right) = \frac{2j+1}{2l+1}\delta_{m'm}. \tag{2.92}$$

If the AMA is adopted instead of the LSCA, Eq. (2.91) is factorized as

$$\frac{d^3\sigma}{dE_1^{\rm L}d\Omega_1^{\rm L}d\Omega_2^{\rm L}} = J_{\rm G\to L}F_{\rm kin}\frac{(2\pi)^4}{\hbar v_i}\frac{(2\pi\hbar^2)^2}{\mu_{12}}\sum_{lj}\frac{1}{2l+1}S_{nlj\nu_{\rm b}}\frac{d\sigma_{12}}{d\Omega_{12}}(\theta_{12},E_{12}) \times \sum_m \left| \int d\boldsymbol{R}\chi^{*(-)\mu_1\mu_1}_{1,\boldsymbol{K}_1}(\boldsymbol{R})\chi^{*(-)\mu_2\mu_2}_{2,\boldsymbol{K}_2}(\boldsymbol{R})\chi^{(+)\mu_0\mu_0}_{0,\boldsymbol{K}_0}(\boldsymbol{R})e^{-i\alpha_R\boldsymbol{K}_0\cdot\boldsymbol{R}} \times \varphi_{nlj\mu_j}(\boldsymbol{R})\right|^2, \tag{2.93}$$

where θ_{12} and E_{12} are fixed in the same way as in Eqs. (2.88) and (2.89) but with the asymptotic momenta.

Equation (2.93) is the most simplified and probably the most widely used form of the DWIA T-matrix when spin degrees of freedom are neglected. It should be noted that when polarized quantities are discussed, both the spin-orbit interaction of the distorting potentials and the spin dependence of $\tilde{t}_{12}^{\mu_1\mu_2\nu_1\nu_2,\mu_0\mu_{\rm b}\nu_0\nu_{\rm b}}$ are essential.

2.1.5 Plane wave impulse approximation

It is worth looking at the plane wave limit of the DWIA framework, which is termed the plane wave impulse approximation (PWIA), to show clearly the basic concept of the knockout reaction. From Eq. (2.93), when all distorted waves are replaced with plane waves, the TDX is given by

$$\frac{d^3\sigma}{dE_1^{\rm L}d\Omega_1^{\rm L}d\Omega_2^{\rm L}} = J_{\rm G\to L}F_{\rm kin}\frac{1}{\hbar v_i}\frac{\hbar^4}{(2\pi)^3\mu_{12}}\sum_{lj}\frac{1}{2l+1}S_{nlj\nu_{\rm b}}\frac{d\sigma_{12}}{d\Omega_{12}}(\theta_{12},E_{12}) \times \sum_m \left|\tilde{\varphi}_{nlj\mu_j}(\boldsymbol{q})\right|^2, \tag{2.94}$$

where $\tilde{\varphi}_{nlj\mu_j}(\boldsymbol{q})$ is the Fourier transform of $\varphi_{nlj\mu_j}(\boldsymbol{R})$:

$$\tilde{\varphi}_{nlj\mu_j}(\boldsymbol{q}) = \int d\boldsymbol{R}e^{i\boldsymbol{q}\cdot\boldsymbol{R}}\varphi_{nlj\mu_j}(\boldsymbol{R}) \tag{2.95}$$

and $\boldsymbol{q}$ is the so-called missing momentum

$$\boldsymbol{q} = (1-\alpha_R)\,\boldsymbol{K}_0 - \boldsymbol{K}_1 - \boldsymbol{K}_2, \tag{2.96}$$

which is known to correspond to the momentum of the residual nucleus B in the L frame, $\boldsymbol{K}_{\rm B}^{\rm L}$. Moreover, since the knockout reaction is performed with relatively high incident energies, say, several hundreds of MeV, the sudden reaction picture works well leaving B as a spectator. Thus, $-\boldsymbol{q}$ can be regarded as the momentum of b when it is knocked out. This is why the knockout reaction is considered to be an appropriate method to investigate or probe single-particle and cluster states of nuclei.

2.2 Helicity representation

2.2.1 Distorted wave in helicity representation

In the practical calculation of the DWIA T-matrix, when spin-orbit terms are included in particular, it is much easier and faster to evaluate the integration over $\boldsymbol{R}$ in three-dimensional space, instead of performing angular momentum algebra of three scattering particles to reduce the $\boldsymbol{R}$ integration to one dimensional integration over R, as discussed in Ref. [40]. Although angular momentum algebra is avoided when the three-dimensional integration way is taken, still one needs to handle spin degrees of freedom in the DWIA framework. One of the promising ways to extract the essence of spin degrees of freedom in the scattering theory is the helicity formalism [40, 63, 70, 71]. The definition of helicity h is given by

$$h = \boldsymbol{J} \cdot \hat{\boldsymbol{p}}, \tag{2.97}$$

where $\boldsymbol{J}$ is the total angular momentum of a moving particle, a vector sum of the orbital angular momentum $\boldsymbol{L}$ and the spin $\boldsymbol{s}$: $\boldsymbol{J} = \boldsymbol{L} + \boldsymbol{s}$. Since $\boldsymbol{L} = \boldsymbol{r} \times \boldsymbol{p}$, the helicity can be rewritten as

$$h = \boldsymbol{s} \cdot \hat{\boldsymbol{p}}, \tag{2.98}$$

$$-s \leq h \leq s. \tag{2.99}$$

The helicity can be understood as the spin projection onto the direction of motion. This way of quantizing angular momenta allows us to see spin degrees of freedom clearly.

The Schrödinger equation of a scattering particle with an optical potential $U(R)$ is given by

$$\left[-\frac{\hbar^2}{2\mu}\nabla_{\boldsymbol{R}}^2 + U(R)\right]\chi_{\boldsymbol{K}}(\boldsymbol{R}) = \frac{\hbar^2 K^2}{2\mu}\chi_{\boldsymbol{K}}(\boldsymbol{R}) = E\chi_{\boldsymbol{K}}(\boldsymbol{R}). \tag{2.100}$$

The angular dependence of the scattering wave function is expressed by spherical harmonics $Y_{LM}(\Omega)$ within a usual partial wave decomposition, and the radial Schrödinger equation is given by

$$\left[-\frac{\hbar^2}{2\mu}\frac{d^2}{dR^2} + \frac{\hbar^2}{2\mu}\frac{L(L+1)}{R^2} + U(R) - E\right]u_L(R) = 0. \tag{2.101}$$

If $U(R)$ consists of central and spin-orbit terms, $U(R) = U_C(R) + 2(\boldsymbol{L}\cdot\boldsymbol{s})U_{so}(R)$, Eq. (2.101) splits into two equations:

$$\left[-\frac{\hbar^2}{2\mu}\frac{d^2}{dR^2} + \frac{\hbar^2}{2\mu}\frac{L(L+1)}{R^2} + U_C(R) + LU_{so}(R) - E\right] u_{LJ_+}(R) = 0, \tag{2.102}$$

$$\left[-\frac{\hbar^2}{2\mu}\frac{d^2}{dR^2} + \frac{\hbar^2}{2\mu}\frac{L(L+1)}{R^2} + U_C(R) - (L+1)U_{so}(R) - E\right] u_{LJ_-}(R) = 0. \tag{2.103}$$

Here, I have assumed that $s = 1/2$

$$\langle JLS\,|\,2\boldsymbol{L}\cdot\boldsymbol{s}\,|\,JLS\rangle = J(J+1) - L(L+1) - s(s+1) \tag{2.104}$$

$$= \begin{cases} L & (\text{for } J = J_+ = L + 1/2), \\ -(L+1) & (\text{for } J = J_- = L - 1/2). \end{cases} \tag{2.105}$$

Before discussing the distorted wave in the helicity formalism, let us recapitulate the scattering wave in the JM representation, in which the angular momenta are quantized in the z-direction, i.e.,

$$\chi^{\mu'\mu}_{\boldsymbol{K}}(\boldsymbol{R}) = \frac{4\pi}{(2\pi)^{3/2}} \sum_{LMM'JM_J} (LM1/2\mu|JM_J)(LM'1/2\mu'|JM_J) i^L \frac{u_{LJ}(K,R)}{KR} \times Y^*_{LM}(\hat{\boldsymbol{K}}) Y_{LM'}(\hat{\boldsymbol{R}}) \eta_{1/2,\mu'}, \tag{2.106}$$

and also its form in a special case when $\hat{\boldsymbol{K}} = \hat{z}$:

$$\chi^{\mu'\mu}_{\boldsymbol{K}}(\boldsymbol{R}) = \frac{4\pi}{(2\pi)^{3/2}} \sum_{LJ} (L01/2\mu|JM_J)(LM'1/2\mu'|JM_J) i^L \frac{u_{LJ}(K,R)}{KR} \times \sqrt{\frac{2L+1}{4\pi}} Y_{LM'}(\hat{\boldsymbol{R}}) \eta_{1/2,\mu'}. \tag{2.107}$$

Note that in Eq. (2.107), M_J and M' are uniquely determined once μ and μ' are given. Since in Eq. (2.107) $\boldsymbol{K}$ is parallel with the quantization axis $\hat{z}$, this can be also interpreted as the helicity representation of the scattering wave. For general directions of $\boldsymbol{K}$, the distorted wave in the helicity representation is given by

$$\chi^{h'h}_{\boldsymbol{K}}(\boldsymbol{R}) = \frac{4\pi}{(2\pi)^{3/2}} \sum_{LJ} (L01/2h|Jh)(L,(h-h'),1/2h'|Jh) i^L \frac{u_{LJ}(K,R)}{KR} \times \sqrt{\frac{2L+1}{4\pi}} Y_{L,(h-h')}(\hat{\boldsymbol{R}}_h) \eta_{1/2,h'}, \tag{2.108}$$

where $\boldsymbol{R}_h$ is the coordinate in, what I call, the helicity frame. $\boldsymbol{K}$ is taken to be parallel with z_h, i.e.,

$$\boldsymbol{R} = \hat{R}(\boldsymbol{K})\boldsymbol{R}_h, \tag{2.109}$$

with $\hat{R}(\boldsymbol{K})$ being the rotation operator which transforms a given frame to the helicity frame.

A two dimensional schematic picture of the rotation is shown in Fig. 2.2. A given coordinate $\boldsymbol{R} = R(\cos\theta, \sin\theta)$ is described by $\boldsymbol{R}_h = R(\cos\theta_h, \sin\theta_h)$ in the helicity frame. Those two are connected with each other by the rotation operator from a given

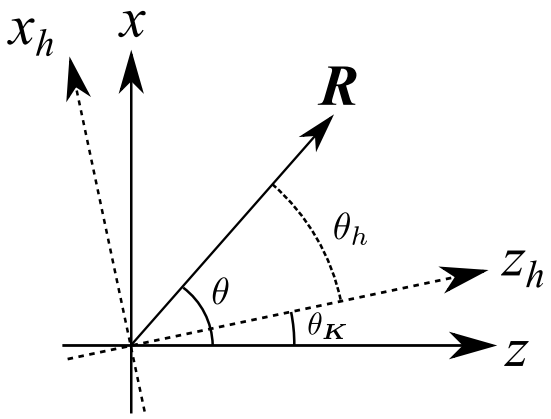

FIGURE 2.2: The relation between a given frame and the helicity frame in two dimensional space. z_h of the helicity frame is taken to be parallel with the momentum $\boldsymbol{K}$.

frame to the helicity frame,

$$\hat{R}(\boldsymbol{K}) = \begin{pmatrix} \cos\theta_{\boldsymbol{K}} & -\sin\theta_{\boldsymbol{K}} \\ \sin\theta_{\boldsymbol{K}} & \cos\theta_{\boldsymbol{K}} \end{pmatrix}, \tag{2.110}$$

which satisfies Eq. (2.109) since $\theta_{\boldsymbol{K}} + \theta_h = \theta$.

Using the following relation between the spherical harmonics and Wigner's D-matrix

$$Y_{LM}(\theta,\phi) = \sqrt{\frac{2L+1}{4\pi}} D^{*L}_{M0}(\phi,\theta,0), \tag{2.111}$$

Eq. (2.108) is reduced to

$$\chi^{h'h}_{\boldsymbol{K}}(\boldsymbol{R}) = \frac{1}{(2\pi)^{3/2}} \sum_{LJ} (2L+1)(L01/2h|Jh)(L(h-h')1/2h'|Jh) i^L \frac{u_{LJ}(K,R)}{KR} \times D^{*L}_{(h-h')0}(\hat{\boldsymbol{R}}_h)\eta_{1/2,h'}. \tag{2.112}$$

Some important mathematics of Wigner's D-matrix is given in Appendix B.

Writing down Eq. (2.112) explicitly for a $s = 1/2$ particle,

$$\chi^{1/2,1/2}_{\boldsymbol{K}}(\boldsymbol{R}) = \frac{1}{(2\pi)^{3/2}} \sum_L i^L \frac{(L+1)u_{LJ_+}(K,R) + Lu_{LJ_-}(K,R)}{KR} \times d^L_{00}(\theta_h)\eta_{1/2,1/2}, \tag{2.113}$$

$$\chi^{-1/2,-1/2}_{\boldsymbol{K}}(\boldsymbol{R}) = \frac{1}{(2\pi)^{3/2}} \sum_L i^L \frac{(L+1)u_{LJ_+}(K,R) + Lu_{LJ_-}(K,R)}{KR} \times d^L_{00}(\theta_h)\eta_{1/2,-1/2}, \tag{2.114}$$

$$\chi^{-1/2,1/2}_{\boldsymbol{K}}(\boldsymbol{R}) = \frac{1}{(2\pi)^{3/2}} \sum_L i^L \sqrt{L(L+1)} \frac{u_{LJ_+}(K,R) - U_{LJ_-}(K,R)}{KR} \times d^L_{10}(\theta_h)\, e^{i\phi_h}\eta_{1/2,-1/2} \tag{2.115}$$

$$\chi^{1/2,-1/2}_{\boldsymbol{K}}(\boldsymbol{R}) = \frac{-1}{(2\pi)^{3/2}} \sum_L i^L \sqrt{L(L+1)} \frac{u_{LJ_+}(K,R) - U_{LJ_-}(K,R)}{KR} \times d^L_{10}(\theta_h)\, e^{-i\phi_h}\eta_{1/2,1/2}. \tag{2.116}$$

Moreover, reorientating the quantization axis of h' to be parallel with $\hat{\boldsymbol{R}}_h$ by

$$\eta_{1/2,h'} = \sum_{h'_{\boldsymbol{R}_h}} D^{*1/2}_{h'h'_{\boldsymbol{R}_h}}(\hat{\boldsymbol{R}}_h)\, \eta_{1/2,h'_{\boldsymbol{R}_h}}, \tag{2.117}$$

Eq. (2.112) is transformed into

$$\chi^{h'h}_{\boldsymbol{K}}(\boldsymbol{R}) = \frac{1}{(2\pi)^{3/2}} \sum_{LJh'_{\boldsymbol{R}_h}} (2L+1)(L01/2h|Jh)(L(h-h')1/2h'|Jh) \times i^L \frac{u_{LJ}(K,R)}{KR} D^{*L}_{(h-h')0}(\hat{\boldsymbol{R}}_h) D^{*1/2}_{h'h'_{\boldsymbol{R}_h}}(\hat{\boldsymbol{R}}_h)\, \eta_{1/2,h'_{\boldsymbol{R}_h}}. \tag{2.118}$$

The coupling formula of Wigner's D-matrix

$$\sum_{N_1N_2} (J_1N_1J_2N_2|JN) D^{J_1}_{M_1N_1}(\Omega) D^{J_2}_{M_2N_2}(\Omega) = (J_1M_1J_2M_2|JM) D^J_{MN}(\Omega) \tag{2.119}$$

reduces the distorted wave summed over h' as

$$\begin{aligned}
\chi^h_{\boldsymbol{K}}(\boldsymbol{R}) =& \sum_{h'} \chi^{h'h}_{\boldsymbol{K}}(\boldsymbol{R}) \\
=& \frac{1}{(2\pi)^{3/2}} \sum_{LJh'_{\boldsymbol{R}_h}h'} (2L+1)(L01/2h|Jh)(L(h-h')1/2h'|Jh) \\
& \times i^L \frac{u_{LJ}(K,R)}{KR} D^{*L}_{(h-h')0}(\hat{\boldsymbol{R}}_h) D^{*1/2}_{h'h'_{\boldsymbol{R}_h}}(\hat{\boldsymbol{R}}_h)\, \eta_{1/2,h'_{\boldsymbol{R}_h}}, \\
=& \frac{1}{(2\pi)^{3/2}} \sum_{LJh'_{\boldsymbol{R}_h}} (2L+1)(L01/2h|Jh)(L01/2h'_{\boldsymbol{R}_h}|Jh'_{\boldsymbol{R}_h}) \\
& \times i^L \frac{u_{LJ}(K,R)}{KR} D^{*J}_{h'_{\boldsymbol{R}_h},h}(\hat{\boldsymbol{R}}_h)\, \eta_{1/2,h'_{\boldsymbol{R}_h}}.
\end{aligned} \tag{2.120}$$

Replacing the Clebsch-Gordan coefficient with explicit values (note $|h| = |h'_{\boldsymbol{R}_h}| = 1/2$), the final form of the distorted wave in the helicity representation is obtained as

$$\chi^{h}_{\boldsymbol{K}}(\boldsymbol{R}) = \sum_{h'_{\boldsymbol{R}_h}} \chi^{h'_{\boldsymbol{R}_h},h}_{\boldsymbol{K}}(\boldsymbol{R}),$$

$$\chi^{h'_{\boldsymbol{R}_h},h}_{\boldsymbol{K}}(\boldsymbol{R}) = \frac{1}{(2\pi)^{3/2}} \sum_{J} \frac{2J+1}{2} \frac{u^{J}_{h'_{\boldsymbol{R}_h},h}(K,R)}{KR} D^{*J}_{h'_{\boldsymbol{R}_h},h}(\boldsymbol{R}_h)\, \eta_{1/2,h'_{\boldsymbol{R}_h}}, \tag{2.121}$$

$$u^{J}_{h'_{\boldsymbol{R}_h},h}(K,R) = i^{J-1/2} \left(u_{L=J-1/2,J}(K,R) + i(-)^{h-h'_{\boldsymbol{R}_h}} u_{L=J+1/2,J}(K,R) \right). \tag{2.122}$$

In the present calculation of distorted waves, Eqs. (2.113)–(2.116) are employed for spin 1/2 particles. Reorientation of the quantization axis from the helicity to the conventional z projection is needed for evaluation of $\tilde{t}_{12}^{\mu'_1\mu'_2\nu_1\nu_2,\mu'_0\mu_{\rm b}\nu_0\nu_{\rm b}}$, since the effective interaction t_{12} is defined to be sandwiched by spin states quantized in the z-direction. Such reorientation can be accomplished by Wigner's D-matrix as in the same way as Eq. (2.117). Reorientation of h_0 to the y-direction is also needed in order to evaluate the vector analyzing power A_y. Thanks to the orthogonality and the completeness of Wigner's D-matrix, i.e.,

$$\sum_{k} D^{*l}_{mk}(\Omega) D^{l}_{m'k}(\Omega) = \delta_{mm'}, \tag{2.123}$$

$$\sum_{m} D^{*l}_{mk}(\Omega) D^{l}_{mk'}(\Omega) = \delta_{kk'}, \tag{2.124}$$

spin unpolarized observables are independent of the direction of the quantization axis. For example, reorientation of the quantization axis for particle 2 to an arbitrary direction

$$\left\langle \eta^{(2)}_{1/2,\mu_2} \right| = \sum_{\lambda_2} D^{*1/2}_{\lambda_2\mu_2}(\Omega_{\lambda\eta}) \left\langle 1/2, \lambda^{(2)}_2 \right| \tag{2.125}$$

does not change the result of the T-matrix as

$$\begin{aligned}
\sum_{\mu_1\mu_2\mu_0\mu_j} \left| T_{\mu_1\mu_2\mu_0\mu_j} \right|^2 &\to \sum_{\mu_1\mu_2\mu_0\mu_j} \left| \sum_{\lambda_2} D^{1/2}_{\lambda_2\mu_2}(\Omega_{\lambda\eta}) T_{\mu_1\lambda_2\mu_0\mu_j} \right|^2 \\
&= \sum_{\mu_1\mu_2\mu_0\mu_j} \left(\sum_{\lambda'_2} D^{*1/2}_{\lambda'_2\mu_2}(\Omega_{\lambda\eta}) T^{*}_{\mu_1\lambda'_2\mu_0\mu_j} \right) \left(\sum_{\lambda_2} D^{1/2}_{\lambda_2\mu_2}(\Omega_{\lambda\eta}) T_{\mu_1\lambda_2\mu_0\mu_j} \right) \\
&= \sum_{\mu_1\mu_0\mu_j} \sum_{\lambda'_2\lambda_2} \sum_{\mu_2} D^{*1/2}_{\lambda'_2\mu_2}(\Omega_{\lambda\eta}) D^{1/2}_{\lambda_2\mu_2}(\Omega_{\lambda\eta}) T^{*}_{\mu_1\lambda'_2\mu_0\mu_j} T_{\mu_1\lambda_2\mu_0\mu_j} \\
&= \sum_{\mu_1\lambda_2\mu_0\mu_j} \left| T_{\mu_1\lambda_2\mu_0\mu_j} \right|^2 .
\end{aligned} \tag{2.126}$$

2.2.2 DWIA in helicity representation and vector analyzing power

Since the distorted waves can easily be evaluated in the helicity representation, the following helicity representation is adopted for the present calculation of the DWIA T-matrix. The T-matrix in the helicity representation which corresponds to Eq. (2.78)

is given by

$$T_{h_1h_2h_0\mu_j} = S^{1/2}_{nlj\nu_{\rm b}} \sum_{h_1'h_2'h_0'} \int d\boldsymbol{R}\, \chi^{*(-)h_1'h_1}_{1,\boldsymbol{K}_1}(\boldsymbol{R}) \chi^{*(-)h_2'h_2}_{2,\boldsymbol{K}_2}(\boldsymbol{R}) \times \tilde{t}^{h_1'h_2'\nu_1\nu_2,h_0'\mu_{\rm b}\nu_0\nu_{\rm b}}_{12}(\boldsymbol{\kappa}',\boldsymbol{\kappa};\boldsymbol{R})\, \chi^{(+)h_0'h_0}_{0,\boldsymbol{K}_0}(\boldsymbol{R})\, e^{-i\alpha_R \boldsymbol{K}_0\cdot\boldsymbol{R}} \times \sum_m (lmI_{\rm b}\mu_{\rm b}|j\mu_j)\, \varphi_{nlj\mu_j}(\boldsymbol{R}), \tag{2.127}$$

where

$$\tilde{t}^{h_1'h_2'\nu_1\nu_2,h_0'\mu_{\rm b}\nu_0\nu_{\rm b}}_{12}(\boldsymbol{\kappa}',\boldsymbol{\kappa};\boldsymbol{R}) \tag{2.128}$$

$$= \left\langle e^{i\boldsymbol{\kappa}'(\boldsymbol{R})\cdot\boldsymbol{s}} \eta^{(1)}_{1/2,h_1'} \xi^{(1)}_{1/2,\nu_1} \Phi^{t_2\nu_2}_{I_2h_2}(\varepsilon_2,\xi_2) \,\middle|\, t_{12} \,\middle|\, e^{i\boldsymbol{\kappa}(\boldsymbol{R})\cdot\boldsymbol{s}} \eta^{(0)}_{1/2,h_0'} \xi^{(0)}_{1/2,\nu_0} \Phi^{t_{\rm b}\nu_{\rm b}}_{I_{\rm b}h_{\rm b}}(\varepsilon_{\rm b},\xi_{\rm b}) \right\rangle. \tag{2.129}$$

The following procedure is taken to rotate the quantization axis of h_1' and h_2':

$$\tilde{t}^{h_1'h_2'\nu_1\nu_2,h_0'\mu_{\rm b}\nu_0\nu_{\rm b}}_{12}(\boldsymbol{\kappa}',\boldsymbol{\kappa};\boldsymbol{R}) \tag{2.130}$$

$$= \sum_{\mu_0'\mu_1'\mu_2'} D^{*1/2}_{\mu_1'h_1'}(\Omega_{h_1z}) D^{*1/2}_{\mu_2'h_2'}(\Omega_{h_2z}) \tilde{t}^{\mu_1'\mu_2'\nu_1\nu_2,\mu_0'\mu_{\rm b}\nu_0\nu_{\rm b}}_{12}(\boldsymbol{\kappa}',\boldsymbol{\kappa};\boldsymbol{R}). \tag{2.131}$$

Note that the JM and the helicity representation are equivalent for particle 0 when the Madison convention is adopted.

On the other hand, the asymptotic spin of particle 0, μ_0 $(= h_0)$, should be quantized in the y direction, which is denoted by $\mu_0^{(y)}$, in order to evaluate the vector analyzing power A_y defined by

$$A_y \equiv \frac{\displaystyle\sum_{h_1h_2\mu_j} \left[\left| T_{h_1h_2,\mu_0^{(y)}=1/2,\mu_j} \right|^2 - \left| T_{h_1h_2,\mu_0^{(y)}=-1/2,\mu_j} \right|^2 \right]}{\displaystyle\sum_{h_1h_2\mu_j} \left[\left| T_{h_1h_2,\mu_0^{(y)}=1/2,\mu_j} \right|^2 + \left| T_{h_1h_2,\mu_0^{(y)}=-1/2,\mu_j} \right|^2 \right]}. \tag{2.132}$$

The transformation of the quantization axis from the z-axis to the y-axis is accomplished by

$$T_{h_1h_2\mu_0^{(y)}\mu_j} = \sum_{h_0} D^{1/2}_{h_0\mu_0^{(y)}}(\hat{R}_{yz}) T_{h_1h_2h_0\mu_j}. \tag{2.133}$$

As already mentioned, reorientation of h_1 and h_2 does not change the observables unless their polarization quantities are under consideration:

$$\sum_{h_1h_2h_0\mu_j} \left| T_{h_1h_2h_0\mu_j} \right|^2 = \sum_{\eta_1^{(a)}\eta_2^{(b)}h_0\mu_j} \left| \sum_{h_1h_2} D^{*1/2}_{h_1\eta_1^{(a)}}(\Omega_{az}) D^{*1/2}_{h_2\eta_2^{(b)}}(\Omega_{bz}) T_{\eta_1^{(a)}\eta_2^{(b)}h_0\mu_j} \right|^2, \tag{2.134}$$

where Ω_{az} (Ω_{bz}) denotes the rotation of the quantization axis from the z-axis to an arbitrary direction a (b).

Chapter 3

Validation of distorted wave impulse approximation

Contents

3.1 Introduction

Although the DWIA has been applied successfully to analyses of the knockout reactions [28–47], it should be compared with more sophisticated reaction theories to validate its framework,. The most precise one will be the Faddeev-Alt-Grassberger-Sandhas formulation (FAGS) [52–54], which gives the exact solution of the three-body Schrödinger equation with a fixed Hamiltonian. Recently FAGS has been applied to the (p,pN) reactions [48–51]. In Ref. [48, 49] the DWIA formalism is shown to be reduced from the FAGS theory by truncating the higher order terms of multiple-scattering theories. However, such DWIA can be different from the one commonly applied to the knockout reaction analyses, because additional approximations are usually adopted to the latter as introduced in Chapter 2.

Very recently, another reaction model named Transfer-to-the-Continuum (TC), which is a derivative of the continuum-discretized coupled-channels method (CDCC) [55–57], has been developed to describe the knockout reactions[58, 59]. In one aspect, the TC has larger model space compared with that of the DWIA framework; although it is an approximated way, the three-body wave function is properly solved and implemented in the TC formalism, while in the DWIA the three-body problem is reduced to the product of two-body problems by introducing an approximation shown in Eq. (2.25). It should be noted that TC and DWIA rely on the prior- and post-form representations, respectively. On the other hand, at least at this moment, it is quite difficult to take the energy dependence of optical potentials into account in TC and FAGS, while it can be easily taken into account in the DWIA.

Considering these advantages and disadvantages of DWIA, TC and FAGS, it will be important to make a comparison between those three reaction theories for the knockout reaction, to estimate how much consistent results one can obtain from them. For this purpose, a benchmark comparison is made between the DWIA and TC, for the

^{15}C(p,pn)^{14}C reaction at 420 MeV/nucleon (MeV/u) in inverse kinematics illustrated in Fig 3.1, to which FAGS has been already applied in Ref. [51].

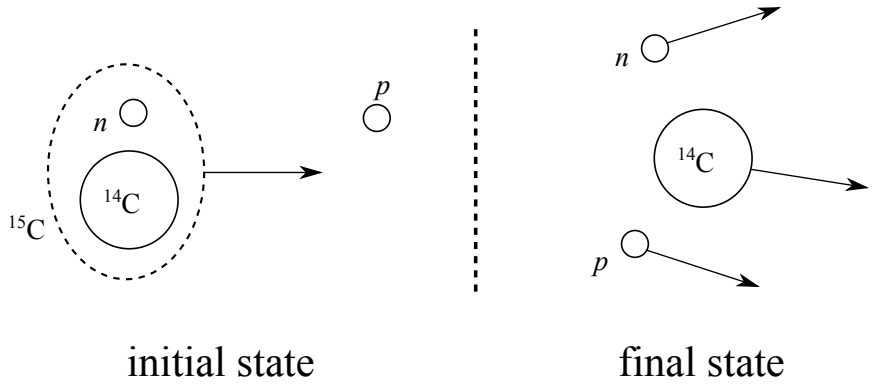

FIGURE 3.1: ^{15}C(p,pn)^{14}C reaction in inverse kinematics.

In the comparison ingredients for the reaction models, e.g., the optical potentials and the single-particle wave function, should be the same as much as possible. However, there exist several limitations; as mentioned the energy dependence of optical potentials cannot be treated in FAGS and TC, for example. The uncertainty originated from the absence of the energy dependence can be estimated by the DWIA calculation, as discussed below. The TC calculation in the present study is performed by A. M. Moro and M. Gómez-Ramos using a modified version of the code FRESCO [72]. The studies in this chapter are shown in Ref. [73].

3.2 Transfer-to-the-Continuum model

In the following, a brief overview of the Transfer-to-the-Continuum model (TC) [58, 59] is given. The T-matrix of TC is described in the prior form:

$$T = \left\langle \Psi_f^{3b(-)} \middle| V_{pn} + V_{p\mathrm{B}} \middle| \phi_{0,\boldsymbol{K}_0}\, \varphi_{nlj\mu_j} \right\rangle, \tag{3.1}$$

where V_{pn} ($V_{p\mathrm{B}}$) is the binary interaction between the target proton and the struck neutron (the core nucleus B). The initial state is described by a product of the plane wave state for the p-A relative motion and the neutron single particle wave function $\varphi_{nlj\mu_j}$, while the final state is given by the exact three-body wave function $\Psi_f^{3b(-)}$. One may replace $\varphi_{0,\boldsymbol{K}_0}$ with $\chi^{(+)}_{0,\boldsymbol{K}_0}$, a distorted wave between p and A, using the Gell-Mann-Goldberger transformation (see Appendix A), i.e.,

$$T = \left\langle \Psi_f^{3b(-)} \middle| V_{pn} + V_{p\mathrm{B}} - U_{p\mathrm{A}} \middle| \chi^{(+)}_{0,\boldsymbol{K}_0}\, \varphi_{nlj\mu_j} \right\rangle, \tag{3.2}$$

where $U_{p\mathrm{A}}$ is the optical potential which generates $\chi^{(+)}_{0,\boldsymbol{K}_0}$.

The three-body wave function $\Psi_f^{3b(-)}$ is expanded by an approximated complete set $\{\tilde{\phi}_i(k_i, \boldsymbol{r})\}$, eigenstates of the p-n binary system including discretized continuum states, in the same way as in the Continuum-Discretized Coupled-Channels method (CDCC):

$$\Psi_f^{3b(-)} \approx \sum_i \tilde{\phi}_i(k_i, \boldsymbol{r}) \chi_i(K_i, \boldsymbol{R}), \tag{3.3}$$

where i denotes the channel index for the p-n system, and k_i (K_i) is the discretized momentum which corresponding to the Jacobi coordinate $\boldsymbol{r}$ ($\boldsymbol{R}$) shown in Fig. 3.2. Detailed procedures of the discretization are given in, for example, Refs. [55–57].

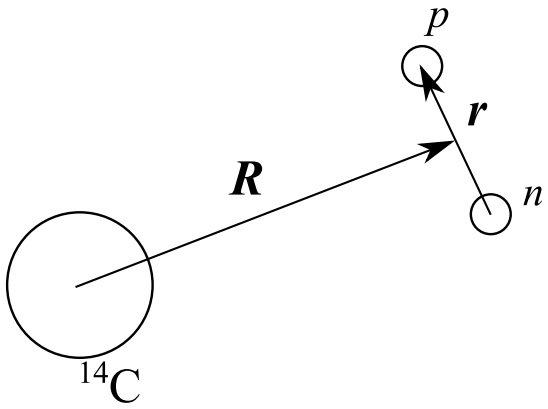

FIGURE 3.2: Jacobi coordinate for (p+n)-^{14}C system.

Inserting Eq. (3.3) into Eq. (3.2), one obtains

$$T \approx \sum_i \left\langle \tilde{\phi}_i \chi_i \middle| V_{pn} + V_{p\mathrm{B}} - U_{p\mathrm{A}} \middle| \chi^{(+)}_{0,\boldsymbol{K}_0} \varphi_{nlj\mu_j} \right\rangle . \tag{3.4}$$

Further simplification called *no-remnant* approximation, in which one neglects the term $V_{p\mathrm{B}} - U_{p\mathrm{A}}$, is made in the present benchmark comparison. The T-matrix of the TC adopted in the present study is thus given by

$$T \approx \sum_i \left\langle \tilde{\phi}_i \chi_i \middle| V_{pn} \middle| \chi^{(+)}_{0,\boldsymbol{K}_0} \varphi_{nlj\mu_j} \right\rangle . \tag{3.5}$$

3.3 Result and discussion

3.3.1 Numerical inputs

In the present study, the ^{15}C(p,pn) reaction at 420 MeV/u is considered. The struck neutron is assumed to be bound in a 1s single-particle orbital with separation energies of S_n = 1.22 MeV, 5 MeV and 18 MeV. S_n = 1.22 MeV is a realistic value which is also adopted in the previous work with FAGS [51], while artificial neutron separation energies S_n = 5 MeV and 18 MeV are also considered to see the S_n dependence of the consistency between the DWIA and TC. The single-particle wave function of the knocked out neutron, $\varphi_{nlj\mu_j}(R)$, is the second eigenstate with the s-wave of the binding problem with a central Woods-Saxon shaped potential:

$$V_{\mathrm{WS}}(R) = \frac{V_0}{1 + \exp\left[\frac{R - r_0 B^{1/3}}{a_0}\right]} \tag{3.6}$$

with the radius and diffuseness parameters being r_0 = 1.25 fm and a_0 = 0.65 fm, respectively; those are used also in the FAGS study [51]. The mass number of the residue ^{14}C is denoted by B. The depth parameter V_0 is adjusted so as to reproduce S_n.

In this chapter the factorized form of the DWIA T-matrix given in Eq. (2.93), which is one of the most simplified forms of the DWIA, is adopted in the DWIA

calculation. The elementary p-n cross section is calculated with the Reid93 potential [74], which is an updated version of the Reid soft core potential [75]. The Reid93 potential reproduces p-p and p-n phase shift up to 350 MeV with $\chi^2/N_{\rm data} = 1.03$. On the other hand, in the TC calculation, Reid93 potential is directly used as V_{pn} in Eq. (3.6).

As for the distorting potentials for the p-A, p-B and n-B binary systems, the EDAD2 parameter set of the Dirac phenomenology [76, 77] is adopted.

3.3.2 Comparison between DWIA and TC

In this section the comparison of the longitudinal momentum distribution (LMD) of the reaction residue ^{14}C between the DWIA and TC is discussed. LMD is defined by

$$\frac{d\sigma}{dK^{\rm A}_{{\rm B}z}} = 2\pi \int dK^{\rm A}_{{\rm B}b} K^{\rm A}_{{\rm B}b} \frac{d\sigma^{\rm A}}{d\boldsymbol{K}^{\rm A}_{\rm B}}, \tag{3.7}$$

which is equivalent to Eq. (2.55). The superscript A indicates that the quantities are evaluated in the ^{15}C-rest (A-rest) frame in the present reaction system.

In Fig. 3.3(a) LMD of the ^{15}C$(p,pn)^{14}$C reaction at 420 MeV/u is shown. The

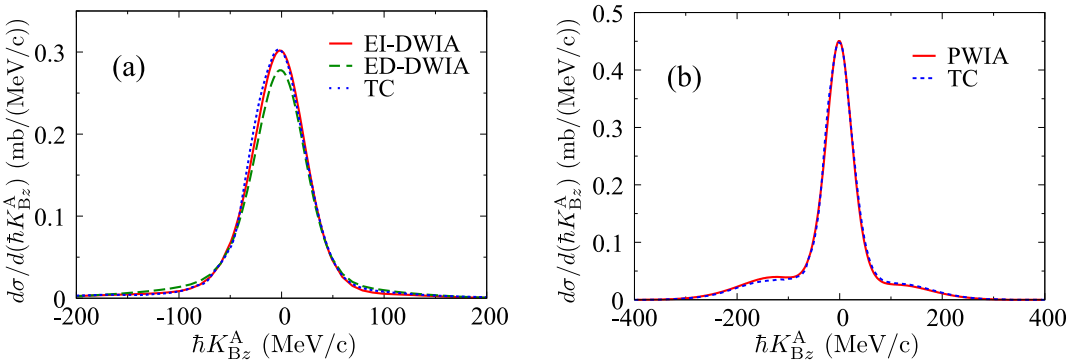

FIGURE 3.3: Longitudinal momentum distribution (LMD) of ^{15}C$(p,pn)^{14}$C reaction with $S_n = 1.22$ MeV. (a) LMD calculated with the energy-independent DWIA (solid), the energy-dependent DWIA (dashed) and TC (dotted). Details are given in the text. (b) Same as (a) but with all distorting potentials switched off.

solid, dashed and dotted lines are the results of the energy-independent DWIA (EI-DWIA), the energy-dependent DWIA (ED-DWIA) and TC, respectively. In obtaining LMD, the scattering energy of the emitted proton and neutron are expected to vary with a broad range satisfying the energy and momentum conservation of the total system. Since the optical potential has the scattering energy dependence, such energy dependence should be included, as done in ED-DWIA. On the other hand, as mentioned in Sec. 3.1, it is very difficult to include the energy dependence in the TC (and FAGS). In order to investigate the uncertainty coming from the absence of that, the EI-DWIA calculation has been performed by fixing the distorting potentials of the emitted proton and neutron at that of 210 MeV, as in the TC calculation.

Finding from Fig. 3.3(a) are summarized as follows.

1. The EI-DWIA and TC results are in almost perfect agreement both in shape and magnitude, giving only 0.3 % difference at the peak.

2. By introducing the energy dependence of the optical potentials, LMD is reduced by about 8 %. Therefore at least for this reaction system, the energy dependence of optical potentials has a minor effect on LMD.

As it is easily expected from the excellent agreement between the EI-DWIA and TC in Fig. 3.3(a), both theories in the plane-wave limit, where all optical potentials are switched off, perfectly agree with each other, as seen in Fig. 3.3(b). It should be noted that the agreement in the plane wave limit is worth investigating because a difference between the DWIA and TC may appear, since the distortion suppresses the tail region of LMD.

In Fig 3.4, results of the same calculation as in Fig. 3.4(a) but with artificial neutron separation energies $S_n = 5$ MeV (Fig. 3.4(a)) and 18 MeV (Fig. 3.4(b)) are shown. One can find that the EI-DWIA and TC agree fairly well in both $S_n = 5$ MeV

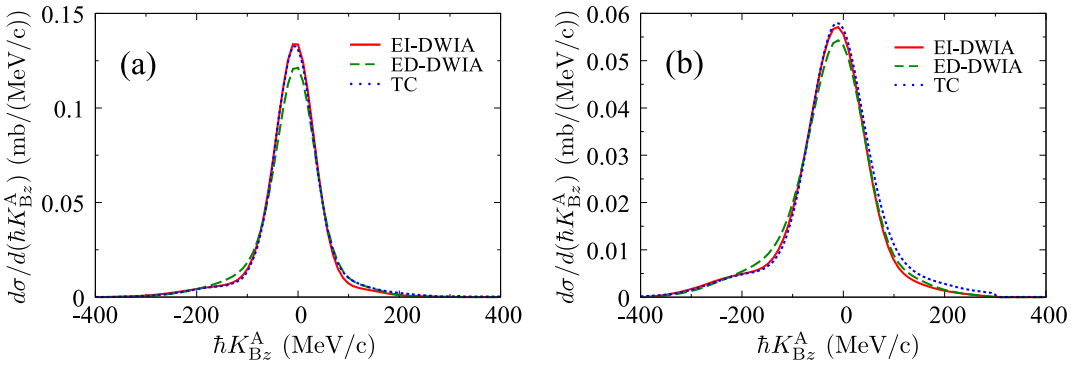

FIGURE 3.4: The same as Fig. 3.3(a) but with $S_n = 5$ MeV (a) and 18 MeV (b).

and 18 MeV cases, giving 0.8 % and 1.4 % difference in peak height, respectively. The reduction of LMD by introducing the energy dependence of the optical potentials is found to be 9.3 % (4.9 %) when S_n =5 MeV (18 MeV). This may cause some uncertainties on deduced spectroscopic factors though analyses on experimental data.

It is also found that even though the knockout process is triggered by a 420 MeV/u proton, the asymmetric shape of LMD due to the asymmetry of the phase space and the attraction of the distorting potentials, which is discussed in detail in Ref. [46], gradually develops as S_n increases.

3.3.3 Comparison between TC and FAGS

In this section, the comparison of the transverse momentum distribution (TMD) between TC and FAGS is given. The following definition of TMD is adopted:

$$\frac{d\sigma}{dK^{\rm A}_{{\rm B}x}} = \int dK^{\rm A}_{{\rm B}y}\, dK^{\rm A}_{{\rm B}z} \frac{d\sigma}{d\boldsymbol{K}^{\rm A}_{\rm B}}, \tag{3.8}$$

which is the same as Eq. (2.61). In this comparison, the calculations of TC are carried out with the same input as in the FAGS calculation of Ref. [51] as much as possible. There remain, however, some differences, which are summarized as follows.

1. Both non-relativistic and relativistic kinematics are assumed in the TC calculation, while only the former is assumed in the FAGS calculations, as shown in Fig. 3.5.

2. The Koning-Delaroche nucleon-nucleus optical potential parameters [78] are adopted as p-^{15}C, p-^{14}C and n-^{14}C distorting potentials. The scattering energy for evaluating the Koning-Delaroche potential is fixed at 200 MeV, following Ref. [51].

3. The CD-Bonn nucleon-nucleon potential [79] is employed in the FAGS calculation, while Reid93 [74] is adopted in the TC calculation. Although different nucleon-nucleon potentials are employed, the comparison will make sense because those two potentials are known to yield the same on-shell observables up to 350 MeV.

The solid line in Fig. 3.5(a) shows the FAGS result taken from Fig. 4 of Ref. [51]. The dashed and dot-dashed lines correspond to TC calculations with and without the

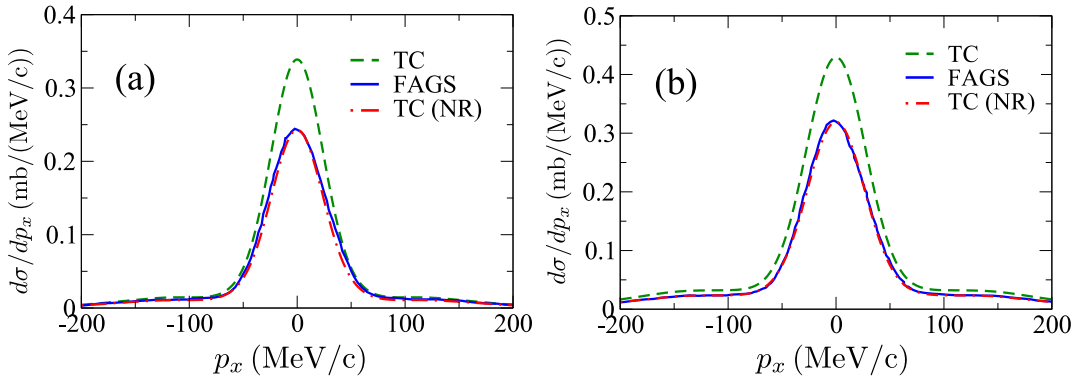

FIGURE 3.5: (a) The transverse momentum distribution (LMD) of ^{15}C(p,pn)^{14}C reaction at 420 MeV/u. The FAGS result taken from Fig. 4 of Ref. [51] is given by the solid line. The dashed and dot-dashed lines are the results of TC with and without relativistic corrections, respectively. (b) Same as (a) but all optical potentials are switched off.

relativistic correction on kinematics, respectively. Figure. 3.5(b) is the same as (a) but with all distorting potentials switched off. One finds that the TC and FAGS agree completely with each other, when non-relativistic kinematics are taken. It should be noted, however, that the relativistic correction increase the magnitude significantly by about 30 % keeping the shape of the distribution. The relativistic kinematics should therefore be necessary for the quantitative discussion such as spectroscopic studies from the analysis of (p,pN) experiments.

3.4 Summary

The longitudinal and transverse momentum distributions of the ^{15}C(p,pn)^{14}C at 420 MeV/u in inverse kinematics have been investigated with three different theories, i.e., the distorted wave impulse approximation (DWIA), the transfer-to-the-continuum model (TC) and the Faddeev-AGS formalism (FAGS).

The longitudinal momentum distributions calculated with the energy-independent DWIA (EI-DWIA) and TC are found to be in excellent agreement, in both shape and height. Evaluated longitudinal momentum distributions of EI-DWIA and TC agree with each other in a wide range of neutron separation energies S_n, giving only 0.3 %, 0.8 % and 1.4 % differences at the peak when S_n = 1.22 MeV, 5 MeV and 18 MeV, respectively. The effect of the energy dependence of optical potentials, which

is not taken into account in TC and FAGS, has also been investigated by comparing the results between the EI-DWIA and the energy-dependent DWIA (ED-DWIA). It was shown that by taking the energy dependence of optical potentials into account properly, the momentum distribution decreases by 8.0 %, 9.3 % and 4.9 % for S_n = 1.22 MeV, 5 MeV and 18 MeV, respectively. The difference is not serious but should be important for quantitative discussions, particularly when deducing spectroscopic factors from knockout cross sections.

The result for the transverse momentum distribution of the ^{14}C residue with Non-relativistic TC is in good agreement with the FAGS result. Another finding is the inclusion of relativistic corrections on kinematics increases the cross section by about 30 %, which shows the necessity of the relativistic treatment of the kinematics.

From those studies, it is concluded that the DWIA, TC and FAGS yield consistent results for the neutron knockout cross sections, once the same input and kinematics are adopted. Therefore those reaction theories can be reliably applied to spectroscopic studies using the nucleon knockout reactions, which is partially discussed in Chap. 7.

Chapter 4

^{120}Sn(p,$p\alpha$)^{116}Cd reaction and the validity of the factorization approximation

Contents

4.1 Introduction

As a new topic of clustering studies, the α clustering on the surface of Sn isotopes is theoretically predicted [10]. This prediction itself is quite interesting because it has been believed that α cluster states may appear mainly in the light mass region, at most ^{40}Ca or ^{44}Ti [80]. Furthermore, as discussed in Ref. [10], the existence of α clusters on the nuclear surface of heavy nuclei may give a significant impact on the deduced slope coefficient of the nuclear equation of state. It should be noted, however, that as already emphasized in Chap. 1, and Sec. 5.1, the surface amplitude of the cluster wave function should be the measure of the clustering.

In this chapter, following an already published paper [35], the proton induced α knockout reaction from ^{120}Sn, i.e., ^{120}Sn(p,$p\alpha$)^{116}Cd, at 392 MeV is investigated within the DWIA framework. One of the subjects in the present study is to see how clearly the α cluster amplitude at the nuclear surface can be probed. Another goal of this chapter is to test the validity of the asymptotic momentum approximation (AMA) and the factorization approximation introduced in Sec. 2.1.3, which has been adopted in various cases of the knockout reaction analyses.

In the present study, the validity of the AMA is examined by means of the local semiclassical approximation (LSCA) [66–68] which is also described in Sec. 2.1.3. As argued in Ref. [42], the AMA and the factorization approximation may become questionable when the target is heavy and the distortion effect is strong; the local momenta of the incoming proton and the emitted proton and α can be much different from the asymptotic ones. Therefore the ^{120}Sn(p,$p\alpha$)^{116}Cd reaction will be a good test case for the validity of the AMA and the factorization approximation.

4.2 Theoretical setup

In the present study, the following is assumed in the DWIA framework.

1. The spin-orbit interactions of distorting potentials are omitted.
2. The average prescription for the nucleon-nucleon effective interaction, Eq. (2.87), is adopted.
3. The on-shell approximation of the final energy prescription, Eq. (2.81), is employed.

The triple differential cross section (TDX) is then given by

$$\frac{d^3\sigma}{dE_1^{\mathrm{L}}d\Omega_1^{\mathrm{L}}d\Omega_2^{\mathrm{L}}} = J_{\mathrm{G}\to\mathrm{L}}F_{\mathrm{kin}}S_{nl}^{\alpha}\frac{(2\pi)^2}{\hbar v_i}\frac{(2\pi\hbar^2)^2}{\mu_{12}}\frac{1}{2l+1} \times\sum_m\left|\int d\boldsymbol{R}\,F_{\boldsymbol{K}_i}(\boldsymbol{R})\varphi_{nlm}(\boldsymbol{R})\sqrt{\frac{d\sigma_{12}}{d\Omega_{12}}(\theta_{12}(\boldsymbol{R}),E_{12}(\boldsymbol{R}))}\right|^2, \tag{4.1}$$

where the distorted-wave factor $F_{\boldsymbol{K}_i}(\boldsymbol{R})$ is defined by

$$F_{\boldsymbol{K}_i}(\boldsymbol{R}) = \chi^{*(-)}_{1,\boldsymbol{K}_1}(\boldsymbol{R})\,\chi^{*(-)}_{2,\boldsymbol{K}_2}(\boldsymbol{R})\,\chi^{(+)}_{0,\boldsymbol{K}_0}(\boldsymbol{R})\,e^{-i\alpha_R\boldsymbol{K}_0\cdot\boldsymbol{R}}. \tag{4.2}$$

Equation (4.1) is equivalent to Eq. (2.91) but some indices are dropped since α is spinless, and superscript α is added to the spectroscopic factor and the cluster wave function.

The scattering energy $E_{12}(\boldsymbol{R})$ of the elementary p-α scattering process is determined by the final energy prescription as shown in Sec. 2.1.4.

Once the asymptotic momenta $\boldsymbol{K}_0$, $\boldsymbol{K}_1$ and $\boldsymbol{K}_2$ are used instead of the local momenta, in other words, the AMA is adopted instead of the LSCA, Eq. (4.1) is reduced to the factorized form

$$\frac{d^3\sigma}{dE_1^{\mathrm{L}}d\Omega_1^{\mathrm{L}}d\Omega_2^{\mathrm{L}}} = J_{\mathrm{G}\to\mathrm{L}}F_{\mathrm{kin}}S_{nl}^{\alpha}\frac{(2\pi)^2}{\hbar v_i}\frac{(2\pi\hbar^2)^2}{\mu_{12}}\frac{1}{2l+1} \times\frac{d\sigma_{12}}{d\Omega_{12}}(\theta_{12},E_{12})\sum_m\left|\int d\boldsymbol{R}\,F_{\boldsymbol{K}_i}(\boldsymbol{R})\varphi_{nlm}(\boldsymbol{R})\right|^2. \tag{4.3}$$

4.3 Numerical input

The cluster wave function $\varphi^{\alpha}_{nlm}(\boldsymbol{R})$ is obtained by solving the Schrödinger equation

$$\left[-\frac{\hbar^2}{2\mu}\nabla^2_{\boldsymbol{R}} + V_{\alpha\mathrm{B}}(R) - \varepsilon_\alpha\right]\varphi^{\alpha}_{nlm}(\boldsymbol{R}) = 0, \tag{4.4}$$

where $V_{\alpha\mathrm{B}}$ is a Woods-Saxon shaped central potential

$$V_{\alpha\mathrm{B}}(R) = \frac{V_0}{1+\exp\left[\frac{R-r_0B^{1/3}}{a_0}\right]} \tag{4.5}$$

with the range parameter $r_0 = 1.27$ fm and the diffuseness parameter $a_0 = 0.67$ fm. The depth parameter V_0 is determined so as to reproduce $\varepsilon_\alpha = -4.81$ MeV. α is assumed to be bound in the $4S$ orbital. In the following, $S^{\alpha}_{40} = 0.022$ taken from Ref. [81] is adopted.

Since θ_{12} and E_{12} in wide range are needed, instead of using the experimental data of $d\sigma_{12}/d\Omega_{12}$, the microscopic folding model [82] with the phenomenological density of α and the Melbourne nucleon-nucleon g-matrix interaction [63] is adopted to obtain the p-α differential cross section. As shown in Fig. 4.1, the calculated p-α differential cross section agrees well with the experimental data at 297 MeV [83] and 500 MeV [84], without any adjustable parameter.

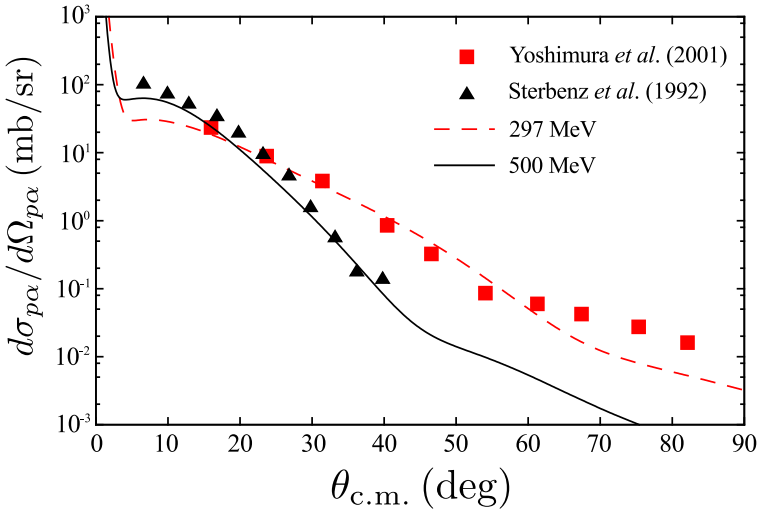

FIGURE 4.1: Comparison between p-α differential cross section calculated by the folding model and the experimental data at 297 MeV [83] and 500 MeV [84].

For the distorting potential of the emitted α, for the consistency with the p-α system, an optical potential obtained by the double-folding model [85] is employed. The Melbourne nucleon-nucleon g-matrix interaction [63] and the nuclear density of ^{116}Cd calculated by the Hartree-Fock method in the same way as in Ref. [69] are adopted. It should be noted that, because of the discrete ambiguities [86, 87] of optical potentials, it is quite difficult to determine the low-energy scattering potential of α phenomenologically. In order to avoid such ambiguities, there exist many attempts [88–90] to construct α-nucleus optical potentials microscopically with the double folding model. It should be noted, however, that in the present study both real and imaginary parts of the α optical potential are evaluated without any free adjustable parameters, in contrast to the preceding works. For distorting potentials of the proton in the initial and the final state, the EDAD1 optical potential parameter of the Dirac phenomenology [76, 77] is adopted.

The nonlocal correction on the proton and α distorted waves are taken into account by multiplying these by the so-called Perey factor [91]

$$F_P(R) = \left[1 - \frac{\mu\beta^2}{2\hbar^2}U(R)\right]^{-1/2}, \tag{4.6}$$

where μ is the reduced mass of the two-body scattering system and β is the range parameter for nonlocality, which is taken to be $\beta = 0.85$ fm (0.2 fm) for proton (α) [92].

The following three-body kinematics are taken with the Madison convention. The kinetic energy of particles 0 and 1 in the L frame are fixed to be $T_0 = 392$ MeV and $T_1 = 328$ MeV, and the emission angle of particle 1 is $\theta_1^{\rm L} = 43.2°$. As for particle 2, $\theta_2^{\rm L}$ (T_2) is varied around 61°. (59 MeV), giving $\theta_{p\alpha} \sim 56°$ and $E_{p\alpha} \sim 385$ MeV.

The reaction is kept in coplanar; $\phi_1^{\rm L} = 0$, $\phi_2^{\rm L} = \pi$. The relativistic correction on the kinematics is made.

4.4 Validity of LSCA and AMA

In this section the validity of the LSCA and the AMA is discussed. As it has been already examined in Refs [68, 69], at energies higher than 50 MeV, the LSCA works for the propagation of distorted waves for nucleon up to about 1.5 fm. Furthermore, in Ref. [69] it was found that the AMA works at almost the same accuracy as the LSCA. As shown in Eqs. (2.66)–(2.68), the required propagation range for particle 0 is

$$\frac{(A+1)}{A}\frac{A_\alpha}{A_\alpha+1}s = \frac{121}{151}s, \tag{4.7}$$

and for particle 1,

$$\frac{A_\alpha}{A_\alpha+1}s = \frac{4}{5}s. \tag{4.8}$$

Considering the interaction range of $t_{p\alpha}(\boldsymbol{s})$, both the LSCA and the AMA will be valid for particle 0 and 1. On the other hand, for particle 2, such a test has not been done.

When α is emitted to (θ, ϕ)= (61°, 180°), the recoilless condition $\boldsymbol{q} = 0$ MeV/c is satisfied and the residual nucleus B is at rest in the L frame. The validity of the LSCA and the AMA for the distorted wave of the emitted α is tested for the propagation from $\boldsymbol{R}_a$ =(7 fm, 61°, 180°) and $\boldsymbol{R}_b$ =(7 fm, 29°, 0°). As shown in Fig. 4.2, the

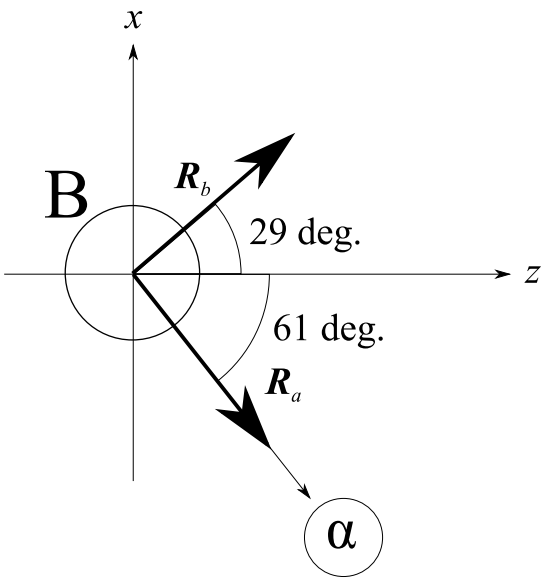

FIGURE 4.2: Directions $\boldsymbol{R}_a$ and $\boldsymbol{R}_b$ in which LSCA and AMA are tested.

direction $\boldsymbol{R}_a$ is taken to be parallel with the emitted direction of α, while that of $\boldsymbol{R}_b$ is taken to be orthogonal to $\boldsymbol{R}_a$.

In Fig. 4.3(a), The real part of the distorted wave of the emitted α along the direction of $\boldsymbol{R}_a$, that with the LSCA, and that with the AMA are shown by the solid, dashed and dotted lines, respectively. The propagation from $\boldsymbol{R}_a$ is considered for the

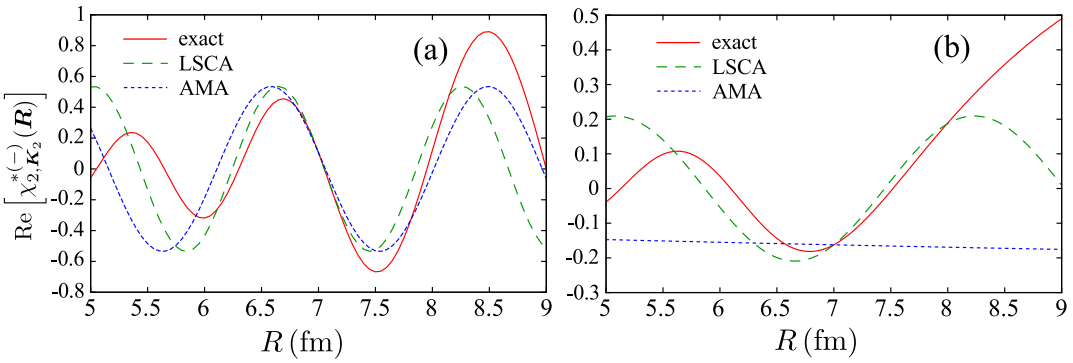

FIGURE 4.3: Validity of LSCA and AMA for emitted α. (a) The real part of the distorted wave of the emitted α is shown in the solid line, while dashed and dotted lines show the approximated results propagated from $\boldsymbol{R}_a$ using the LSCA and the AMA, respectively. (b) same as (a) but with the propagated from $\boldsymbol{R}_b$.

LSCA and the AMA. Since $\boldsymbol{R}_a$ is the fore-side of ^{116}Cd with respect to the emitted α, the distortion effect is small. Therefore as seen in Fig. 4.3(a), both the LSCA and the AMA work fairly well and the propagation within about 0.5 fm can be reproduced. It should be noted that considering the range of the p-α interaction of 2 fm and the coefficient

$$\frac{1}{A_\alpha + 1} = \frac{1}{5} \tag{4.9}$$

of the LSCA and the AMA for the emitted α, the range where these are required to be valid is about 0.4 fm.

In contrast to the weak distortion case, as shown in Fig. 4.3(b) and also suggested in Ref. [42], the AMA fails to describe the propagation of the true distorted wave in the direction of $\boldsymbol{R}_b$ in particular. This is because $\boldsymbol{R}_b$ is orthogonal to $\boldsymbol{K}_2$, which is the asymptotic momentum of the emitted α, and hence the AMA wave function is almost constant as shown in the dotted line in Fig. 4.3(b). On the other hand, the exact distorted wave (solid line) shows some oscillation, since the local momentum of α is attracted by the real part of the optical potential and its direction is no longer parallel with $\boldsymbol{K}_2$. The LSCA (dashed line) succeeds in reproducing the behavior of the exact wave at almost the same level as in the case of Fig. 4.3(a), since in the LSCA the local momentum is taken to be parallel with the flux of the distorted wave as shown by in Eq. (2.65).

As a conclusion, the LSCA well reproduces the behavior of the exact distorted wave both for p and α, even if the distortion effect is strong. On the other hand, at least at the wave function level, the AMA fails to reproduce the exact distorted wave when the distortion is strong and the local momentum differs so much from the asymptotic one. This result may cast a doubt on the factorization in the DWIA framework for the $(p,p\alpha)$ reaction. The validity of the AMA in the TDX point of view is discussed in the following.

4.5 TDX of ^{120}Sn$(p,p\alpha)^{116}$Cd reaction at 392 MeV

The calculated TDX as a function of the recoil momentum defined by

$$p_{\rm R} = \hbar K_{\rm B}^{\rm L} \frac{K_{{\rm B}z}^{\rm L}}{|K_{{\rm B}z}^{\rm L}|} \tag{4.10}$$

is shown in Fig. 4.4. The kinematics of the reaction are given in Sec. 4.3. The solid

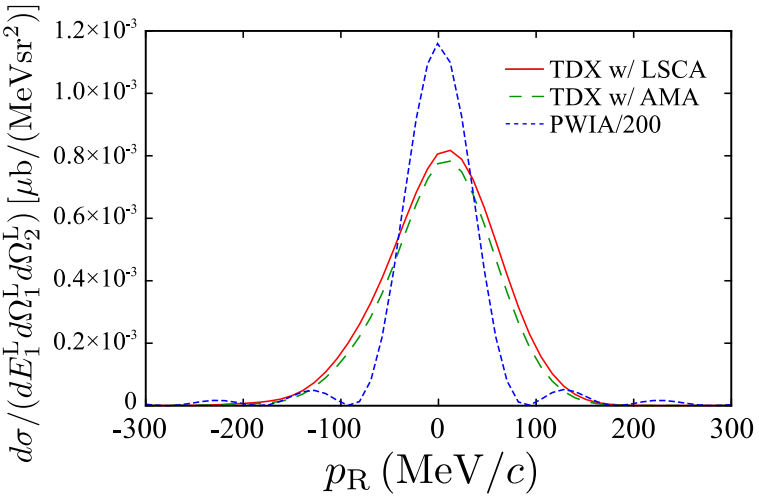

FIGURE 4.4: Triple differential cross section (TDX) of the ^{120}Sn$(p,p\alpha)^{116}$Cd reaction as a function of the recoil momentum. The solid, dashed and dotted lines are TDXs with the LSCA, the AMA and the PWIA divided by 200, respectively.

and dashed lines show the TDXs with the LSCA and the AMA, respectively. It can be seen in Fig. 4.4 that, the TDX with the factorization approximation, which is equivalent to that with the AMA, agrees well with the TDX with the LSCA, even though the distorted wave with the AMA fails to reproduce the proper behavior of the exact distorted wave as discussed in Sec. 4.4. The reason for this is fond to be the strong absorption. As seen also in Fig. 4.4, the PWIA result is more than 200 times larger than the DWIA result, which shows the existence of extremely strong absorption.

4.6 1- and 2-dimensional investigation on probed region

In the first half of this section, as in the same way as in Sec. 5.4, the radial amplitude $I(R)$ defined by

$$\bar{I}(R) \equiv R^2 \varphi_{40}^{\alpha}(R) \left| \int d\Omega \sqrt{\frac{d\sigma_{12}}{d\Omega_{12}}(\theta_{12}(\boldsymbol{R}), E_{12}(\boldsymbol{R}))} F_{\boldsymbol{K}_i}(\boldsymbol{R}) Y_{00}(\Omega) \right| \tag{4.11}$$

is discussed. It should be noted that, as a difference from Eq. (5.7), in Eq. (4.11) the local p-α elementary cross section is included, since the LSCA is considered.

In Fig. 4.5, $\bar{I}(R)$ corresponding to the DWIA, that without the distorting potential U_α of the emitted α and that of the PWIA are shown by the solid, dashed and dotted lines, respectively. Each distribution is normalized to unity at the peak height; in reality $\bar{I}(R)$ of the PWIA is much higher than the others. The kinematics of the reaction in Fig. 4.5 are chosen so as to satisfy the recoilless condition: $p_R = 0$ MeV/c,

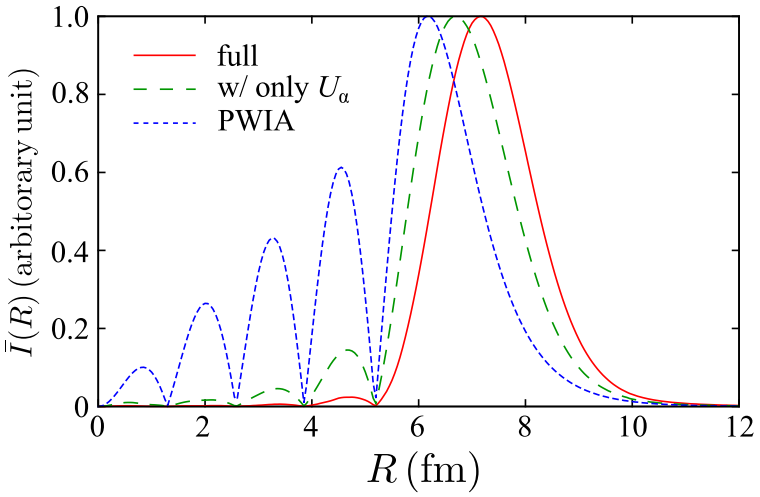

FIGURE 4.5: Radial amplitude of the ^{120}Sn(p,$p\alpha$)^{116}Cd reaction at 392 MeV. The kinematics are chosen to satisfy $p_R = 0$ MeV/c. The solid line shows the result of the DWIA, while the dashed and dotted lines represent the results of the DWIA without the distorting potential U_α of the emitted α, and of the PWIA, respectively. Each line is normalized to unity at the peak height.

which corresponds to the peak of the TDX in Fig. 4.4. It is found that the magnitude of $\bar{I}(R)$ is strongly suppressed in the nuclear interior region, say, $R \leq 6$ fm. Considering the results of the PWIA and the DWIA without U_α, the strong absorption is mainly because of the α-^{116}Cd distorting potential. The difference in the peak positions of $\bar{I}(R)$ seen in Fig. 4.5 is also due to the absorption in the nuclear interior region; since the absorption is stronger in the nuclear interior and weaker in the nuclear surface, the peak positions for the three results different from each other.

For the quantitative discussion on the peripherality of the reaction, in Fig. 4.6 the TDXs calculated with changing the minimum value $R_{\rm min}$ of the integration over R in T-matrix, i.e.,

$$T = \int_{R_{\rm min}}^{\infty} dR\, R^2 \varphi^{\alpha}_{40}(R) \int d\Omega \sqrt{\frac{d\sigma_{12}}{d\Omega_{12}}(\theta_{12}(\boldsymbol{R}), E_{12}(\boldsymbol{R}))} F_{\boldsymbol{K}_i}(\boldsymbol{R}) Y_{00}(\Omega), \tag{4.12}$$

are shown for $R_{\rm min} = 0.0$, 6.0, 6.5, 7.0 and 8.0 fm. It is found that the calculated TDX remains the same for $R_{\rm min} = 0$–5.5 fm, and decreases rapidly as $R_{\rm min}$ increases from 6.0 fm to 8.0 fm. The slight increase in the TDX when $R_{\rm min} = 6.0$ fm is due to the interference of the integrand. From this result one can conclude that only $R \geq 5.5$ fm, the surface region of the α cluster wave function in ^{120}Sn, is probed with high selectivity through the (p,$p\alpha$) reaction. This peripherality is, as already mentioned, suitable for probing α cluster states.

The reason why the distribution of the DWIA result becomes much wider than that of the PWIA shown in Fig. 4.4 can also be understood by the strong absorption in the interior region. The absorption makes the distribution of α cluster wave function narrower and localized around the nuclear surface in the coordinate representation. The distribution of the TDX then becomes wider since the TDX is essentially the squared modulus of the Fourier transform of the α cluster wave function in the plane wave limit, as discussed in Sec. 2.1.5.

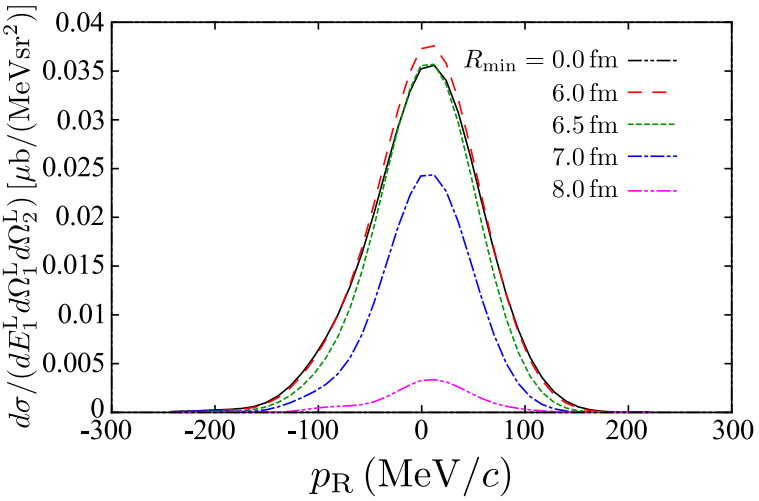

FIGURE 4.6: The peripherality of ^{120}Sn(p,$p\alpha$)^{116}Cd reaction. The figure is the same as Fig. 4.4 but with different $R_{\rm min}$ = 0.0, 6.0, 6.5, 7.0, 8.0 fm, shown by the solid, dashed, dotted, dot-dashed and two-dot-dashed lines, respectively.

For a further detailed analysis, the integrand of Eq. (4.12):

$$J(\boldsymbol{R}) = \sqrt{\frac{d\sigma_{12}}{d\Omega_{12}}(\theta_{12}(\boldsymbol{R}), E_{12}(\boldsymbol{R}))} F_{\boldsymbol{K}_i}(\boldsymbol{R})\varphi^{\alpha}_{40}(\boldsymbol{R}) \tag{4.13}$$

is discussed in the following. Since $J(\boldsymbol{R})$ is complex and a three-dimensional distribution, $|J(\boldsymbol{R})|$ on the z-x plane for y = 0, 1, 3, 5, 6 and 7 fm are shown in Fig. 4.7. For y = 0, 1 and 3 fm, it is clearly seen that the spatial amplitude is localized in the fore-side region of the emitted α at around R =6–9 fm, where the distorted wave of the emitted α is not absorbed and the cluster wave function has a finite magnitude. For $y \geq 5$ fm, the localization of the amplitude is no longer clear on the z-x plane, since for example (x, y, z) = (0, 6 fm, 0) is enough far from the center of the nucleus and is around the nuclear surface, where the absorption is weak. For $y \geq 6$ fm, the amplitude begins to vanish since the α cluster amplitude disappears. From Figs. 4.7(a)–(f), it is found that the ^{120}Sn(p,$p\alpha$)^{116}Cd reaction has high selectivity not only in the radius but also in the direction depending on the emission direction of the knocked out α.

It is also found that the peak at the rear side at around $\boldsymbol{R}$ = (6–8 fm, 120°, 0°) in Fig. 4.7(a) is generated by the focus of the distorted wave of the emitted α due to the strong attraction by ^{116}Cd. Large p-α cross sections are also realized in this focus due to the forward scattering of p-α elementary process. It should be noted that the rear side peak exists only on the z-x plane and rapidly disappears as y increases. This is because the kinematics of the scattered particles are in the coplanar and the focus only lies on the z-x plane. In fact the rear side peak on the z-x plane has a minor contribution to the TDX; about 90 % of the TDX comes from the $x \leq 0$ region. This result suggests that the interference between the amplitude around fore-side and rear-side regions should be very small, and a naïve picture of the (p,$p\alpha$) reaction works; the α particle can be knocked out only from the surface of the target nucleus with the direction of the α emission, since α particle may not travel through the nuclear medium. These features of the (p,$p\alpha$) reaction on heavy nuclei support the validity of the AMA.

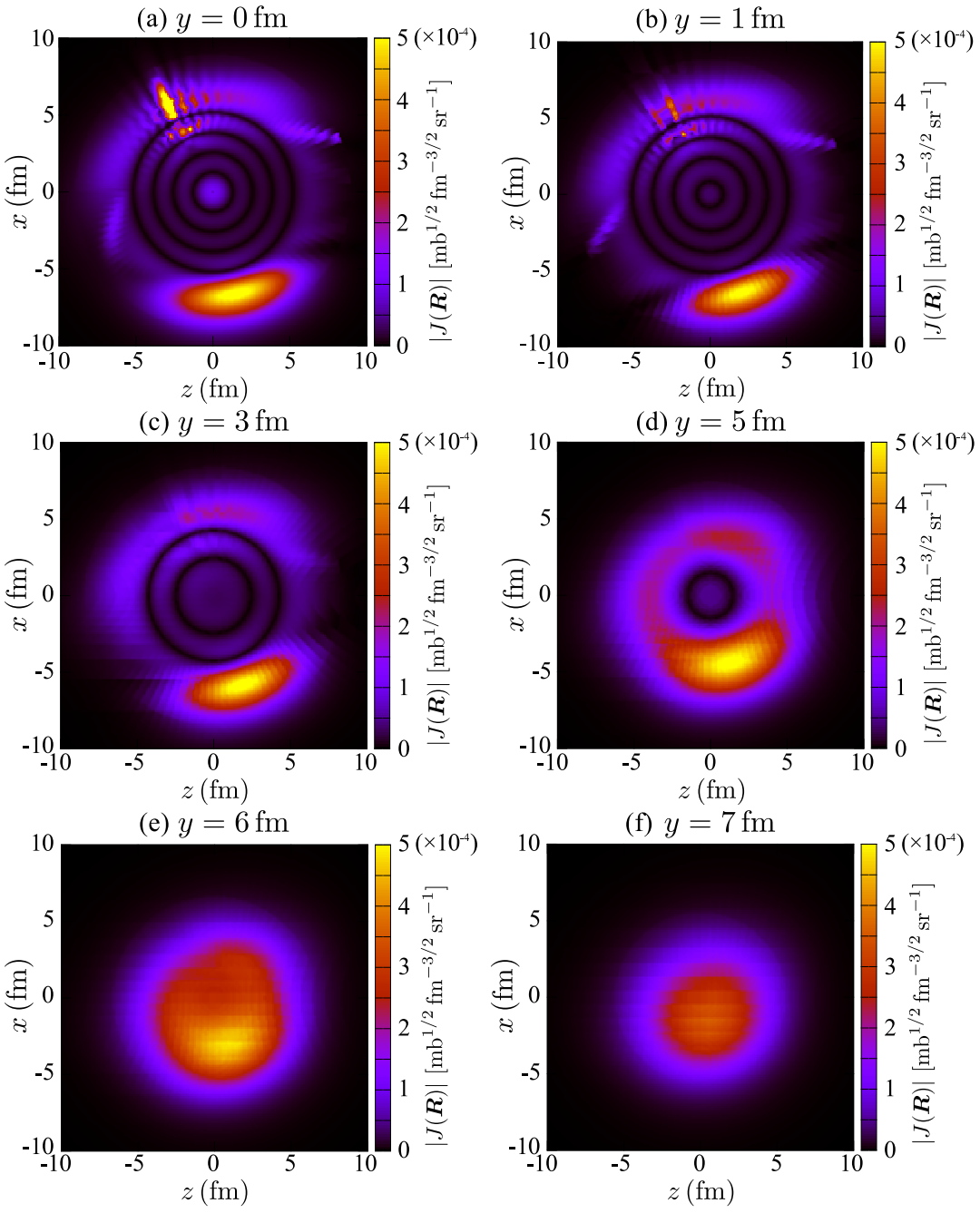

FIGURE 4.7: $|J(\boldsymbol{R})|$ on the z-x plane for y =0, 1, 3, 5, 6, and 7 fm. The kinematical condition is the same as in Fig. 4.5.

4.7 Sensitivity to α cluster wave function

Since a very naïve α cluster wave function is adopted in the present study, it should be worth investigating how the results shown above are affected by changing the α cluster wave function. It is clear that the validity of the LSCA depends only on how distorted waves are described and has nothing to do with the cluster wave function. On the other hand, the validity of the AMA, which leads the factorization approximation, may be affect by the change of cluster wave functions since the validity of the factorization approximation shown above is based on the peripherality of the reaction, which is partly determined by the range of the α cluster wave function. Thus, in this section, the α cluster wave function dependence of TDXs and that of the AMA are discussed.

In Fig. 4.8, TDXs with three types of the α cluster wave function by changing the radius parameter by 10 % are shown; the solid, dashed and dotted lines are TDXs adopting the α cluster wave function with $r_0 = 1.40$ fm, 1.27 fm and 1.14 fm, respectively. The results shown in Fig. 4.8 are obtained with the LSCA. The TDX

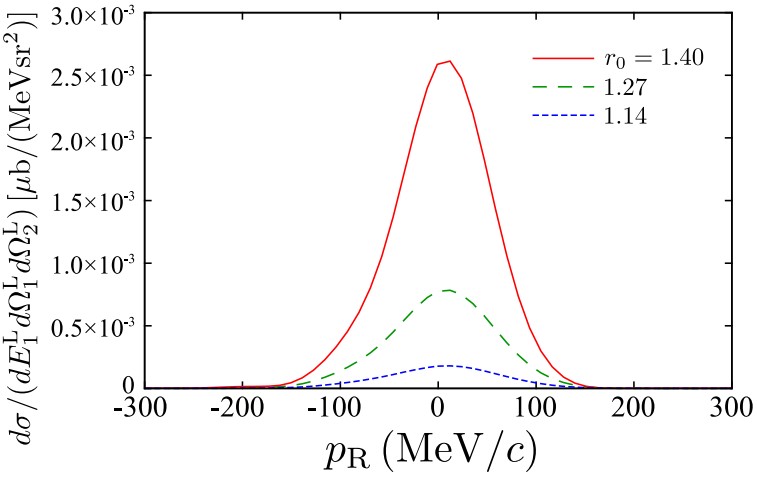

FIGURE 4.8: Dependence of TDXs on the range parameter r_0 of the α biding potential. The solid, dashed and dotted lines are TDXs with $r_0 = 1.40$ fm, 1.27 fm, and 1.14 fm, respectively.

with $r_0 = 1.27$ fm (dashed line) is the original one shown by the solid line in Fig. 4.4. It is found that the 10 % difference of r_0 changes the magnitude of the TDX drastically, by about a factor of three. This can be also understood by the strong absorption in the nuclear interior region; a little extension of the cluster wave function toward the outer region may increase the TDX significantly. It is also found that the TDX with the AMA differs from that with the LSCA by only 6 % at most at the peak at $p_R = 0$ MeV/c of the TDX. Moreover, the qualitative characteristics of the ^{120}Sn$(p,p\alpha)^{116}$Cd reaction shown in Figs. 4.5, 4.6 and 4.7 remain the same, independently of the choices of r_0.

4.8 Summary

In this chapter the ^{120}Sn$(p,p\alpha)^{116}$Cd reaction at 392 MeV has been investigated within the DWIA framework. The validity of the so-called factorization approximation, which has been widely applied to many preceding studies and analyses of the $(p,p\mathrm{N})$ and $(p,p\alpha)$ reactions, is confirmed through the comparison between the DWIA with the AMA and that with the LSCA; the AMA is equivalent to the factorization approximation. Although the AMA itself does not work well in describing the propagation

of the α particle in the region where strong nuclear distortion exists, the TDX of the knockout reaction is not affected because the strong absorption exists in that region. In other words, the transition amplitude of the ^{120}Sn(p,$p\alpha$)^{116}Cd reaction takes place only where the AMA works well. It should be noted, however, that from the analyses in the present study, there remains a possibility that the inaccuracy of the AMA may affect the result when particles propagate with feeling deep real and shallow imaginary potential; that will be realized, for example, in nucleon scattering at low energies.

The strong absorption, that by the α-^{116}Cd distorting potential in particular, makes the ^{120}Sn(p,$p\alpha$)^{116}Cd peripheral, which enables us to probe clearly the α clustering on the surface of nuclei. Furthermore, it was shown that the (p,$p\alpha$) reaction has high selectivity not only the radius but also the direction of the target nucleus; the cluster wave function in only the fore-side region with respect to the emitted α with the radius of 6–9 fm is probed.

It was also shown that the magnitude of the TDX is sensitive to the range of the α cluster wave function, but both the factorization approximation and the peripherality of the reaction are found to be valid for the different types of the α cluster wave function. This result may suggest that it is essential to employ a reliable α cluster wave function for quantitative discussion. Robustness of the validity of the factorization approximation and the peripherality allows one to apply the present reaction framework and discussion to such studies.

Chapter 5

Masking effect in α knockout reaction

Contents

5.1 Introduction

As already stressed in Chap. 1, large spectroscopic factors of an α particle are not necessarily the direct evidence of developed α cluster states because of the *duality*. From this point of view, a large amplitude of a cluster wave function, instead of a large spectroscopic factor, should be the measure of the cluster structure. For this purpose, The ^{16}O(^{6}Li,d)^{20}Ne α transfer reaction has been studied [93] within a three-body reaction theory called the coupled-channels Born approximation (CCBA) [94, 95]. A three-body wave function obtained by the continuum-discretized coupled-channel method (CDCC) [55–57], and an α cluster wave function constructed by a microscopic cluster model (MCM) with the generator coordinate method (GCM) [96–98] are employed. In Ref. [93] the transfer reaction was shown to have rather high sensitivities in the nuclear surface region, and hence it is appropriate for the investigation on the α cluster amplitude around the nuclear surface.

As an alternative method to the transfer reaction, proton-induced α knockout reactions, i.e., the (p,$p\alpha$) reactions, can be considered. In this chapter, the peripherality of the ^{20}Ne(p,$p\alpha$)^{16}O reaction is investigated within the distorted wave impulse approximation (DWIA) framework, which has been applied to α knockout reaction analyses [28–35]. The incident energy dependence of the peripherality of the reaction is also studied considering 100–400 MeV bombarding energies. A new concept, that shows in which region reaction takes place, designated as *the masking function*, is introduced in Sec. 5.2. The studies in this chapter are given in Ref. [99]

5.2 Masking function

In this chapter the spin-orbit part of the distorting potentials is neglected and the following factorized form of DWIA

$$\frac{d^3\sigma}{dE_1^{\mathrm{L}}d\Omega_1^{\mathrm{L}}d\Omega_2^{\mathrm{L}}} = J_{\mathrm{G}\to\mathrm{L}}F_{\mathrm{kin}}\frac{(2\pi)^4}{\hbar v_i}\frac{(2\pi\hbar^2)^2}{\mu_{12}}\sum_l\frac{1}{2l+1}S_{nl}^{\alpha}\frac{d\sigma_{12}}{d\Omega_{12}}(\theta_{12},E_{12}) \times\sum_m\left|\int d\boldsymbol{R}\chi_{1,\boldsymbol{K}_1}^{*(-)}(\boldsymbol{R})\chi_{2,\boldsymbol{K}_2}^{*(-)}(\boldsymbol{R})\chi_{0,\boldsymbol{K}_0}^{(+)}(\boldsymbol{R})e^{-i\alpha_R\boldsymbol{K}_0\cdot\boldsymbol{R}} \times\varphi_{nlm}^{\alpha}(\boldsymbol{R})\right|^2 \tag{5.1}$$

is adopted. Note that particles 0, 1 and 2 correspond to the incident proton, the emitted proton and α, respectively. The reduced T-matrix in the present DWIA framework can be defined by

$$\bar{T}_{nlm} = \int d\boldsymbol{R}\, F_{\boldsymbol{K}_i}(\boldsymbol{R})\varphi_{nlm}^{\alpha}(\boldsymbol{R}), \tag{5.2}$$

where the so-called distorted-wave factor $F_{\boldsymbol{K}_i}$ is defined by

$$F_{\boldsymbol{K}_i}(\boldsymbol{R}) \equiv \chi_{1,\boldsymbol{K}_1}^{*(-)}(\boldsymbol{R})\,\chi_{2,\boldsymbol{K}_2}^{*(-)}(\boldsymbol{R})\,\chi_{0,\boldsymbol{K}_0}^{(+)}(\boldsymbol{R})\,e^{-i\alpha_R\boldsymbol{K}_0\cdot\boldsymbol{R}}. \tag{5.3}$$

Since the norm square of Eq. (5.2) is proportional to the α knockout cross section, it is the equation connecting the structural information on the α cluster wave function φ_{nlm}^{α} and the knockout observables, through a *weighting function* $F_{\boldsymbol{K}}(\boldsymbol{R})$. Therefore it should be worth investigating the property of Eq. (5.2).

The angular part of the cluster wave function can be described by the spherical harmonics as

$$\varphi_{nlm}^{\alpha}(\boldsymbol{R}) = \phi_{nl}^{\alpha}(R)Y_{lm}(\Omega), \tag{5.4}$$

where Ω is the solid angle of $\boldsymbol{R}$. Equation (5.2) is reduced to

$$\bar{T}_{nlm} = \sqrt{4\pi}\int dR\, R^2 D_{lm}(R)\,\phi_{nl}^{\alpha}(R) \tag{5.5}$$

with introducing *the masking function* $D_{lm}(R)$ defined by

$$D_{lm}(R) = \frac{1}{\sqrt{4\pi}}\int d\Omega\, F_{\boldsymbol{K}_i}(\boldsymbol{R})Y_{lm}(\Omega). \tag{5.6}$$

The radial amplitude is then defined by

$$I(R) \equiv R^2\,|D_{lm}(R)|\,\phi_{nl}^{\alpha}(R). \tag{5.7}$$

The masking function $D_{lm}(R)$ is normalized to unity in the following situation.

1. $l = m = 0$,
2. The recoilless condition holds:

$$\boldsymbol{q} = (1-\alpha_R)\boldsymbol{K}_0 - \boldsymbol{K}_1 - \boldsymbol{K}_2 = 0, \tag{5.8}$$

and

3. the plane wave limit of the DWIA discussed in Sec. 2.1.5 is taken.

One sees this as

$$D_{00}(R) \xrightarrow[\text{PWIA}]{} \frac{1}{\sqrt{4\pi}} \int d\Omega\, e^{i\boldsymbol{q}\cdot\boldsymbol{R}} Y_{00}(\Omega), \xrightarrow[\boldsymbol{q}=0]{} 1. \tag{5.9}$$

This corresponds to the case in which there is no absorption effect due to the imaginary part of optical potentials. The squared modulus of the Fourier transform of $\varphi^{\alpha}_{nlm}(\boldsymbol{R})$ is then directly observed as an α knockout cross section. On the other hand, when the absorption of the distorting potentials exists, the masking function shows how the cluster wave function is distorted in the knockout reaction process; it is a weighting function on the radial distribution, as shown in Eq. (5.5).

5.3 Numerical input

In the present study, the α cluster wave function $\varphi^{\alpha}_{nlm}(\boldsymbol{R})$ for the α-^{16}O system is obtained as an eigenstate of the Schrödinger equation

$$\left[-\frac{\hbar^2}{2\mu}\nabla^2_{\boldsymbol{R}} + V_{\alpha\mathrm{B}}(R) - \varepsilon_{\alpha}\right] \varphi^{\alpha}_{nlm}(\boldsymbol{R}) = 0, \tag{5.10}$$

where μ, $V_{\alpha\mathrm{B}}$ and ε_{α} are the reduced mass, the interaction and the eigenenergy of the α-B system, respectively. Both α and ^{16}O are assumed to be inert. As for $V_{\alpha\mathrm{B}}$, a central Woods-Saxon shaped potential of the form

$$f_{\mathrm{WS}}(R) = \frac{V_0}{1 + \exp\left[\frac{R - r_0 B^{1/3}}{a_0}\right]} \tag{5.11}$$

is assumed with $B = 16$, and the radius parameter r_0 and the diffuseness parameter a_0 being $r_0 = 1.25$ fm and $a_0 = 0.76$ fm. Those parameters are taken from Ref. [93], which are adjusted to fit the behavior of $\phi^{\alpha}_{nl}(R)$ in the tail region to that of the microscopic cluster model wave function. The depth parameter V_0 is determined so as to reproduce the α binding energy -4.73 MeV. The orbital angular momentum $l = 0$ and principal quantum number $n = 4$ are assumed [93].

In Fig. 5.1, $\phi^{\alpha}_{40}(R)$ obtained by solving Eq. (5.10) is shown. The solid, dashed and dotted lines are $\phi^{\alpha}_{40}(R)$, $R\phi^{\alpha}_{40}(R)$ and $R^2\phi^{\alpha}_{40}(R)$, respectively. The dashed line is equivalent to the PM1 in Fig. 3 of Ref. [93]. The dotted line in shows a cluster wave function multiplied by R^2, which will be helpful in the following discussion; R^2 appears as a weight on $\phi^{\alpha}_{40}(R)$ in the transition matrix as shown in Eq. (5.5).

As for the distorting potentials for the incoming and the outgoing proton, a global optical potential parameter by Koning and Delaroche [78] is adopted. For the emitted α particle in the final state, the parameter by M. Nolte *et al.* [86] is employed. For the p-α cross section, the microscopic (single) folding model [82] with a phenomenological α density and the Melbourne nucleon-nucleon g-matrix interaction [63] is employed in the same way as in Sec. 4.3.

5.4 Masking effect in ^{20}Ne(p,$p\alpha$)^{16}O reaction

Kinematics of this knockout process are chosen to be $T^{\mathrm{L}}_0 = 392$ MeV, $T^{\mathrm{L}}_1 = 352$ MeV, $\theta^{\mathrm{L}}_1 = 32.5°$, and the kinetic energy of the emitted α particle, T_2, varies for 31–35 MeV,

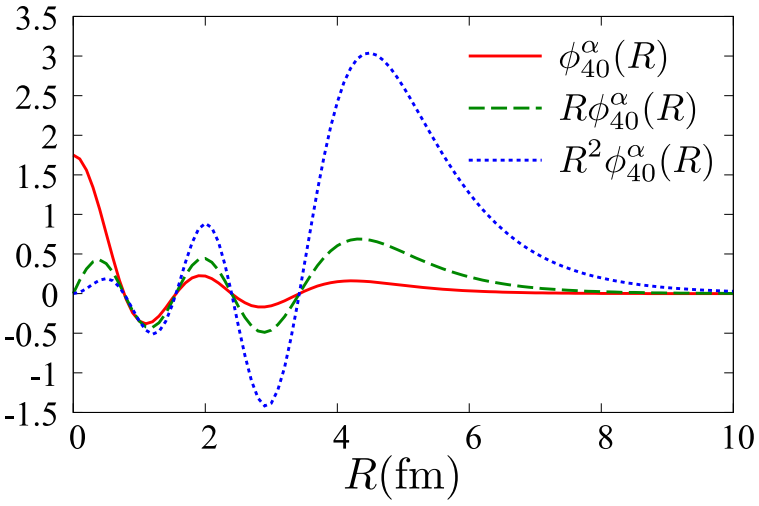

FIGURE 5.1: α cluster wave function of the α-^{16}O system. The solid, dashed and dotted lines are, $\phi^{\alpha}_{40}(R)$, $R\phi^{\alpha}_{40}(R)$ and $R^2\phi^{\alpha}_{40}(R)$, respectively.

with $\theta^{\rm L}_2$ changing 27°–108°, to satisfy the energy and momentum conservation. The azimuthal angle of the emitted particles are taken to be $\phi_1 = 0$ and $\phi_2 = \pi$, i.e., the scattered particles are in coplanar.

In Fig. (5.2) the triple differential cross section (TDX) of Eq. (5.1) is given as a

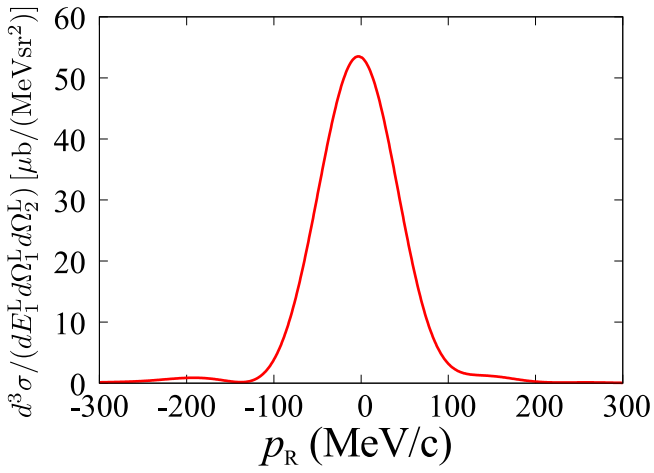

FIGURE 5.2: TDX of the ^{20}Ne(p,$p\alpha$)^{16}O reaction as a function of the recoil momentum p_R. Details are given in the text.

function of the so-called recoil momentum p_R, which is defined by

$$p_R = \hbar K^{\rm L}_{\rm B} \frac{K^{\rm L}_{{\rm B}z}}{\left|K^{\rm L}_{{\rm B}z}\right|}. \tag{5.12}$$

As mentioned in Sec. 2.1.5, the TDX has the peak at $p_R \approx 0$ MeV/c since $l = 0$ in this case. In the following discussion on the masking function, kinematics of the ^{20}Ne(p,$p\alpha$)^{16}O reaction are fixed to $p_R = 0$ MeV/c ($T^{\rm L}_2 \sim 35.3$ MeV and $\theta^{\rm L}_2 = 67.6°$), which yields the largest TDX.

The modulus of the masking function is shown In Fig. 5.3(a). The solid, dashed, dotted and dot-dashed lines are the masking function, that without all Coulomb interactions (V_C) of distorting potentials, that in the plane wave limit, and the eikonal

masking function, respectively; the eikonal masking function is discussed in Sec. 5.5. As it can be seen by the solid line in Fig. 5.3(a), the masking function strongly suppresses the contribution of the α cluster wave function to the cross section in the nuclear interior region due to the absorption of the distorting potentials. When the plane wave limit is taken, i.e., the plane wave impulse approximation (PWIA) is used, no absorption effect exists, as shown by the dotted line in Fig. 5.3(a).

It is found that despite $|D_{00}(R)|$ and that without V_C agree in the interior region, their asymptotic behavior are different; the former does not reach unity whereas the latter does. This can be understood as follows. Since the kinematics are taken so as to satisfy $\boldsymbol{q} = 0$, $F_{\boldsymbol{K}_i}(\boldsymbol{R}) = 1$ in the asymptotic region (out of the nuclear interaction range) and hence $D_{00}(R) = 0$ if Coulomb interactions are absent. This is the case as shown by the dashed line in Fig. 5.3(a). On the other hand, owing to the long-range nature of Coulomb interactions, $F_{\boldsymbol{K}_i}(\boldsymbol{R})$ and $D_{00}(R)$ suffer from Coulomb phase shift even outside the nuclear potential, which makes $\boldsymbol{q}$ effectively distorted unless $R \to \infty$. This effect of Coulomb interactions is discussed also in Sec. 5.6.

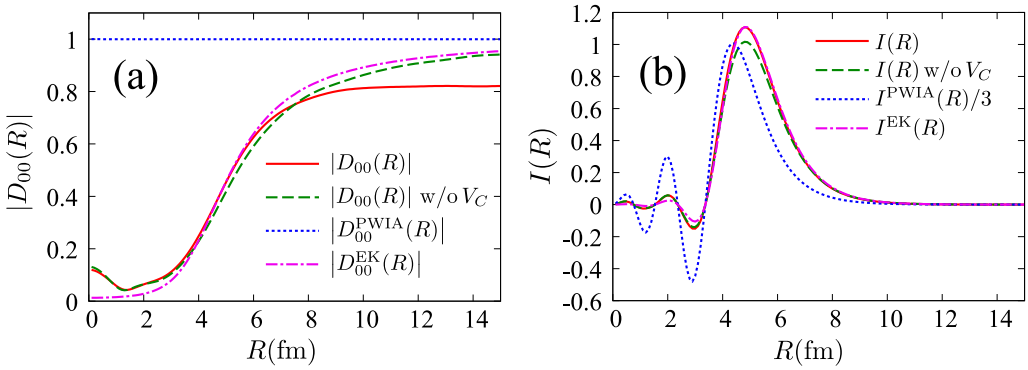

FIGURE 5.3: (a) Masking function of ^{20}Ne(p,$p\alpha$)^{16}O at 392 MeV. The solid, dashed, dotted and dot-dashed lines represent the masking function, that without Coulomb interaction, that of PWIA and the eikonal masking function, respectively. (b) Same as (a) but for the radial amplitude $I(R)$. Details are given in the text.

In Fig. 5.3(b), I show $I(R)$, which is the radial distribution of reaction amplitude defined in Eq. (5.7). The solid, dashed, dotted and dot-dashed lines represent $I(R)$, that without V_C, that of the PWIA divided by 3, and that with the eikonal masking function, respectively. The dotted line in Fig. 5.3(b) is equivalent to the dotted line in Fig. 5.1.

It is clearly seen that the masking effect strongly suppresses the amplitude in the nuclear interior, and the cluster wave function around the nuclear surface contributes to the knockout cross section. As already mentioned in the introduction of this chapter, this is exactly the desired character of reactions for probing how α cluster states are developed. This feature of the α knockout reaction, i.e., high sensitivity on the nuclear surface and low sensitivity in the nuclear interior, will enable us to probe the cluster wave function amplitude around the nuclear surface through the knockout cross section. The surface α amplitude is a direct measure of developed cluster states, since a large α spectroscopic factor does not necessarily imply the existence of a developed α cluster state as mentioned in Sec. 5.1.

5.5 Eikonal masking function and mean free path

For simplification and intuitive interpretation of the masking function, the eikonal approximation is adopted to the distorted waves. The distorted-wave factor is then reduced to

$$\begin{aligned} F_{\boldsymbol{K}_i}(\boldsymbol{R}) \approx F^{\mathrm{EK}}_{\boldsymbol{K}_i}(\boldsymbol{R}) = \exp\left[\frac{1}{i\hbar v_0}\int_{-\infty}^{z} dz'\, U_0(\boldsymbol{R})\right] \\ \times \exp\left[\frac{1}{i\hbar v_1}\int_{z}^{\infty} dz'\, U_1(\boldsymbol{R})\right] \\ \times \exp\left[\frac{1}{i\hbar v_2}\int_{z}^{\infty} dz'\, U_2(\boldsymbol{R})\right] \\ \times e^{i\boldsymbol{q}\cdot\boldsymbol{R}}, \end{aligned} \tag{5.13}$$

where $U(\boldsymbol{R})$ and v_i are the distorting potential and the velocity of particle i, respectively. The momentum $\boldsymbol{q}$ is defined by Eq. (5.8). Further approximation is made as follows.

1. Integration interval is extended to $(-\infty, \infty)$ for all particles.
2. The distorting potentials $U_0(R)$, $U_1(R)$ and $U_2(R)$ are assumed to have the same shape as that of the binding potential $f_{\mathrm{WS}}(R)$.
3. The sum of three depth parameters of the imaginary part W_i with a factor $1/(\hbar v_i)$ is replaced by a free parameter $-C_{\mathrm{abs}}$ which determines the total effective strength of the absorption.

$F^{\mathrm{EK}}_{\boldsymbol{K}_i}(\boldsymbol{R})$ is then approximated by

$$\begin{aligned} F^{\mathrm{EK}}_{\boldsymbol{K}_i}(\boldsymbol{R}) &\approx \prod_{i=0}^{3} \exp\left[\frac{1}{i\hbar v_i}\int_{-\infty}^{\infty} dz'\, U_i(\boldsymbol{R})\right] \\ &\approx \exp\left[\sum_{i=0}^{3}\frac{W_i}{\hbar v_i}\int_{-\infty}^{\infty} dz'\, f_{\mathrm{WS}}(R)\right] \\ &\approx \exp\left[-C_{\mathrm{abs}}\int_{-\infty}^{\infty} dz'\, f_{\mathrm{WS}}(R)\right]. \end{aligned} \tag{5.14}$$

Note that the term $\exp[i\boldsymbol{q}\cdot\boldsymbol{R}]$ in Eq. (5.13) has been dropped since the kinematics are fixed so as to satisfy $\boldsymbol{q} = 0$. The real part of the optical potentials is also neglected since it has no effect on the modulus of $D^{\mathrm{EK}}_{00}(R)$ in the eikonal approximation. In the end the eikonal masking function and the eikonal radial amplitude are defined by

$$D^{\mathrm{EK}}_{lm}(R) = \frac{1}{\sqrt{4\pi}}\int d\Omega \exp\left[-C_{\mathrm{abs}}\int_{-\infty}^{\infty} dz'\, f_{\mathrm{WS}}(R)\right] Y_{lm}(\Omega), \tag{5.15}$$

$$I^{\mathrm{EK}}(R) \equiv R^2 \left|D^{\mathrm{EK}}_{lm}(R)\right| \phi^{\alpha}_{nl}(R). \tag{5.16}$$

The absorption strength parameter C_{abs} is determined to be 0.69 fm^{-1} so as $I^{\mathrm{EK}}(R)$ to reproduce the peak height of $I(R)$.

As shown in Fig. 5.3(a), the dot-dashed line agrees well with the solid line for $4 \lesssim R \lesssim 6$ fm, and deviates from it $R \gtrsim 6$ fm. This asymptotic behavior of the dot-dashed line is due to the absence of Coulomb interactions and $|D^{\mathrm{EK}}_{00}(R)|$ cannot reproduce the asymptotics of $|D_{00}(R)|$. However, it should be noted that as shown in

Fig. 5.3(b), $I^{\rm EK}(R)$ (dot-dashed line) reproduces $I(R)$ well for $R \gtrsim 4$ fm, where $I(R)$ has a finite amplitude. This results show that the eikonal approximation works well in describing the property of the masking function for the present $(p,p\alpha)$ reaction. It should be noted that the deviation of $|D_{00}^{\rm EK}(R)|$ from $|D_{00}(R)|$ for $R \gtrsim 6$ fm gives small but finite difference between $I^{\rm EK}(R)$ and $I(R)$; the difference at 8 fm is about 6%.

$C_{\rm abs}$ should be related to the mean free path (MFP) λ of the scattering particles. From the relation between the MFP and the imaginary part of an optical potential [100]

$$\frac{1}{\lambda} = \frac{2}{\hbar v} W(R), \tag{5.17}$$

the MFP for the $(p,p\alpha)$ reaction can be defined by

$$\frac{1}{\lambda_{\rm ko}} = \sum_{i=0}^{2} \frac{2}{\hbar v_i}, W(R). \tag{5.18}$$

and for the MFP with the eikonal approximation, one finds

$$\frac{1}{\lambda_{\rm ko}^{\rm EK}} = 2C_{\rm abs}\, f_{\rm WS}(R). \tag{5.19}$$

In Fig. 5.4, $1/\lambda_{\rm ko}$ and $1/\lambda_{\rm ko}^{\rm EK}$ are shown by the solid and dashed lines, respectively. It is found that the latter is smaller than the former. This indicates overshooting of

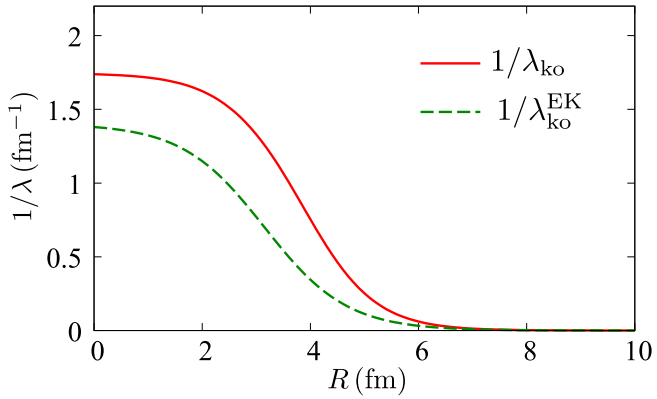

FIGURE 5.4: The comparison between $\lambda_{\rm ko}$ (solid line) and $\lambda_{\rm ko}^{\rm EK}$ (dashed line).

the integral over z' due to the extension of the interval of the integrations made from Eq. (5.13) to (5.14).

In Fig. 5.5 the T_0 dependence of $C_{\rm abs}$ is shown. T_1, T_2, $\theta_1^{\rm L}$ and $\theta_2^{\rm L}$ are chosen so as to give $p_R = 0$ MeV/c, and the reaction is kept in coplanar; $\phi_1^{\rm L} = 0$, $\phi_2^{\rm L} = \pi$. It is found that T_0 dependence of $C_{\rm abs}$ is moderate above 200 MeV, where quasi-free (impulse) picture of the knockout reaction is valid. On the other hand, below 200 MeV, $C_{\rm abs}$ increases rapidly as T_0 decreases because of the small MFPs of low energy particles, that for α in particular. This behavior of $C_{\rm abs}$ for small T_0 will indicate the breakdown of the quasi-free (impulse) picture of the knockout reaction.

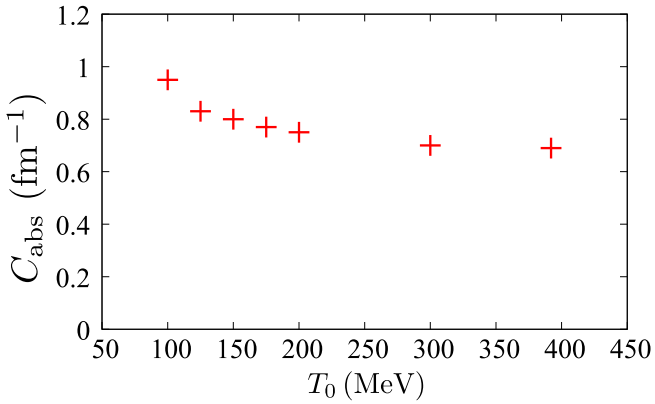

FIGURE 5.5: Incident energy dependence of the absorption strength parameter.

5.6 Coulomb effect on masking function

As shown in Fig. 5.3(a), long-ranged Coulomb interactions prohibit the masking function from reaching unity, Even though the kinematics of the knockout process are fixed so as to satisfy $\boldsymbol{q} = 0$. This effect is significant when the charge of the target nucleus is large. From this point of view, the peripherality and the masking function of the ^{120}Sn$(p,p\alpha)^{116}$Cd reaction at 392 MeV is investigated in this section. The α cluster wave function is constructed in the same method as above but with $r_0 = 1.25 \times 116^{1/3}$ fm and $\varepsilon_\alpha = -4.81$ MeV. The three-body kinematics are chosen to be $T_0 = 392$ MeV, $T_1 = 328$ MeV, $\theta_1^{\rm L} = 43.2°$, and $T_\alpha = 51$ MeV ($\theta_\alpha = 61°$), which satisfies $\boldsymbol{q} = 0$ MeV/c.

In Fig. 5.6 $D_{00}(R)$ and $I(R)$ of the ^{120}Sn$(p,p\alpha)^{116}$Cd are shown in the same way as in Fig. 5.3(a) and Fig. 5.3(b), respectively. The obtained masking function for

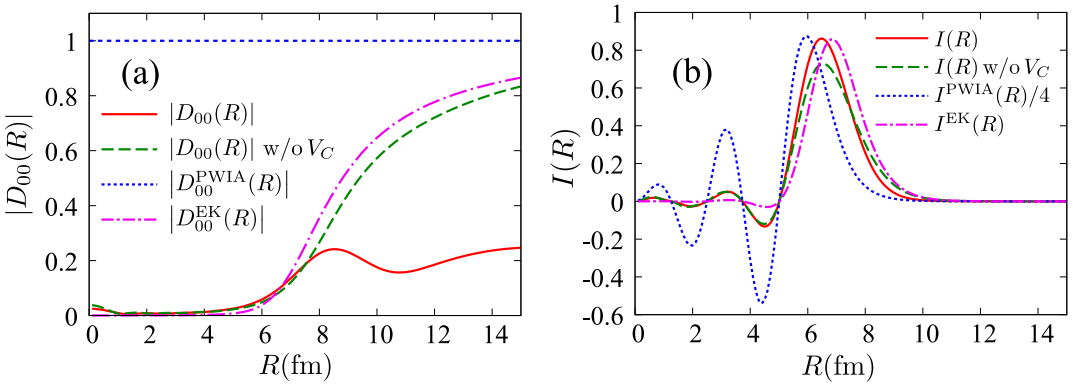

FIGURE 5.6: Same as Fig. 5.3(a) and Fig. 5.3(b) but for the ^{120}Sn$(p,p\alpha)^{116}$Cd reaction.

this system (the solid line in Fig. 5.6(a)) is strongly suppressed in the asymptotic region by Coulomb interactions. On the other hand, $D_{00}(R)$ without V_C (the dashed line) approaches to unity, as well as the eikonal masking function $D_{00}^{\rm EK}(R)$. It should be noted, however, that despite Coulomb interactions are strong and the eikonal masking wave function fails to reproduce the proper asymptotic behavior of $D_{00}(R)$, $I(R)$ and $I^{\rm EK}(R)$ can agree relatively well as shown in Fig. 5.6(b), giving reliable radial distributions of the reaction amplitude. This is because the masking function in the asymptotic region has little overlap with the cluster wave function.

5.7 Summary

The ^{20}Ne(p,$p\alpha$)^{16}O reaction at 100–392 MeV was investigated with the distorted wave impulse approximation framework. We have introduced a new concept named *the masking function*, which describes the absorption effect due to the distorting potentials of the incident p and of emitted p and α. Through the analyses on the masking function of the reaction, it is clearly shown that the α knockout reaction is peripheral and suitable for probing the α cluster amplitude in the nuclear surface, which should be the direct measure of spatially developed α cluster states.

By adopting the eikonal approximation to the masking function, one can reproduce the functional behavior of the masking function in a simplified way with one free parameter which represents the total effective absorption strength. The incident energy dependence of the absorption parameter was shown to be weak above 200–400 MeV, where the quasi-free knockout reaction picture is considered to be valid. On the other hand, below 200 MeV it increases as the incident energy decreases, reflecting the small mean free paths of low energy particles.

As an extreme case of strong Coulomb interaction, the ^{120}Sn(p,$p\alpha$)^{116}Cd reaction at 392 MeV has been investigated. It is shown that even if the eikonal masking function fails to reproduce the proper asymptotic behavior owing to the long-range nature of Coulomb interactions, the radial distribution of reaction amplitude is reproduced well. This is due to the fact that the eikonal masking function agrees with the true masking function in the nuclear interior, where the cluster amplitude exists.

Chapter 6

α clustering in ^{10}Be

Contents

6.1 Introduction

In recent years microscopic theories have been established for describing the cluster states ranging from the molecular-like states in Be isotopes [101–116] to the gas-like Hoyle state (0_2^+) of ^{12}C [11, 24, 117, 118] The agreement of the physical quantities such as the binding energy and the (charge) radius between the theoretical predictions and the experimental data suggests the α clustering in ^{10}Be. As discussed in Chap. 1, however, due to *the duality* of the cluster and the shell model wave function [23, 26], a large magnitude of the α cluster wave function on the nuclear surface should be a probed through the reaction. Since it has been shown that the α knockout reaction is very peripheral not only for heavy targets as shown in Chap. 4 but also light nuclei as shown in Chap. 5, the α knockout reaction can be the direct probe to the α cluster amplitude in the nuclear surface region. It should be noted, however, in the preceding α knockout reaction studies phenomenological α cluster wave functions are adopted. For the quantitative discussion, it should be necessary to apply the microscopic cluster theory to the DWIA framework.

In this chapter the ^{10}Be(p,$p\alpha$)^{6}He at 250 MeV is investigated. The microscopic description of the α clustering in ^{10}Be is discussed by adopting an extended version of the Tohsaki-Horiuchi-Schuck-Röpke (THSR) wave function [11] to the microscopic description of ^{10}Be and ^{6}He residue [116]. Utilizing the flexibility of the THSR model, the α cluster state of ^{10}Be is smoothly evolved artificially from the compact shell model limit to the spatially developed gas-like limit, and the reaction observables with them are investigated. This chapter is based on Ref. [119].

6.2 THSR wave function and overlap function

In the present study the latest version of the THSR wave function [**Zhao17**] is employed, including the di-neutron paring term for describing ^{10}Be and ^{6}He

$$\left|\Psi(^{10}\mathrm{Be})\right\rangle = \hat{P}^J_{MK}\left(C^\dagger_\alpha\right)^2\left[(1-\gamma)c^\dagger_{n,\uparrow}c^\dagger_{n,\downarrow}+\gamma c^\dagger_{2n}\right]|\mathrm{vac}\rangle\,, \tag{6.1}$$

$$\left|\Psi(^{6}\mathrm{He})\right\rangle = \hat{P}^J_{MK}C^\dagger_\alpha\left[(1-\gamma)c^\dagger_{n,\uparrow}c^\dagger_{n,\downarrow}+\gamma c^\dagger_{2n}\right]|\mathrm{vac}\rangle\,, \tag{6.2}$$

where $\hat{P}^J_{MK}$ is the angular momentum projection operator [120] for restoring the rotational symmetry of the wave function, and $|\mathrm{vac}\rangle$ is the vacuum state. $C^\dagger_\alpha$ is the α cluster creation operator defined by

$$C^\dagger_\alpha = \int d\boldsymbol{R} \exp\left(-\frac{R_x^2+R_y^2}{\beta^2_{\alpha,xy}} - \frac{R_z^2}{\beta^2_{\alpha,x}}\right) \times \int d\boldsymbol{r}_1 \dots d\boldsymbol{r}_4\, \psi(\boldsymbol{r}_1-\boldsymbol{R}) a^\dagger_{\sigma_1,\tau_1}(\boldsymbol{r}_1) \dots \psi(\boldsymbol{r}_4-\boldsymbol{R}) a^\dagger_{\sigma_4,\tau_4}(\boldsymbol{r}_4), \tag{6.3}$$

where $\boldsymbol{R}$ is the generator coordinate of the α cluster. The creation operator of the single nucleon state of ith nucleon is described by $\psi(\boldsymbol{r}_i-\boldsymbol{R})a^\dagger_{\sigma_i,\tau_i}$, where σ_i and τ_i are spin and isospin of ith nucleon, respectively. The spatial part of the single particle wave function has the Gaussian form

$$\psi(\boldsymbol{r}) = (\pi b^2)^{-3/4} \exp[-r^2/(2b^2)]. \tag{6.4}$$

The range parameter b is fixed to be $b = 1.35$ fm. $\beta_{\alpha,xy}$ ($\beta_{\alpha,z}$) is the deformed parameter for the x-y plane (z-direction) which describes the nonlocalized motion of the α particles. Both $\beta_{\alpha,xy}$ and $\beta_{\alpha,z}$ are determined by the variational calculation, unless they are artificially fixed.

There are two types of the creation operator adopted for the valence neutrons. One is the operator for the unpaired neutrons defined by the similar way as Eq. (6.3)

$$c^\dagger_{n\sigma} = \int d\boldsymbol{R}_n \exp\left(-\frac{R_{n,x}^2+R_{n,y}^2}{\beta_{n,xy}} - \frac{R_{n,z}^2}{\beta^2_{n,z}}\right) \times \int d\boldsymbol{r}_i (\pi b^2)^{-3/4} e^{(-)^m \phi(\boldsymbol{R}_n)} e^{-(\boldsymbol{r}_i-\boldsymbol{R}_n)^2/(2b^2)}\, a^\dagger_\sigma(\boldsymbol{r}_i). \tag{6.5}$$

Note that the phase $\exp[(-)^m\phi(\boldsymbol{R}_n)]$ corresponding to the third component of the orbital angular momentum, m, of the valence neutron and the azimuthal angle of $\boldsymbol{R}_n$, $\phi(\boldsymbol{R}_i)$, appears to describe the intrinsic π-orbit negative parity state for the valence neutrons. Details can be found in Ref. [115, 116].

The other is the creation operator for the paring configuration of the valence neutrons

$$c^\dagger_{2n} = \int d\boldsymbol{R}_{2n} \exp\left(-\frac{R_{2n,x}^2+R_{2n,y}^2}{\beta^2_{2n,xy}} - \frac{R^2_{2n,z}}{\beta^2_{2n,z}}\right) \int d\boldsymbol{r}_i d\boldsymbol{r}_j \times (\pi b^2)^{-3/4} e^{-(\boldsymbol{r}_i-\boldsymbol{R}_{2n})^2/(2b^2)} a^\dagger_\uparrow(\boldsymbol{r}_i) \times (\pi b^2)^{-3/4} e^{-(\boldsymbol{r}_j-\boldsymbol{R}_{2n})^2/(2b^2)} a^\dagger_\downarrow(\boldsymbol{r}_j), \tag{6.6}$$

where $\boldsymbol{R}_{2n}$, $\beta_{2n,z}$, and $\beta_{2n,xy}$ are the generator coordinate for di-neutron pair, the deformed parameter for z and that for the other directions, respectively. The pairing (Eq. (6.6)) and un-paring (Eq. (6.5)) components of the two valence neutrons are mixed by the variational parameter γ as shown in Eqs. (6.1) and (6.2).

Although the formation of the α clusters are assumed by the α creation operator, the antisymmetrization effect is taken into account in the THSR wave function. As a result, the α spectroscopic factor deduced from the THSR wave function becomes less than unity in general. This is a great advantage of adopting the microscopic cluster model because the cluster wave function amplitude at the nuclear surface is obtained theoretically and further normalization, such as the normalization to the observed

cross section, is not necessary in principle.

In order to obtain the α cluster wave function from the THSR wave functions of ^{10}Be and ^{6}He, an approximation introduced in Ref. [121] is adopted in the present study. In this method an approximation to the reduced width amplitude (RWA) $ay(a)$ at the channel radius a is approximated by $y^{\rm app}(a)$, which is obtained by the overlap function between the wave function of ^{10}Be and a Brink-Bloch wave function as

$$\begin{aligned} |ay(a)| &\approx ay^{\rm app}(a) \\ &\equiv \frac{1}{\sqrt{2}} \left(\frac{6\times 4}{10\pi b^2} \right)^{1/4} \left| \left\langle \Phi(^{10}\mathrm{Be}) \,\middle|\, \Psi^{J\pi}_{\rm BB}(^{6}\mathrm{He}, \alpha, S=a) \right\rangle \right| \end{aligned} \tag{6.7}$$

where $\Phi(^{10}\mathrm{be})$ and $\Phi^{J\pi}_{\rm BB}$ are the THSR wave function of ^{10}Be and the Brink-Bloch-type wave function of ^{6}He-α two body system, respectively. It should be noted that, as it is shown in Ref. [121], this approximation works well only the nuclear surface and fails to give the proper behavior in the nuclear interior. However, thanks to the peripherality of the α knockout reaction, Eq. (6.7) can be safely applied in the ^{10}Be(p,$p\alpha$)^{6}He reaction analyses.

As for the reaction part, the factorized form of the DWIA, as shown in Eq. (2.93), is adopted. It should be emphasized again, that the α spectroscopic factor is no longer needed because the cluster wave function is constructed microscopically.

6.3 Input and result

As for the structure part, following Ref. [109], the Volkov No.2 interaction [122] is employed as the central term and the G3RS as the spin-orbit term [123] of the nucleon-nucleon interaction. All the variational parameters of the THSR wave function are optimized by variational calculation for the ground state energies of ^{10}Be and ^{6}He.

As for the reaction part, the following kinematics of the ^{10}Be(p,$p\alpha$)^{6}He at 250 MeV are considered with the Madison convention is adopted. Particle 1 is emitted with $T_1 = 180$ MeV, $\theta_1 = 60.9^\circ$, and $\phi_1 = 0^\circ$. T_2 and θ_2 vary with satisfying the energy and momentum conservation. When $\theta_2 = 76^\circ$ and $T_2 = 62.5$ MeV, the recoilless condition is satisfied. The scattering energy and the angle of the p-α binary collision are $E_{p\alpha} \sim 242$ MeV and $\theta_{p\alpha} \sim 76^\circ$ at the recoilless condition, respectively. Because there do not exist experimental differential cross section data for the p-^{10}Be, p-^{6}He, and α-^{6}He systems at intermediate energies, the single- and double-folding models [82, 85] with the Melbourne g matrix interaction [63] are employed to obtain the required optical potentials. For the double folding calculation of the α-^{6}He potential, the target density approximation of Ref. [85] is adopted.

The binding energy of -61.4 MeV is obtained for the ground state of ^{10}Be by the variational calculation in the THSR framework. As for the root-mean-square change radius, the obtained value of 2.31 fm agrees well with the experimental value of 2.36 fm [124]. In Fig. 6.1(b) the charge distribution of ^{10}Be with the optimized variational parameters $\beta_{\alpha,xy} = 0.1$ fm and $\beta_{\alpha,z} = 2.6$ fm is shown. As a comparison, the charge distribution of ^{10}Be with artificial values of $\beta_{\alpha,z} = 1.0$ fm and 6.0 fm are shown in Figs. 6.1(a) and (c), respectively. The result with $\beta_{\alpha,z} = 1.0$ fm ($\beta_{\alpha,z} = 6.0$ fm) corresponds to shell-like (gas-like) structure. In the case of $\beta_{\alpha,z} = 1.0$ fm the wave function is close to the $SU(3)$-shell-model limit and the two clusters are overlapping each other, giving the strong antisymmetrization effect. Since the approximation of Eq. (6.7) is adopted in the present study, it is dangerous to make $\beta_{\alpha,z}$ too much small. That is the reason why $\beta_{\alpha,z} = 1.0$ fm is chosen as the shell-model-like case.

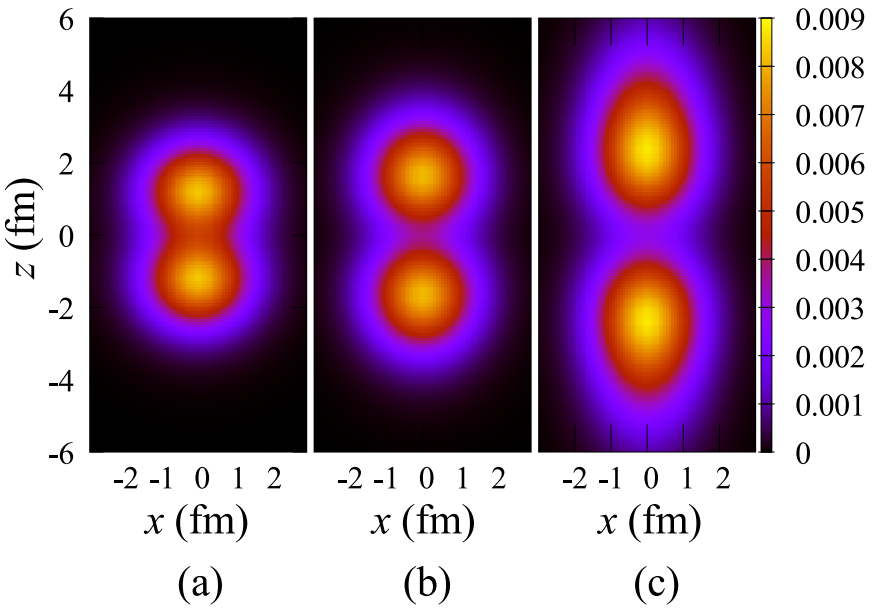

FIGURE 6.1: The charge distribution of ^{10}Be with $\beta_{\alpha,z} = 1.0$ fm (a), 2.6 fm (b), and 6.0 fm (c).

In contrast, as shown in Fig. 6.1(c), very dilute structure of ^{10}Be is obtained with $\beta_{\alpha,z} = 6.0$ fm.

In Fig 6.2, the approximated RWAs obtained by Eq. (6.7) using the THSR wave functions of ^{10}Be and ^{6}He are shown. The solid, dashed and dotted lines are the RWAs with $\beta_{\alpha,z} = 1.0$ fm, 2.6 fm and 6.0 fm, respectively. One may clearly find that

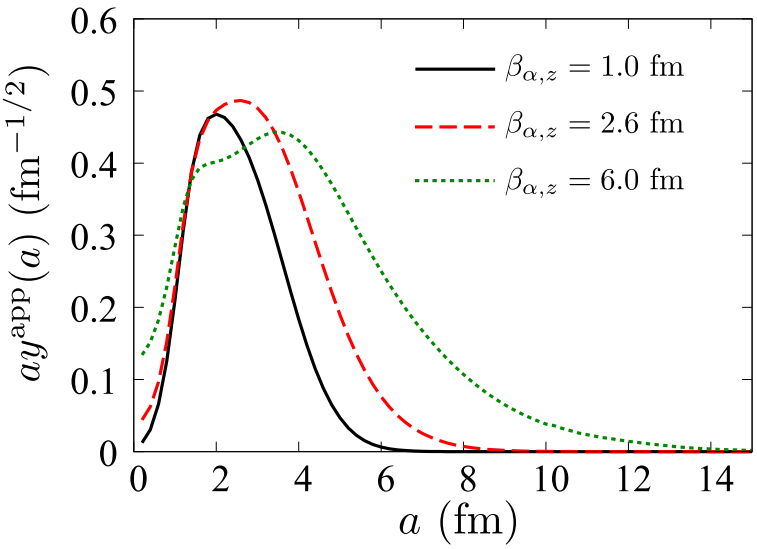

FIGURE 6.2: The approximated reduced width amplitude for $\beta_{\alpha,z} = 1.0$ fm (solid line), 2.6 fm (dashed line) and 6.0 fm (dotted line).

RWAs also show a compact (dilute) behavior with $\beta_{\alpha,z} = 1.0$ fm (6.0 fm).

Adopting those RWAs to the DWIA calculations, the triple differential cross section (TDX) of the ^{10}Be$(p,p\alpha)^{6}$He at 250 MeV is obtained. In Fig. 6.3 the TDXs with $\beta_{\alpha,z} = 1.0$ fm, 2.6 fm, and 6.0 fm are shown by the solid, dashed, and dotted lines,

respectively, as a function of the recoil momentum defined by

$$p_{\rm R} = \hbar K_{\rm B}^{\rm L} \frac{K_{{\rm B}z}^{\rm L}}{|K_{{\rm B}z}^{\rm L}|}. \tag{6.8}$$

The magnitude of TDXs are quite different. The ratio of the TDX with $\beta_{\alpha,z} = 6.0$ to

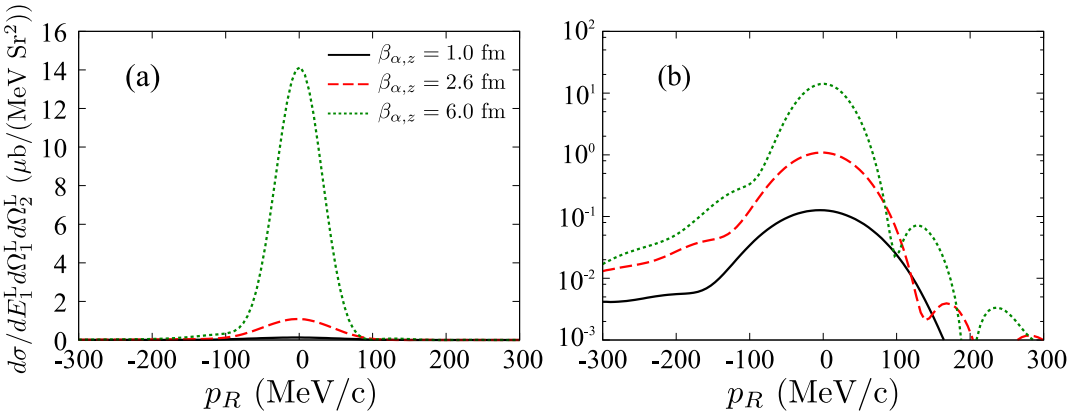

FIGURE 6.3: (a) Triple differential cross section (TDX) of the ^{10}Be(p,$p\alpha$)^{6}He at 250 MeV. The solid, dashed and dotted lines are TDX with $\beta_{z,\alpha} = 1.0$ fm, 2.6 fm and 6.0 fm, respectively. (b) Same as (a) but plotted in the logarithmic scale.

that with $\beta_{\alpha,z} = 2.6$ is about 13.0 and the TDX with $\beta_{\alpha,z} = 2.6$ to that with $\beta_{\alpha,z} = 1.0$ is about 8.6 at the peak height. These results show that the TDXs of the α knockout reaction have the high sensitivity to the size of the cluster structures. As already mentioned, by adopting the microscopic cluster theory to the DWIA framework, the magnitude of the TDXs can be predicted. Therefore one may pin down how much the α clustering is developed from the TDXs of the (p,$p\alpha$) reaction.

By looking at Figs. 6.2 and 6.3, one may find the peripherality of the reaction. The RWAs around the nuclear surface are reflected to the TDXs with emphasis whereas the inner part has less contribution. In fact, as the α knockout from ^{120}Sn and ^{20}Ne discussed in Chaps 4 and 5, the ^{10}Be(p,$p\alpha$)^{6}He is very peripheral. In Fig. 6.4 the transition matrix density (TMD) of the ^{10}Be(p,$p\alpha$)^{6}He is shown. The solid, dashed and dotted lines are the TMDs with RWAs of $\beta_{\alpha,z} = 1.0$ fm, 2.6 fm and 6.0 fm, respectively. The TMD can be interpreted as the radial strength (not amplitude) of the reaction. Details of the TMD are given in Appendix D. It is clearly seen that only the middle and tail regions are probed through the knockout reaction; the nuclear interior region has little contribution to the cross section because of the absorption and R^2 weight in the transition matrix. Thanks to the peripherality of the reaction, it is possible to probe the α cluster amplitude at the nuclear surface. It is an essential property for probing α clustering because the α clusters in nuclear interior is not well defined and they does not necessarily indicate the clustering due to the antisymmetrization. It should be noted that in Ref. [121] it is shown that in ^{8}Be system, the antisymmetrization effect is small for $a \geq 3$–4 fm, and in that region the approximation of Eq. (6.7) is valid. Assuming this to be true also for ^{10}Be, one may safely conclude that the approximation of Eq. (6.7) causes little error in the TDXs. For the $\beta_{\alpha,z} = 1.0$ fm case, the error coming from the approximation to the RWA is not clear, but still it will be safe to expect for the much smaller cross section when $\beta_{\alpha,z} = 2.6$ fm.

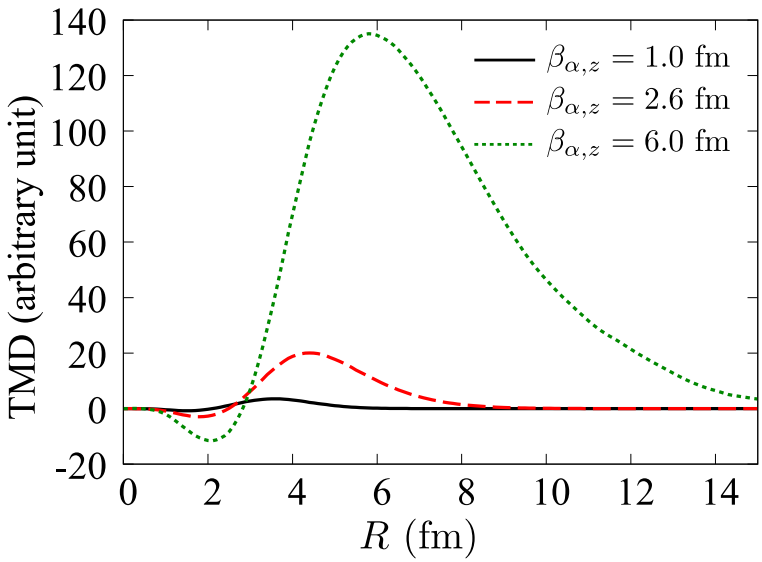

FIGURE 6.4: Transition matrix density (TMD) of the ^{10}Be(p,$p\alpha$)^{6}He reaction. The solid, dashed and dotted lines are the TMDs with RWAs of $\beta_{\alpha,z}$ = 1.0 fm, 2.6 fm and 6.0 fm, respectively.

6.4 Summary

In this chapter the ^{10}Be(p,$p\alpha$)^{6}He at 250 MeV has been investigated. The structure of ^{10}Be and ^{6}He are described microscopically by the THSR wave function. The α cluster wave function in ^{10}Be is obtained as an approximated RWA from the THSR wave functions as introduced in Ref. [121]. The obtained α cluster wave function includes the probability of the existence of an α particle; it is not normalized to unity.

Adopting the cluster wave function obtained from the THSR wave functions to the DWIA framework, it is clearly shown that the α cluster amplitude around the nuclear surface is probed through the ^{10}Be(p,$p\alpha$)^{6}He reaction. Therefore, the α knockout cross section is a direct measure of the development of the α cluster states. Furthermore, by changing the parameter of the THSR wave function, the shell-model-like and gas-like cluster cases of ^{10}Be has been investigated. Due to the peripherality of the α knockout reaction, the knockout cross section has very high sensitivity to the size of the cluster states and one may pin down α-α distance from the α knockout cross sections.

Chapter 7

Spectroscopy of nuclei via nucleon knockout reactions

Contents

7.1 Introduction

In this chapter the current situation of the nuclear spectroscopy is summarized. The single-particle (s.p.) state of the nucleon in the nucleus is characterized by the principal number n, the orbital angular momentum $\boldsymbol{l}$, and the total angular momentum $\boldsymbol{j} = \boldsymbol{l} + 1/2$. In addition to these quantum numbers, the spectroscopic factor (amplitude) shown in Eq. (2.37) is the key quantity which shows how much s.p. state is realized. In order to pin down the quantum numbers and the spectroscopic factors of the s.p. states, the nucleon knockout reaction, (p,pN), has been utilized [36–47].

The quantum numbers n and l, and the spectroscopic factor can be deduced through the analyses of the (p,pN) cross sections, as discussed in Sec. 7.2. The current status of the knockout reaction analyses for the nucleon spectroscopy is discussed in Sec. 7.3. Thanks to the so-called Maris effect [125–128], the total angular momentum j can be fixed by looking at the so-called energy sharing distribution of the vector analyzing power of the (p,pN) process, as shown in Appendix F.

7.2 Nucleon knockout reaction and spectroscopic factor

The most exclusive cross section of the (p,pN) reaction is the triple differential cross section (TDX). As discussed in Sec.2.1.5, the plane wave limit of the TDX is proportional to the squared Fourier transform of the s.p. wave function. Therefore the orbital angular momentum l can be determined by the shape of the TDX.

For the DWIA calculations in this section, the factorized form of DWIA given by Eq. (2.93) is adopted. The p-p differential cross section is obtained by the Franey-Love nucleon-nucleon effective interaction [62] with the final state prescription of the on-shell approximation defined by Eq. (2.81). The optical potential by Koning and Delaroche [78] is adopted as the distorting potentials. The s.p. wave function of the struck proton is obtained by solving the bound state problem of the Schrödinger

equation with the binding potential introduced by Bohr and Mottelson [100], i.e.,

$$U(R) = Vf(R) + V_{ls}(\boldsymbol{l}\cdot\boldsymbol{s})r_0^2\frac{1}{R}\frac{d}{dR}f(R), \tag{7.1}$$

where

$$f(R) = \frac{1}{1+\exp\left(\frac{R-R_0}{a}\right)}. \tag{7.2}$$

The parameters are given by

$$R_0 = r_0 B^{1/3}, \tag{7.3}$$
$$r_0 = 1.27 \text{ fm}, \tag{7.4}$$
$$a = 0.67 \text{ fm}, \tag{7.5}$$
$$V = \left(-51 + 33\frac{N-Z}{A}\right) \text{ MeV}, \tag{7.6}$$
$$V_{ls} = -0.44V \tag{7.7}$$

with N, Z and B being the number of neutrons, protons, and nucleons of nucleus B, respectively. In the results in this chapter, the spectroscopic factor of the struck nucleon taken from the $(e,e'p)$ reaction analyses are adopted, instead of fitting the DWIA results to the experimental data In this way the consistency between the spectroscopic factors deduced from the two reactions is investigated because they should be independent of what kind of reactions they are deduced from. It should be noted, however, that the electron-induced knockout experiments can hardly be applied to neutron knockout reactions and also to unstable nuclei in inverse kinematics, even though the electron storage ring facility named SCRIT [129–131] at RIKEN has been under development. The spectroscopic factors of stable nuclei deduced from $(e,e'p)$ analyses are summarized in Ref. [132].

In Fig. 7.1 ^{12}C$(p,2p)^{11}$B from the $0p_{3/2}$ orbital at 392 MeV is shown as a function of the recoil momentum defined by

$$p_R = \hbar K_{\rm B}^{\rm L}\frac{K_{{\rm B}z}^{\rm L}}{|K_{{\rm B}z}^{\rm L}|}. \tag{7.8}$$

The experimental data are taken from Ref. [133, 134]. The kinematics of particle 1 are fixed to be $T_1^{\rm L} = 250$ MeV and $\theta_1^{\rm L} = 32.5°$. $T_2^{\rm L}$ and $\theta_2^{\rm L}$ vary with satisfying the energy and momentum conservations. The reaction is kept in coplanar; $\phi_1^{\rm L} = 0$ and $\phi_2^{\rm L} = \pi$. Since TDX is essentially the squared Fourier transform of the s.p. wave function as discussed in Sec. 2.1.5, a typical behavior of the recoil momentum distribution with $l = 1$ is clearly seen; no TDX is obtained at the recoilless condition ($p_R = 0$ MeV/c) since the angular momentum is finite. Both the shape and the magnitude of the recoil momentum distribution are well reproduced by DWIA calculation employing the proton spectroscopic factor of 1.72 from the $(e,e'p)$ analysis [135]. It should be noted that the deeper dip around $p_R \sim 0$ of the DWIA result is known to be almost eliminated by including the finite size of the detection region in the experiment.

In Fig. 7.2, the so-called energy sharing distribution, the TDX of the ^{16}O$(p,2p)^{15}$N* (6.32 MeV) as a function of T_1, is shown. In this reaction the proton is considered to be knocked out from the $0p_{3/2}$ orbital and consequently the residue is in an excited state. The kinematics are fixed to $\theta_1^{\rm L} = \theta_2^{\rm L} = 47°$ in Fig. 7.2(a), and $\theta_1^{\rm L} = 69°$ and $\theta_2^{\rm L} = 35°$ in Fig. 7.2(b). $T_1^{\rm L}$ and $T_1^{\rm L}$ vary with satisfying the energy and momentum conservations.

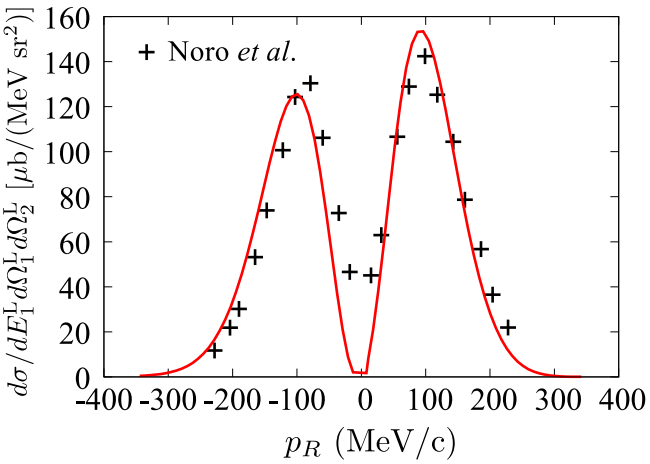

FIGURE 7.1: Recoil momentum distribution of the ^{12}C(p,2p)^{11}B at 392 MeV. The proton is knocked out from the $0p_{3/2}$ orbital. The experimental data are taken from Ref. [133, 134].

It is the reason why this kinematics are called "energy sharing distribution". The experimental data are taken from Ref. [44] and the proton spectroscopic factor of 2.25 deduced from the (e,$e'p$) analysis [132] is adopted. Similarly in Fig. 7.3, the result of

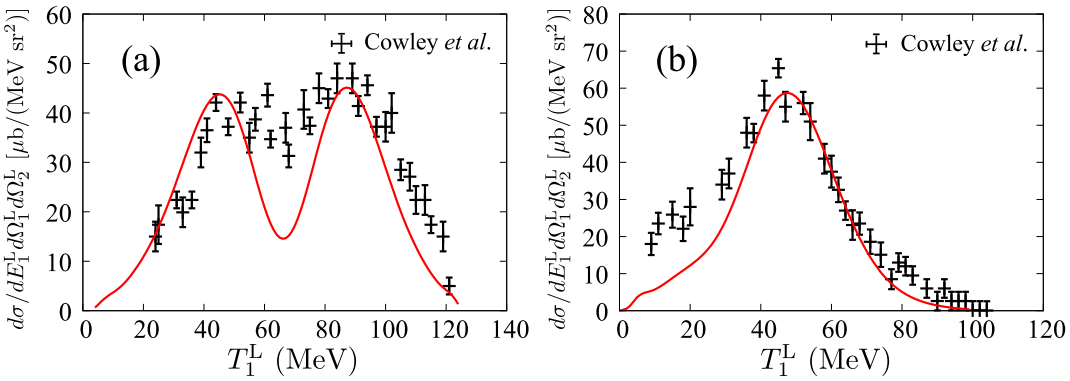

FIGURE 7.2: (a) Energy sharing distribution of the ^{16}O(p,2p)^{15}N* (6.32 MeV) at 151 MeV incident energy. The proton is knocked out from the $0p_{3/2}$ orbital. The kinematics are fixed to $\theta_1^L = \theta_2^L = 47°$. The experimental data are taken from Ref. [44]. (b) Same as (a) but with $\theta_1^L = 69°$ and $\theta_2^L = 35°$.

the ^{40}Ca(p,2p)^{39}K* (2.52 MeV) is shown. The proton is knocked out from the $1s_{1/2}$ orbital. The kinematics are fixed to $\theta_1^L = \theta_2^L = 41°$ in Fig. 7.3(a), and $\theta_1^L = 30°$, $\theta_2^L = 49°$ in Fig. 7.3(b). The experimental data are taken from Ref. [42], and the spectroscopic factor of 1.03 deduced from the (e,$e'p$) analysis [132] is adopted. As is the case with ^{12}C(p,2p)^{11}B, both the shape and the magnitude of the ^{16}O(p,2p)^{15}N* and ^{40}Ca(p,2p)^{39}K* are well explained.

7.3 Spectroscopic factors of unstable nuclei

Although consistent spectroscopic factors are obtained from the (p,2p) and (e,$e'p$) analyses as shown in Sec. 7.2, it has been reported in Refs. [136, 137] that the nucleon spectroscopic factors deduced from inclusive nucleon removal experiments and their analyses show a systematic inconsistency with those predicted by the shell model

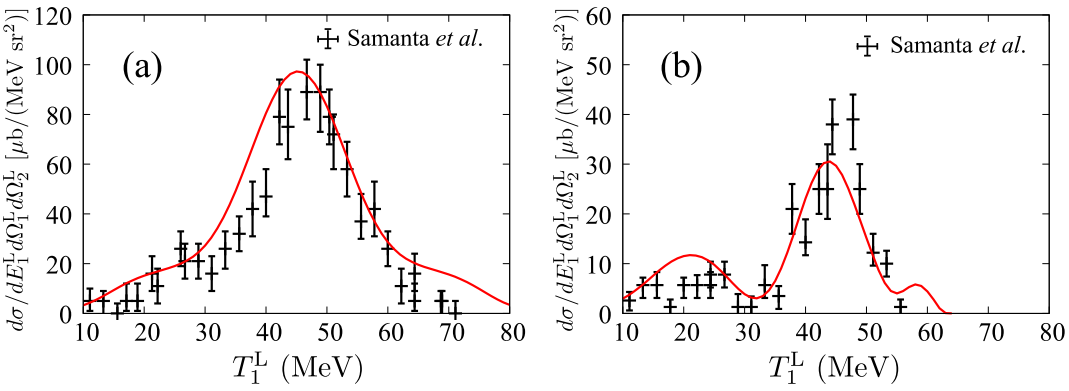

FIGURE 7.3: (a) Energy sharing distribution of the ^{40}Ca(p,2p)^{39}K* (2.52 MeV) at 101 MeV and 76 MeV. The proton is knocked out from the $1s_{1/2}$ orbital. The kinematics is fixed to $T_0 = 101$ MeV and $\theta_1^L = \theta_2^L = 41°$. The experimental data are taken from Ref. [42]. (b) Same as (a) but with $T_0 = 76$ MeV, $\theta_1^L = 30°$, and $\theta_2^L = 49°$.

calculations. In Fig. 7.4 the so-called reduction factor, R_s, is shown as a function of the difference between the neutron and proton separation energies ΔS. Figure 7.4 is

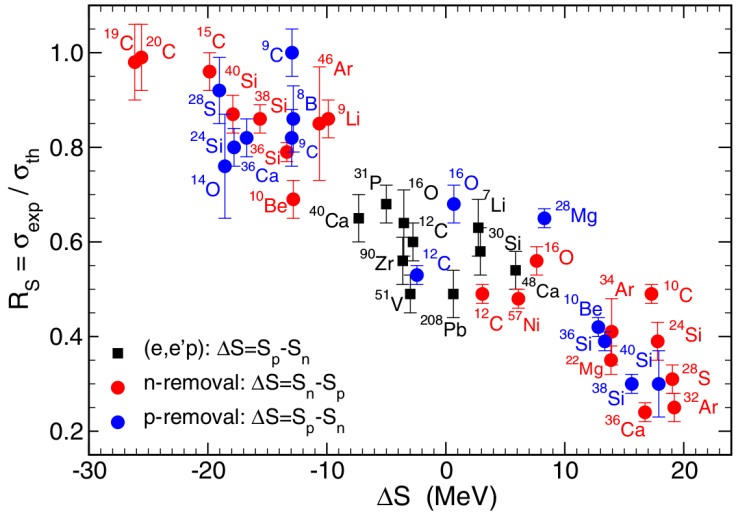

FIGURE 7.4: Reduction factor R_s as a function of ΔS. The red (blue) points are for neutron (proton) removal. The solid (black) squares are from (e,$e'p$) analyses. The figure is taken from Fig. 1 of Ref. [137].

taken from Fig. 1 of Ref. [137]. ΔS is defined by $\Delta S = S_n - S_p$ ($\Delta S = S_p - S_n$) for neutron (proton) removal reactions where S_n (S_p) is the neutron (proton) separation energy. The reduction factor R_s is defined by

$$R_s = \frac{\sigma_{\rm exp}}{\sigma_{\rm th}}, \tag{7.9}$$

where $\sigma_{\rm exp}$ is the observed experimental cross section and $\sigma_{\rm th}$ is the theoretical cross section including the shell model spectroscopic factor.

As shown in fig. 7.4, when ΔS is small, which corresponds to the loosely bound nucleon removal reactions, $R_s \sim 1$ and the consistent spectroscopic factors are obtained from both the experiment analyses and the shell model calculations. On the

other hand when ΔS is large, which corresponds to the nucleon removal from deep orbitals, $R_s \sim 0.2$ in the worst cases.

It should be noted, however, that the inclusive nucleon removal reactions can be considered to be unclearer method than the exclusive nucleon knockout reactions. In this point of view, proton knockout reactions from O isotopes covering a wide range of ΔS has been recently performed [138]. In Fig. 7.5, the reduction factors for $^{14-24}$O are shown. This figure is taken from Fig. 6 of Ref. [138]. The up (down) pointing

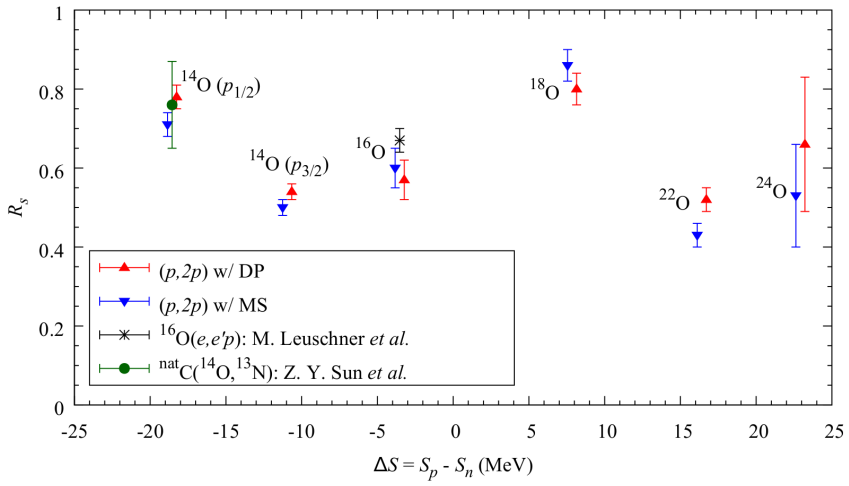

FIGURE 7.5: Reduction factors for $^{14-24}$O as a function of ΔS. The up (down) pointing triangles are R_s deduced from the DWIA analyses using DP and MS. R_s obtained by the $(e, e'p)$ reaction [139] and the proton removal ^{nat}C(^{14}O,^{13}N) reaction [140] are shown for the comparison. The figure is taken from Fig. 6 of Ref. [138].

triangles are R_s deduced from the DWIA analyses by the THREEDEE code [38] using the Dirac phenomenology optical potential (DP) [76, 77] and the microscopic optical potential (MS) [69] with the Melbourne g-matrix [63].

The different systematics from Fig. 7.4 are found in Fig. 7.5. The reduction factors are roughly constant for the wide range of ΔS, lying $0.5 \lesssim R_s \lesssim 0.9$, which gives consistent results with that of the $(e,e'p)$ analysis. Nevertheless, R_s from the knockout reaction analyses still deviates from unity. This is because the spectroscopic factors predicted by the shell model calculations are larger than ones obtained experimentally. This may suggest there exist missing correlations of nucleons in the shell model. From Figs. 7.4 and 7.5, it may be concluded that the systematic behavior of R_s deduced from nucleon removal reactions shown in Fig. 7.4 will be originated from the reaction analysis for the removal reactions. The systematics seen in Fig. 7.4 cannot be found in the nucleon knockout analyses, as shown in Fig. 7.5. These results show that it is important to apply a clean reaction to the nucleon spectroscopic studies and the exclusive nucleon knockout reactions will be a good probe for the s.p. states. The inconsistency between the spectroscopic factors predicted by the shell model and those deduced from the knockout reaction analyses have not yet solved and further investigations are needed.

7.4 Density dependence of NN interaction on vector analyzing power

In this section, the in-medium effect of the nucleon-nucleon (NN) interaction on the vector analyzing power (A_y) of the ^{16}O(p,2p)^{15}N reaction is discussed. The vector analyzing power and the so-called Maris effect are introduced in Appendix F. As for the NN effective interaction, a g-matrix interaction based on the chiral interactions [141, 142] is employed. Note that in the present study the density dependence and the off-the-energy-shell property of the NN interaction is taken into account properly, but only the two-nucleon force is considered.

In Fig. 7.6, the vector analyzing power of the ^{16}O(p,2p)^{15}N at 200 MeV are shown. The kinematics are chosen to be the symmetric opening angles; $\theta_1 = \theta_2 = 30°$, 40°, and 47° in Fig. 7.6(a), (b), and (c), respectively. The azimuthal angles of emitted particle 1 and 2 are fixed at 0 and π, respectively, i.e., the scattered particles are in a coplanar. The bound state wave function is obtained by the Woods-Saxon shaped binding potential;

$$V(R) = -V_c f(R) + V_{so}\left(\frac{\hbar}{m_\pi c}\right)^2 \frac{1}{R}\frac{df}{dR}(\boldsymbol{l}\cdot\boldsymbol{\sigma}), \tag{7.10}$$

$$f(R) = \frac{1}{1+\exp\left(\frac{R-R_0}{a}\right)}. \tag{7.11}$$

$V_c = 52$ MeV, $V_{so} = 13$ MeV, $R_0 = 1.41 \times 15^{1/3}$ fm, and $a = 0.65$ fm are the depth of the central potential,that of spin-orbit potential, range and diffuseness parameter taken from Ref [143], respectively. The global optical potential by Koning and Delaroche [78] is adopted for incoming and outgoing protons. The solid, dashed, and dotted lines are the proton knockout reaction from $0p_{3/2}$ orbital with employing pp effective interaction at the matter density $\rho = 0$ fm^{-3}, 0.035 fm^{-3}, and 0.166 fm^{-3} (normal density), respectively. The dot-dashed, two-dot-dashed, and three-dot-dashed lines are the same as above but the proton knockout reaction from $0p_{1/2}$ orbital. As shown in Fig. 7.6, the Maris effect is well reproduced in case (a) particular, without adjusting any input. This effective polarization is dependent on the j-value of the struck nucleon and hence a useful method to pin down the j-values in the spectroscopic study of nuclei.

It is found that the density dependence of the NN interaction has little effect on the A_y, although ρ =0–0.166 fm^{-3} (free space to the normal density) has been investigated.

7.5 Summary

In this chapter the features of the proton induced nucleon knockout reaction and the current status of the knockout reaction studies are overviewed. The spectroscopic factors deduced from the knockout reaction analyses agree well with those from electron induced nucleon knockout reactions. A strange systematics of the reduction factors deduced from the inclusive nucleon removal reactions have been resolved by the exclusive nucleon knockout analyses. Nevertheless, the reduction factors obtained by the nucleon knockout reactions deviate from unity. This may suggest that some correlations between nucleons are missing in the present shell model calculations.

Besides the knockout cross sections, the vector analyzing power is one of the key quantities of the knockout reactions. The so-called Maris effect shows clear j

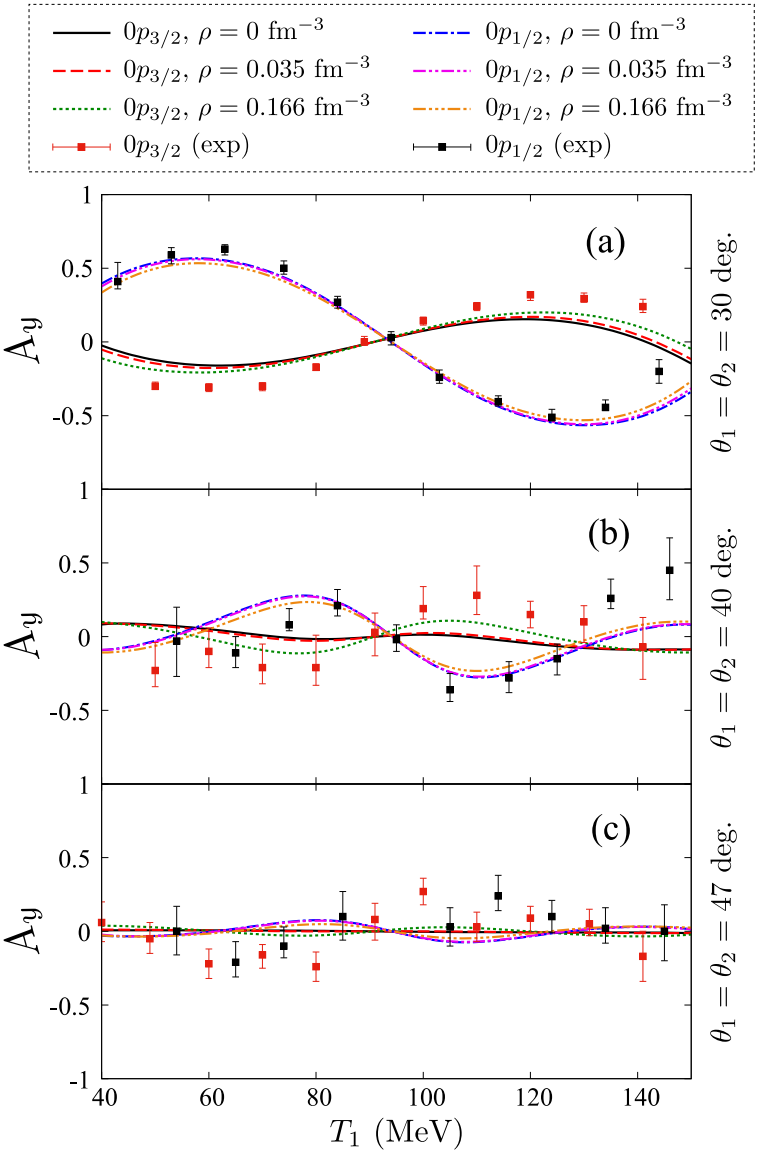

FIGURE 7.6: Vector analyzing power and the Maris effect of ^{16}O(p,2p)^{15}N$^{(*)}$ reaction at 200 MeV. The experimental data are taken from Ref. [39]. The solid, dashed, and dotted lines are the proton knockout reaction from $0p_{3/2}$ orbital with employing pp effective interaction at zero, finite, and normal density, respectively. The dot-dashed, two-dot-dashed, and three-dot-dashed lines are the same as above but the proton knockout reaction from $0p_{1/2}$ orbital. See the text for the detail.

dependence in the energy sharing distribution and one may pin down the j value of the knocked out nucleon. The effect of the density dependence of nucleon-nucleon effective interaction on the vector analyzing power is also investigated, and it has been shown that the effect is little.

Chapter 8

Summary and conclusion

In this thesis the proton (p) induced nucleon (N) or α knockout reactions, i.e., (p,pN) and (p,$p\alpha$) reactions have been studied. It has been shown that the nucleon (α) knockout reaction is a good probe for the single particle (α cluster) state of nuclei.

In Chap. 2, the distorted wave impulse approximation (DWIA) formalism is given. Various approximations in the DWIA formalism is also introduced in detail. The validity of the DWIA framework and the approximations adopted to that is discussed in the following chapters. The helicity formalism for DWIA is also introduced.

In Chap. 3, The longitudinal and transverse momentum distributions (LMD and TMD) of the ^{15}C(p,pn)^{14}C at 420 MeV/u is investigated with three different theories, i.e., DWIA, the transfer-to-the-continuum model (TC) and the Faddeev-AGS method (FAGS). The LMDs calculated with DWIA excluding the energy dependence of the distorting potentials (EI-DWIA) and TC are found to give good agreements in both shape and magnitude. Obtained LMDs of EI-DWIA and TC agree with each other for various neutron separation energies S_n, giving only 0.3 %, 0.8 % and 1.4 % differences at the peak of LMDs for S_n = 1.22 MeV, 5 MeV and 18 MeV, respectively. The effects coming from the energy dependence of optical potentials, which are not taken into account in the TC and the FAGS framework, is also tested by comparing the results between the EI-DWIA and the DWIA including the energy dependence of the distorting potentials (ED-DWIA). It has been shown that the inclusion of the energy dependence of the optical potentials decreases the momentum distribution by 8.0 %, 9.3 % and 4.9 % for S_n = 1.22 MeV, 5 MeV and 18 MeV, respectively. The difference is not severe but will be important for quantitative discussions, when deducing spectroscopic factors from knockout cross sections in particular. On the other hand, the relativistic treatment on kinematics increases the cross section by about 30 % and it is shown to be essential.

In Chap. 4, the ^{120}Sn(p,$p\alpha$)^{116}Cd has been investigated. The validity of the so-called factorization approximation is confirmed. It should be noted that the asymptotic momentum approximation (AMA) itself does not work well in this reaction. However, thanks to the strong absorption in the region where AMA does not work, the knockout cross sections are not affected by the failure of AMA. The strong absorption makes the reaction very peripheral. Therefore the α clustering on the surface of nuclei can be probed clearly. Furthermore, it was shown that the reaction has high selectivity on also the direction of the target nucleus; the α cluster wave function in only the fore-side region with respect to the emitted α is probed.

In Chap. 5, the ^{20}Ne(p,$p\alpha$)^{16}O reaction at 100–392 MeV was investigated. A new concept, *the masking function*, which shows how the α cluster wave functions are probed through the knockout reactions, is introduced. Through the analyses on the masking function, it is clearly shown that the (p,$p\alpha$) is enough peripheral for probing the α cluster amplitude in the nuclear surface, and the (p,$p\alpha$) reaction can be a direct measure of spatially developed α cluster states. By adopting the eikonal

approximation to the masking function, one can reproduce the masking function in a simplified way with one free parameter. This parameter shows the total effective absorption strength and related to the mean free path of the knockout reaction. The incident energy dependence of the parameter was investigated and shown to be weak above 200–400 MeV, where the quasi-free (impulse) knockout reaction picture is valid. On the other hand, below 200 MeV it increases rather rapidly as the incident energy decreases, due to the small mean free paths of low energy particles, especially α. As a case of strong Coulomb interaction, the ^{120}Sn(p,$p\alpha$)^{116}Cd reaction has been also investigated in this chapter. It has been shown that, although the eikonal masking function fails to reproduce the proper asymptotic behavior owing to the long-range nature of Coulomb interactions, the radial distribution of reaction amplitude is reproduced well. This is because the eikonal masking function agrees with the true masking function in the nuclear interior, where the cluster amplitude exists.

In Chap. 6, the ^{10}Be(p,$p\alpha$)^{6}He have been investigated. The ^{10}Be and ^{6}He wave functions are described by the Tohsaki-Horiuchi-Schuck-Röpke (THSR) wave function. Adopting the α cluster wave function obtained by THSR wave functions to the DWIA framework, it is shown that the α cluster wave function at the nuclear surface is probed through the ^{10}Be(p,$p\alpha$)^{6}He reaction. Hence, the α knockout cross section can be a direct measure of the spatially developed α cluster states. Furthermore, benefiting the flexibility of THSR wave function, the α knockout reactions from the shell-like and gas-like structures of ^{10}Be has been investigated. It has been shown that the knockout cross section has very high sensitivity to the size of ^{10}Be and one can safely pin down the α-α distance from the α knockout cross sections.

In Chap. 7, the features of the (p,pN) reactions and the current status of the knockout reaction studies are given. The spectroscopic factors deduced from the knockout reaction analyses were shown to agree well with those from (e,$e'p$) reactions. A strange systematics of the so-called reduction factors deduced from the inclusive nucleon removal reactions have been resolved by the exclusive nucleon knockout analyses. On the other hand, the reduction factors obtained by (p,pN) analyses deviate from unity. This suggests that there exist missing correlations of nucleons. The vector analyzing power is one of the key quantities of the knockout reactions. The so-called Maris effect is discussed and the clear j dependence in the energy sharing distribution is shown, and one may pin down the j value of the knocked out nucleon. The effect of the density dependence of nucleon-nucleon (NN) effective interaction on the vector analyzing power (A_y) is also investigated, and it has been shown that the effect is little.

Appendix A

Gell-Mann-Goldberger transformation

Here the Hamiltonian of the total system is defined by,

$$H = T_{c_1} + V_{c_1} + h_{c_1} = T_{c_2} + V_{c_2} + h_{c_2} = \cdots , \tag{A.1}$$

where T_j, V_j, h_j are the kinetic operator, interaction, and internal Hamiltonian of the nuclei in the channel j.

The post form transition matrix from channel i to j is given by,

$$T_{fi} = \left\langle \phi_f \middle| V_f \middle| \Psi_i^{(+)} \right\rangle \tag{A.2}$$

The superscript $(+)$ or $(-)$ denotes the outgoing or incoming boundary condition, respectively.

The goal of this discussion is to show the transformation,

$$T_{fi} = \left\langle \phi_f \middle| U_f \middle| \chi_i^{(+)} \right\rangle \delta_{fi} + \left\langle \chi_f^{(-)} \middle| V_f - U_f \middle| \Psi_i^{(+)} \right\rangle , \tag{A.3}$$

where U_j is an auxiliary interaction, whose property is well known, for example, an optical potential which is constructed to give a proper (asymptotic) behavior of scattering wave function corresponding to the elastic scattering. ϕ_j (χ_j) is the plane wave (distorted wave) function which the solution of the Schrödinger equation:

$$[E - T_j - h_j]\, \phi_j = 0, \tag{A.4}$$

$$[E - T_j - U_j - h_j]\, \chi_j = 0. \tag{A.5}$$

It should be noted that Ψ_j, χ_j and ϕ_j include the internal eigenstate corresponding to internal Hamiltonian h_j in this discussion. Therefore there is no need to specify the channel of E.

As a first step to show Eq. (A.3), the Lippmann-Schwinger equation is adopted to the Schrödinger equation:

$$[E - T_i - V_i - h_i]\, \Psi_j = 0, \tag{A.6}$$

that leads,

$$\Psi_i^{(+)} = \phi_i + \frac{1}{E - T_i - h_i + i\eta} V_i \Psi_i^{(+)}. \tag{A.7}$$

This iteration can be summed up as,

$$\Psi_i^{(+)} = \phi_i + \frac{1}{E - H + i\eta} V_i \phi_i. \tag{A.8}$$

Applying the Gell-Mann-Goldberger identity:

$$\frac{1}{a-b} = \frac{1}{a}\left(1 + b\frac{1}{a-b}\right) = \left(1 + \frac{1}{a-b}b\right)\frac{1}{a}, \tag{A.9}$$

to the second term of Eq. (A.8), one obtains,

$$\begin{aligned}
\Psi_i^{(+)} &= \left(1 + \frac{1}{E - H + i\eta}\left(V_i - U_i + U_i\right)\right)\phi_i \\
&= \left[\left(1 + \frac{1}{E - H + i\eta}(V_i - U_i)\right) + \frac{1}{E - T_i - U_i - h_i + i\eta - (V_i - U_i)} U_c\right]\phi_i \\
&= \left[\left(1 + \frac{1}{E - H + i\eta}(V_i - U_i)\right)\right. \\
&\quad \left. + \left(1 + \frac{1}{E - H + i\eta}(V_i - U_i)\right)\frac{1}{E - T_i - U_i - h_i + i\eta} U_i\right]\phi_c \\
&= \left(1 + \frac{1}{E - H + i\eta}(V_i - U_i)\right)\left(1 + \frac{1}{E - T_i - U_i - h_i + i\eta} U_i\right)\phi_i.
\end{aligned} \tag{A.10}$$

Since the formal solution of Eq. (A.5) is given by

$$\chi_i^{(+)} = \left(1 + \frac{1}{E - T_i - U_i - h_i + i\eta} U_i\right)\phi_i, \tag{A.11}$$

The total wave function is reduced to

$$\Psi_i^{(+)} = \left(1 + \frac{1}{E - H + i\eta}(V_i - U_i)\right)\chi_i^{(+)}. \tag{A.12}$$

Operating $(E - H + i\eta)$ from left,

$$\begin{aligned}
(E - H + i\eta)\Psi_i^{(+)} &= (E - H + i\eta + (V_i - U_i))\,\chi_i^{(+)}, \\
&= (E - T_i - U_i - h_i + i\eta)\,\chi_i^{(+)}, \\
&= i\eta\chi_i^{(+)},
\end{aligned} \tag{A.13}$$

and another operator of the final channel $(E - T_f - U_f - h_f + i\eta)$ from left,

$$\frac{1}{E - T_f - U_f - h_f + i\eta}(E - H + i\eta)\Psi_i^{(+)} = \frac{1}{E - T_f - U_f - h_f + i\eta} i\eta\chi_i^{(+)}, \tag{A.14}$$

$$\Psi_i^{(+)} = \frac{i\eta}{E - T_f - U_f - h_f + i\eta}\chi_i^{(+)} + \frac{1}{E - T_f - U_f - h_f + i\eta}(V_f - U_f)\Psi_i^{(+)}. \tag{A.15}$$

The first term vanishes unless $i = f$ when $\eta \to 0$ [144] because,

$$\frac{1}{E - T_f - U_f - h_f + i\eta}(E - T_i - U_i - h_i + i\eta)\chi_i^{(+)} = \chi_i^{(+)} \quad (i = f), \tag{A.16}$$

and also,

$$\begin{aligned}&\frac{1}{E-T_f-U_f-h_f+i\eta}(E-T_i-U_i-h_i+i\eta)\chi_i^{(+)}\\&\quad=\frac{i\eta}{E-T_f-U_f-h_f+i\eta}\chi_i^{(+)}\xrightarrow[\eta\to 0]{}0\quad(i\neq f),\end{aligned}\tag{A.17}$$

and that leads

$$\Psi_i^{(+)}=\chi_i\delta_{fi}+\frac{1}{E-T_f-U_f-h_f+i\eta}(V_f-U_f)\Psi_i^{(+)},\tag{A.18}$$

$$\to V_f\Psi_i=(U_f+V_f-U_f)\Psi_i\tag{A.19}$$

$$=U_f\left(\chi_i^{(+)}\delta_{fi}+\frac{1}{E-T_f-U_f-h_f+i\eta}(V_f-U_f)\Psi_i^{(+)}\right)+(V_f-U_f)\Psi_i^{(+)}\tag{A.20}$$

$$=U_f\chi_i^{(+)}\delta_{fi}+\left(1+U_f\frac{1}{E-T_f-U_f-h_f+i\eta}\right)(V_f-U_f)\Psi_i^{(+)}.\tag{A.21}$$

Finally, the transition matrix is given by

$$T_{fi}=\left\langle\phi_f\middle|V_f\middle|\Psi_i^{(+)}\right\rangle\tag{A.22}$$

$$=\left\langle\phi_f\middle|U_f\middle|\chi_i^{(+)}\right\rangle\delta_{fi}+\left\langle\phi_f\middle|\left(1+U_f\frac{1}{E-T_f-U_f-h_f+i\eta}\right)(V_f-U_f)\middle|\Psi_i^{(+)}\right\rangle\tag{A.23}$$

$$=\left\langle\phi_f\middle|U_f\middle|\chi_i^{(+)}\right\rangle\delta_{fi}+\left\langle\left(1+U_f\frac{1}{E-T_f-U_f-h_f+i\eta}\right)^{\dagger}\phi_f\middle|(V_f-U_f)\middle|\Psi_i^{(+)}\right\rangle\tag{A.24}$$

$$=\left\langle\phi_f\middle|U_f\middle|\chi_i^{(+)}\right\rangle\delta_{fi}+\left\langle\chi_f^{(-)}\middle|(V_f-U_f)\middle|\Psi_i^{(+)}\right\rangle.\tag{A.25}$$

Comparing Eq. (A.25) with Eq. (A.3), especially if $i\neq f$, U_f is consumed to distort the final state ϕ_f. This is called Gell-Mann-Goldberger transformation.

Appendix B

Wigner's D-matrix

Details on Wigner's D-matrix is given in Ref. [65, 145]. The Wigner-D matrix $D^J_{MM'}(R)$ may be defined as the matrix elements of the rotation operator $\hat{R}(R)$ from an projection axis to another in the JM representation,

$$\left\langle JM \left| \hat{R}(R) \right| J'M' \right\rangle = \delta_{JJ'} D^J_{MM'}(R). \tag{B.1}$$

R denotes the rotation from Ω to Ω'. The D-matrices realize transformations of covariant components of any irreducible tensor of rank J under coordinate rotations,

$$\Psi_{JM'}(\Omega', \sigma') = \sum_{M=-J}^{J} \Psi_{JM}(\Omega, \sigma) D^J_{MM'}(R), \tag{B.2}$$

$$\Psi^*_{JM'}(\Omega', \sigma') = \sum_{M=-J}^{J} \Psi^*_{JM}(\Omega, \sigma) D^{J*}_{MM'}(R). \tag{B.3}$$

σ and σ' are spin variables in the initial and new systems.

The sentences below, taken from Ref. [145], will be important.

> States with a given angular momentum relative to one frame have the same angular momentum relative to any other rotated frame. It will be noted that this statement is not generally true for a component of an angular momentum like l_z. A state with a definite value of z-projection of l in one frame does not generally represent a definite z-projection of the angular momentum in another frame.

The equations above show that $\Psi_{JM'}(\Omega', \sigma')$ is described by the superposition of $\Psi_{JM}(\Omega, \sigma)$ with several different values of M. The coefficients $D^J_{MM'}(R)$ is the Wigner-D matrix or D function. The rotation R can be described by Euler-angles (α, β, γ) for example. Here the z-y-z convention is assumed. The general form of $D^l_{mk}(\alpha, \beta, \gamma)$ is given by,

$$D^l_{mk}(\alpha, \beta, \gamma) = e^{-im\alpha} d^l_{mk}(\beta) e^{-ik\gamma} \tag{B.4}$$

$$d^l_{mk} = \sum_{\sigma} \sqrt{\frac{(l+k)!(l-k)!(l+m)!(l-m)!}{(l-k-\sigma)!(l-m-\sigma)!\sigma!(m+k+\sigma)!}} \times (-)^{l-k-\sigma} \left(\cos\frac{\beta}{2}\right)^{2\sigma+m+k} \left(\sin\frac{\beta}{2}\right)^{2l-(2\sigma+m+k)}. \tag{B.5}$$

The summation over σ runs $max(0, -m-k) \leq \sigma \leq min(l-k, l-m)$.

$$d^l_{mk}(\beta) = d^l_{km}(-\beta) \tag{B.6}$$

$$d^l_{mk}(\beta) = (-)^{m-k} d^l_{km}(\beta) = (-)^{m-k} d^l_{-m-k}(\beta) = d^l_{-k-m}(\beta) \tag{B.7}$$

$$d^l_{mk}(\pi-\beta) = (-)^{l-k} d^l_{-mk}(\beta) = (-)^{l+m} d^l_{m-k}(\beta). \tag{B.8}$$

$d^l_{mk}(\beta)$ for $l = 1/2, 1$ are

$$d^{1/2}_{mk}(\beta) = \begin{array}{c|cc} m \backslash k & \text{-1/2} & 1/2 \\ \hline -1/2 & \cos\frac{\beta}{2} & \sin\frac{\beta}{2} \\ 1/2 & -\sin\frac{\beta}{2} & \cos\frac{\beta}{2} \end{array}$$

$$d^1_{mk}(\beta) = \begin{array}{c|ccc} m \backslash k & \text{-1} & 0 & 1 \\ \hline -1 & \cos^2\frac{\beta}{2} & \frac{1}{\sqrt{2}}\sin\beta & \sin^2\frac{\beta}{2} \\ 0 & -\frac{1}{\sqrt{2}}\sin\beta & \cos\beta & \frac{1}{\sqrt{2}}\sin\beta \\ 1 & \sin^2\frac{\beta}{2} & -\frac{1}{\sqrt{2}}\sin\beta & \cos^2\frac{\beta}{2} \end{array}$$

Orthogonal relationships are

$$\sum_k D^{l*}_{mk}(\Omega) D^l_{m'k}(\Omega) = \delta_{mm'} \tag{B.9}$$

$$\sum_m D^{l*}_{mk}(\Omega) D^l_{mk'}(\Omega) = \delta_{kk'} \tag{B.10}$$

$$\frac{2l+1}{8\pi^2} \int d\Omega\, D^{l*}_{mk}(\Omega) D^{l'}_{m'k'}(\Omega) = \delta_{ll'}\delta_{mm'}\delta_{kk'}$$

$$\left(\int d\Omega = \int_0^{2\pi} d\alpha \int_0^{\pi} d\beta \sin\beta \int_0^{2\pi} d\gamma \right). \tag{B.11}$$

The product of two D-matrices with the same arguments Ω may be expanded in the following series

$$D^{J_1}_{M_1N_1}(\Omega) D^{J_2}_{M_2N_2}(\Omega) = \sum_{J=|J_1-J_2|}^{J_1+J_2} \sum_{MN} (J_1M_1J_2M_2|JM)(J_1N_1J_2N_2|JN) D^J_{MN}(\Omega). \tag{B.12}$$

Using this expansion, together with the orthogonality condition of the Clebsch-Gordan coefficients,

$$\sum_{m_1m_2} (j_1m_1j_2m_2|jm)(j_1m_1j_2m_2|j'm') = \delta_{jj'}\delta_{mm'}, \tag{B.13}$$

$$\sum_{j(m)} (j_1m_1j_2m_2|jm)(j_1m'_1j_2m'_2|jm) = \delta_{m_1m'_1}\delta_{m_2m'_2}, \tag{B.14}$$

one can calculate sums of products of D-matrices with identical arguments as follows.

$$\sum_{M_1M_2N_1N_2} (J_1M_1J_2M_2|JM)(J_1N_1J_2N_2|J'N) D^{J_1}_{M_1N_1}(\Omega) D^{J_2}_{M_2N_2}(\Omega)$$

$$= \delta_{N_1N'_1} \{J_1J_2J\} D^J_{NM}(\Omega) \tag{B.15}$$

$$\sum_{J=|J_1-J_2|}^{J_1+J_2}\sum_{M_1M}(J_1M_1J_2M_2|JM)(J_1N_1'J_2N_2|JN)D^{*J_1}_{M_1N_1}(\Omega)D^{J}_{MN}(\Omega)$$
$$=\delta_{N_1N_1'}D^{J_2}_{M_2N_2}(\Omega) \quad \text{(B.16)}$$

$$\sum_{N_1N_2}(J_1N_1J_2N_2|JN)D^{J_1}_{M_1N_1}(\Omega)D^{J_2}_{M_2N_2}(\Omega)=(J_1M_1J_2M_2|JM)D^{J}_{MN}(\Omega) \quad \text{(B.17)}$$

$$\sum_{N_1N_2N}(J_1N_1J_2N_2|JN)D^{*J}_{MN}(\Omega)D^{J_1}_{M_1N_1}(\Omega)D^{J_2}_{M_2N_2}(\Omega)=(J_1M_1J_2M_2|JM) \quad \text{(B.18)}$$

$$\sum_{M_1M_2MN_1N_2}(J_1M_1J_2M_2|JM)(J_1N_1J_2N_2|J'N')D^{*J}_{MN}(\Omega)D^{J_1}_{M_1N_1}(\Omega)D^{J_2}_{M_2N_2}(\Omega)$$
$$=\delta_{JJ'}\delta_{NN'}\{J_1J_2J\} \quad \text{(B.19)}$$

where

$$\{j_1j_2j_3\}=\begin{cases}1 & \text{if } j_1+j_2+j_3 \text{ is integer and } |j_1-j_2|\le j_3\le j_1+j_2\\ 0 & \text{otherwise}\end{cases}. \quad \text{(B.20)}$$

$\{j_1j_2J_3\}$ is invariant with respect to permutations of j_1, j_2, j_3.

Relation between the D-matrix and the spherical harmonics

$$Y_{lm}(\theta,\phi)=\sqrt{\frac{2l+1}{4\pi}}D^{l*}_{m0}(\phi,\theta,\chi) \quad \text{(B.21)}$$
$$=(-)^m\sqrt{\frac{2l+1}{4\pi}}D^{l}_{-m0}(\phi,\theta,\chi) \quad \text{(B.22)}$$
$$=(-)^m\sqrt{\frac{2l+1}{4\pi}}D^{l*}_{0m}(\chi,\theta,\phi) \quad \text{(B.23)}$$
$$=\sqrt{\frac{2l+1}{4\pi}}D^{l}_{0-m}(\chi,\theta,\phi) \qquad (\chi:\text{arbitrary}) \quad \text{(B.24)}$$
$$D^l_{00}(\alpha,\beta,\gamma)=d^l_{00}(\beta)=\sqrt{\frac{4\pi}{2l+1}}Y_{l0}(\beta,\alpha)=P_l(\cos\beta) \quad \text{(B.25)}$$

Appendix C

Jacobian from center-of-mass to laboratory frame

In this Appendix the Jacobian $J_{G\to L}$ which converts the TDX in the center-of-mass (G) frame to laboratory (L) frame:

$$J_{G\to L} \equiv \frac{dE_1 d\Omega_1 d\Omega_2}{dE_1^{\mathrm{L}} d\Omega_1^{\mathrm{L}} d\Omega_2^{\mathrm{L}}}, \tag{C.1}$$

is discussed.

From the relation,

$$dE_1 = d\left(\sqrt{(cP_1)^2 + (m_1c^2)^2}\right) = \frac{c^2 P_1}{E_1} dP_1 \tag{C.2}$$

$$= \frac{c^2}{P_1 E_1} P_1^2 dP_1, \tag{C.3}$$

one obtains,

$$dE_1 d\Omega_1 = \frac{c^2}{P_1 E_1} P_1^2 dP_1 d\Omega_1 \tag{C.4}$$

$$= \frac{c^2}{P_1} \frac{d\boldsymbol{P_1}}{E_1}. \tag{C.5}$$

In the same way as above,

$$dE_1^{\mathrm{L}} d\Omega_1^{\mathrm{L}} = \frac{c^2}{P_1^{\mathrm{L}}} \frac{d\boldsymbol{P_1^{\mathrm{L}}}}{E_1^{\mathrm{L}}}. \tag{C.6}$$

since $d\boldsymbol{P}_i/E_i$ is Lorentz invariant,

$$\frac{dE_1 d\Omega_1}{dE_1^{\mathrm{L}} d\Omega_1^{\mathrm{L}}} = \frac{P_1^{\mathrm{L}}}{P_1}, \tag{C.7}$$

Similar for particle 2,

$$\frac{dE_2 d\Omega_2}{dE_2^{\mathrm{L}} d\Omega_2^{\mathrm{L}}} = \frac{P_2^{\mathrm{L}}}{P_2}, \tag{C.8}$$

$$\to \frac{d\Omega_2}{d\Omega_2^{\mathrm{L}}} = \frac{P_2^{\mathrm{L}}}{P_2} \frac{dE_2^{\mathrm{L}}}{dE_2}. \tag{C.9}$$

Therefore,

$$J_{G\to L} = \frac{P_1^{\mathrm{L}} P_2^{\mathrm{L}}}{P_1 P_2} \frac{dE_2^{\mathrm{L}}}{dE_2}. \tag{C.10}$$

The Lorentz boost from E_2 to E_2^{L} is given by,

$$E_2^{\mathrm{L}} = \gamma(E_2 + \boldsymbol{\beta} \cdot c\boldsymbol{P}_2) = \gamma(E_2 + c\beta P_2 \cos\theta_2), \tag{C.11}$$

where

$$\boldsymbol{\beta} = \frac{c\boldsymbol{P}_{\mathrm{tot}}^{\mathrm{L}}}{E_{\mathrm{tot}}^{\mathrm{L}}}, \tag{C.12}$$

$$\gamma = \frac{1}{\sqrt{1-\beta^2}}, \tag{C.13}$$

with $\boldsymbol{P}_{\mathrm{tot}}^{\mathrm{L}}$ and $E_{\mathrm{tot}}^{\mathrm{L}}$ being total momentum and total energy in L frame, respectively. The direction of motion is taken to be parallel with z-axis and the zenith angle in G frame is given by θ_2. Since

$$P_2 = \frac{1}{c}\sqrt{E_2^2 - (m_2 c^2)^2}, \tag{C.14}$$

and hence,

$$\frac{dP_2}{dE_2} = \frac{1}{c^2}\frac{E_2}{P_2}, \tag{C.15}$$

which leads,

$$\frac{dE_2^{\mathrm{L}}}{dE_2} = \gamma\left(1 + \beta\frac{E_2}{cP_2}\cos\theta_2\right). \tag{C.16}$$

Inserting Eq. (C.16) to (C.10), the Jacobian is finally given by,

$$J_{G\to L} = \frac{P_1^{\mathrm{L}} P_2^{\mathrm{L}}}{P_1 P_2}\gamma\left(1 + \beta\frac{E_2}{cP_2}\cos\theta_2\right). \tag{C.17}$$

Appendix D

Transition matrix density and mean density

The triple differential cross section (TDX) of the knockout reaction is proportional to the absolute square of the transition matrix (T-matrix),

$$\sigma \equiv \frac{d\sigma}{dE_1 d\Omega_1 d\Omega_2} \propto |T|^2 . \tag{D.1}$$

The transition matrix density (TMD) discussed in the present thesis is originally introduced as a weighting function of the mean density in Refs. [146, 147]. The transition matrix density $\delta(R)$, which expresses the radial distribution of the reaction, consists of the real and imaginary part $\delta(R) = \delta_R(R) + i\delta_I(R)$.

An original definition of $\delta(R)$ is given by,

$$\delta_R(R) = \frac{1}{2\Delta R}(\sigma - \sigma_R), \tag{D.2}$$

$$\delta_I(R) = \frac{1}{2\Delta R}(\sigma - \sigma'_R), \tag{D.3}$$

where

$$\sigma_R = \left| \int_0^\infty I(R)dR - \int_R^{R+\Delta R} I(R)dR \right|^2 \tag{D.4}$$

$$\sigma'_R = \left| \int_0^\infty I(R)dR + i \int_R^{R+\Delta R} I(R)dR \right|^2 , \tag{D.5}$$

with $I(R)$ being the complex radial amplitude of the T-matrix,

$$T = \int_0^\infty I(R)dR. \tag{D.6}$$

Substituting Eq. (D.4) into Eq. (D.2) one obtains,

$$\delta_R(R) = \frac{\left| \int_0^\infty I(R)dR \right|^2 - \left| \int_0^\infty I(R)dR - \int_R^{R+\Delta R} I(R)dR \right|^2}{2\Delta R}. \tag{D.7}$$

By taking the limit $\Delta R \to 0$,

$$\delta_R(R) \xrightarrow[\Delta R\to 0]{} \frac{1}{2} I(R) \int_0^\infty I^*(R) dR + \frac{1}{2} I^*(R) \int_0^\infty I(R) dR \tag{D.8}$$

$$= \frac{I(R)}{2\int_0^\infty I(R) dR} \left| \int_0^\infty I(R) dR \right|^2 + \frac{I^*(R)}{2\int_0^\infty I^*(R) dR} \left| \int_0^\infty I(R) dR \right|^2 \tag{D.9}$$

$$= \mathrm{Re}\left[\frac{I(R)}{\int_0^\infty I(R) dR} \right] \sigma. \tag{D.10}$$

Similarly, substituting Eq. (D.5) into Eq. (D.3),

$$\delta_I(R) = \mathrm{Im}\left[\frac{I(R)}{\int_0^\infty I(R) dR} \right] \sigma. \tag{D.11}$$

Integrating $\delta(R)$ for whole region of R one obtains,

$$\int_0^\infty \delta_R(R) dR = \sigma, \tag{D.12}$$

$$\int_0^\infty \delta_I(R) dR = 0. \tag{D.13}$$

Therefore $\delta_R(R)$ can be regarded as the radial distribution of the cross section. It should be noted, as shown in Eq. (D.13), the integrated value of $\delta_I(R)$ does not contribute to the observables but $\delta_I(R)$ it self has finite distribution of R.

Another equivalent definition for $\delta(R) = \delta_R(R) + i\delta_I(R)$ can be given by,

$$\delta(R) \equiv T^* I(R). \tag{D.14}$$

This expression clearly shows the property of $\delta(R)$ as

$$\int_0^\infty \delta(R) dR = T^* \int_0^\infty I(R) dR = |T|^2 = \sigma, \tag{D.15}$$

and hence,

$$\int_0^\infty \delta_R(R) dR = \mathrm{Re}\,[\sigma] = \sigma, \tag{D.16}$$

$$\int_0^\infty \delta_I(R) dR = \mathrm{Im}\,[\sigma] = 0, \tag{D.17}$$

It can be found from Eq. (D.14) and Eq. (D.15) that T^* rotates $I(R)$ on the complex plane by $\arg(T^*) = -\arg(T)$ so as the integrated value of $\delta_I(R)$ vanishes. Therefore, although the distribution of $\delta_I(R)$ does not contribute to the observables, is magnitude and functional behavior may indicate how much interference exists.

Since the absolute values of cross sections is usually given in elsewhere and only the radial contribution to the cross sections is the interest in many cases, there are several definitions of the absolute value of the TMD; some of them are not normalized to the cross section. Therefore usually the TMD is discussed in arbitrary unit.

This method can be applied not only the radial distribution, but also the angular distribution, or both, and more. The relation between any complex function $F(x_i)$ of

a set of real variables $\{x_i\}$ and its strength

$$S = \left| \int dx_i F(x_i) \right|^2 , \tag{D.18}$$

is simply given by

$$\delta_{x_i}(x_i) = F(x_i) \int dx_i' F^*(x_i'). \tag{D.19}$$

One may integrate out any variables x_i' which are out of interest and leave those under investigation.

Appendix E

On definition of total knockout cross section

One has to be careful on the relation between total (p,pN) cross sections and total p-N cross sections, if N = p in particular. Recalling the plane-wave limit of the DWIA framework shown by Eq. (2.94), the triple differential cross section (TDX) in the center-of-mass frame is given by

$$\frac{d^3\sigma}{dE_1 d\Omega_1 d\Omega_2} = F_{\mathrm{kin}} \frac{(2\pi)^4}{\hbar v_i} \frac{(2\pi\hbar^2)^2}{\mu_{12}} \sum_{lj} \frac{1}{2l+1} S_{nlj\nu_\mathrm{b}} \frac{d\sigma_{12}}{d\Omega_{12}} (\theta_{12}, E_{12}) \times \sum_m \left| \tilde{\varphi}_{nlj\mu_j}(\boldsymbol{q}) \right|^2 . \tag{E.1}$$

For simplicity, with certain values of l and j, one may write

$$\frac{d^3\sigma}{dE_1 d\Omega_1 d\Omega_2} = C \frac{d\sigma_{12}}{d\Omega_{12}} (\theta_{12}, E_{12}) \tag{E.2}$$

where

$$C = F_{\mathrm{kin}} \frac{(2\pi)^4}{\hbar v_i} \frac{(2\pi\hbar^2)^2}{\mu_{12}} \frac{1}{2l+1} S_{nlj\nu_\mathrm{b}} \sum_m \left| \tilde{\varphi}_{nlj\mu_j}(\boldsymbol{q}) \right|^2 . \tag{E.3}$$

Since

$$d\Omega_1 d\Omega_2 = 4\pi d\Omega_{12}, \tag{E.4}$$

the TDX and the single differential cross section are reduced to

$$\frac{d^3\sigma}{dE_1 d\Omega_1 d\Omega_2} = C \frac{d\sigma_{12}}{d\Omega_{12}} (\theta_{12}, E_{12}) , \tag{E.5}$$

$$\frac{d\sigma}{dE_1} = C \int d\Omega_1 d\Omega_2 \frac{d\sigma_{12}}{d\Omega_{12}} (\theta_{12}, E_{12}) \tag{E.6}$$

$$= 4\pi C \int d\Omega_{12} \frac{d\sigma_{12}}{d\Omega_{12}} (\theta_{12}, E_{12}) . \tag{E.7}$$

Note that in practice C depends on the three-body kinematics of the (p,pN) process. E_{12}, the relative energy of p-N binary collision, may be fixed when the incident energy and E_1 is given, in a naïve quasi-free (impulse) picture.

The "problem" is, the total p-p cross section is conventionally defined by

$$\sigma_{pp}(E_{pp}) \equiv \frac{1}{2} \int d\Omega_{pp} \frac{d\sigma_{pp}}{d\Omega_{pp}} (\theta_{pp}, E_{pp}) . \tag{E.8}$$

The factor 1/2 appears because the two protons are identical particles. Note this is not a quantum mechanical effect. On the other hand, the total p-n cross section is simply defined by

$$\sigma_{pn}(E_{pn}) \equiv \int d\Omega_{pn} \frac{d\sigma_{pn}}{d\Omega_{pn}} (\theta_{pn}, E_{pn}) \,. \tag{E.9}$$

Therefore, the (p,2p) cross section is given by

$$\frac{d\sigma_{(p,2p)}}{dE_1} = \frac{1}{2} 4\pi C \sigma_{pp} (E_{pp}) \,, \tag{E.10}$$

while the (p,pn) cross section is

$$\frac{d\sigma_{(p,pn)}}{dE_1} = 4\pi C \sigma_{pn} (E_{pn}) \,. \tag{E.11}$$

Hence, the proportionality of the (p,pN) cross section to the p-N cross section is different by the factor of 2 depending on whether N = p or N = n. This difference should be kept in mind when a integrated cross section of the (p,pN) process is considered.

Appendix F

Vector analyzing power and the Maris effect

The vector analyzing power (A_y) of nucleon knockout reactions defined by Eq. (2.132), is known to be important for pinning down the total single-particle angular momentum of knocked out nucleon. Equation (2.132) is equivalently rewritten as the asymmetry of the knockout cross section:

$$A_y = \frac{\sigma^{\rm up} - \sigma^{\rm down}}{\sigma^{\rm up} + \sigma^{\rm down}}, \tag{F.1}$$

where $\sigma^{\rm up}$ ($\sigma^{\rm down}$) is the knockout cross section of the spin-up (-down) incident proton. In nucleon knockout reactions, a well known effective polarization phenomenon called the Maris effect [125–128] plays an important role in determining the total angular momentum j of the struck nucleon.

The Maris effect can be understood by the following steps.

1. Fix the kinematics of the knockout process as shown in Fig. F.1; the momentum of the emitted proton, $\boldsymbol{p}_1$, is much larger than that of knockout out nucleon, $\boldsymbol{p}_2$, with leaving the Fermi momentum of the bound nucleon $\boldsymbol{p}_{\rm N}$ being parallel with $\boldsymbol{p}_0$.

2. Consider a case that the initial proton is spin up. Since the nucleon-nucleon elastic cross section is larger when the spins of the two nucleons are parallel compared with that in the anti-parallel case, one may drop the spin anti-parallel case for qualitative understanding. In this case, both the spins of the initial proton and the struck nucleon are up.

3. Considering the direction of $\boldsymbol{p}_{\rm N}$, the direction of the orbital angular momentum $\boldsymbol{L}$ is anti-parallel (parallel) with the spin of the struck nucleon in the case A (case B) of Fig. F.1. The case A (case B) corresponds to the knockout reaction from the $\boldsymbol{j}_< = L - 1/2$ ($\boldsymbol{j}_> = L + 1/2$) single particle orbit.

4. Due to the inequality of the momenta, $p_1 \gg p_2$, the case A cannot observed as (p,pN) reaction event because the struck nucleon with small momentum p_2 may not pass through the nucleus. On the other hand, the case B is allowed because p_1 is large enough to go across the nuclear medium. The knocked out nucleon of momentum p_2 also may come out since the length of the nuclear medium for the nucleon to travel is small.

According to the discussion above, because of the imbalanced momentum sharing $p_1 \gg p_2$, the case A is forbidden and the case B is allowed; the observed events are thus dominated by the knockout process from $j_>$ orbit, and *vice versa* when initial proton is spin down. In consequence A_y for $j_>$ and $j_<$ show the opposite behavior

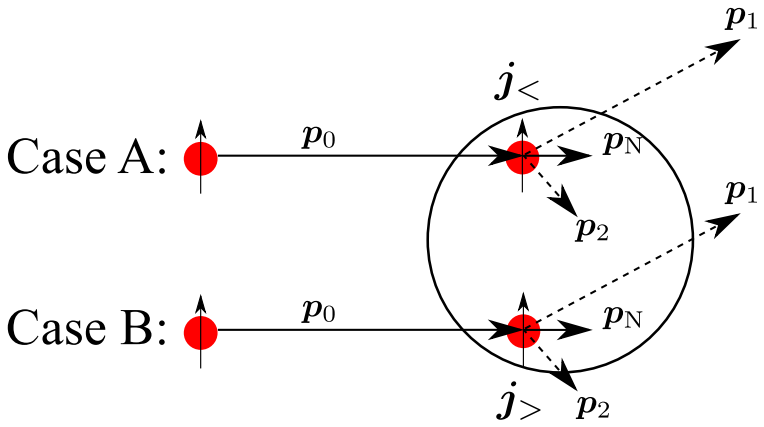

FIGURE F.1: Classical and qualitative explanation of the Maris effect. The momentum of two nucleons in the initial state, $\boldsymbol{p}_0$ and $\boldsymbol{p}_N$, are shown as the solid arrows, while those in the final state, $\boldsymbol{p}_1$ and $\boldsymbol{p}_2$, are shown as the dashed arrows. See the text for the details.

in the energy sharing distribution as shown in Fig. 7.6. This effective polarization is called the Maris effect. By decreasing p_1 and increasing p_2 with satisfying energy and momentum conservation, the effective polarization direction is gradually inverted.

It should be noted that the essence of this effective polarization is the absorption of a low momentum nucleon inside a nucleus, rather than the spin dependence of the nucleon-nucleon collision itself.

Bibliography

[1] C. F. von Weizsäcker, Zeitschrift für Physik **96**, 431 (1935).

[2] H. A. Bethe and R. F. Bacher, Rev. Mod. Phys. **8**, 82 (1936).

[3] M. G. Mayer, Phys. Rev. **74**, 235 (1948).

[4] M. G. Mayer, Phys. Rev. **75**, 1969 (1949).

[5] M. G. Mayer, Phys. Rev. **78**, 16 (1950).

[6] M. G. Mayer, Phys. Rev. **78**, 22 (1950).

[7] O. Haxel, J. H. D. Jensen, and H. E. Suess, Phys. Rev. **75**, 1766 (1949).

[8] K. Ikeda, N. Takigawa, and H. Horiuchi, Prog. Theor. Phys. Suppl. **E68**, 464 (1968).

[9] R. Tamagaki and H. Tanaka, Prog. Theor. Phys. **34**, 191 (1965).

[10] S. Typel, Phys. Rev. C **89**, 064321 (2014).

[11] A. Tohsaki, H. Horiuchi, P. Schuck, and G. Röpke, Phys. Rev. Lett. **87**, 192501 (2001).

[12] A. Ono, H. Horiuchi, T. Maruyama, and A. Ohnishi, Prog. Theor. Phys. **87**, 1185 (1992).

[13] A. Ono, H. Horiuchi, T. Maruyama, and A. Ohnishi, Phys. Rev. Lett. **68**, 2898 (1992).

[14] Y. Kanada-En'yo, H. Horiuchi, and A. Ono, Phys. Rev. C **52**, 628 (1995).

[15] Y. Kanada-En'yo and H. Horiuchi, Prog. Theor. Phys. Suppl. **142**, 205 (2001).

[16] A. Ono and H. Horiuchi, Prog. Part. Nucl. Phys. **53**, 501 (2004).

[17] Y. Kanada-En'yo, M. Kimura, and A. Ono, Prog. Theor. Exp. Phys. **2012**, 01A202 (2012).

[18] H. Feldmeier, Nucl. Phys. A **515**, 147 (1990).

[19] H. Feldmeier, K. Bieler, and J. Schnack, Nucl. Phys. A **586**, 493 (1995).

[20] H. Feldmeier and J. Schnack, Rev. Mod. Phys. **72**, 655 (2000).

[21] T. Neff and H. Feldmeier, Nucl. Phys. A **713**, 311 (2003).

[22] T. Neff and H. Feldmeier, Nucl. Phys. A **738**, Proceedings of the 8th International Conference on Clustering Aspects of Nuclear Structure and Dynamics, 357 (2004).

[23] H. Horiuchi, K. Ikeda, and K. Katō, Prog. Theor. Phys. Suppl. **192**, 1 (2012).

[24] Y. Funaki, H. Horiuchi, and A. Tohsaki, Prog. Part. Nucl. Phys. **82**, 78 (2015).

[25] M. Freer *et al.*, Rev. Mod. Phys. **90**, 035004 (2018).

[26] B. Bayman and A. Bohr, Nucl. Phys. **9**, 596 (1958).

[27] Y. Suzuki, K. Arai, Y. Ogawa, and K. Varga, Phys. Rev. C **54**, 2073 (1996).

[28] P. G. Roos *et al.*, Phys. Rev. C **15**, 69 (1977).

[29] A. Nadasen *et al.*, Phys. Rev. C **22**, 1394 (1980).

[30] T. A. Carey *et al.*, Phys. Rev. C **29**, 1273 (1984).

[31] C. W. Wang *et al.*, Phys. Rev. C **31**, 1662 (1985).

[32] A. Nadasen *et al.*, Phys. Rev. C **40**, 1130 (1989).

[33] T. Yoshimura *et al.*, Nucl. Phys. A **641**, 3 (1998).

[34] J. Mabiala *et al.*, Phys. Rev. C **79**, 054612 (2009).

[35] K. Yoshida, K. Minomo, and K. Ogata, Phys. Rev. C **94**, 044604 (2016).

[36] G. Jacob and T. A. J. Maris, Rev. Mod. Phys. **38**, 121 (1966).

[37] G. Jacob and T. A. J. Maris, Rev. Mod. Phys. **45**, 6 (1973).

[38] N. S. Chant and P. G. Roos, Phys. Rev. C **15**, 57 (1977).

[39] P. Kitching *et al.*, Nucl. Phys. A **340**, 423 (1980).

[40] N. S. Chant and P. G. Roos, Phys. Rev. C **27**, 1060 (1983).

[41] P. Kitching, W. J. McDonald, T. A. J. Maris, and C. A. Z. Vasconcellos, in Advances in nuclear physics, edited by J. W. Negele and E. Vogt (1985), pp. 43–83.

[42] C. Samanta *et al.*, Phys. Rev. C **34**, 1610 (1986).

[43] C. Samanta *et al.*, Phys. Rev. C **35**, 333 (1987).

[44] A. A. Cowley *et al.*, Phys. Rev. C **44**, 329 (1991).

[45] D. S. Carman *et al.*, Phys. Rev. C **59**, 1869 (1999).

[46] K. Ogata, K. Yoshida, and K. Minomo, Phys. Rev. C **92**, 034616 (2015).

[47] K. Minomo, M. Kohno, K. Yoshida, and K. Ogata, Phys. Rev. C **96**, 024609 (2017).

[48] R. Crespo *et al.*, Phys. Rev. C **77**, 024601 (2008).

[49] R. Crespo *et al.*, Phys. Rev. C **79**, 014609 (2009).

[50] R. Crespo, A. Deltuva, and E. Cravo, Phys. Rev. C **90**, 044606 (2014).

[51] E. Cravo, R. Crespo, and A. Deltuva, Phys. Rev. C **93**, 054612 (2016).

[52] L. D. Faddeev, Zh. Eksp. Theor. Fiz. **39**, 1459 (1960).

[53] L. D. Faddeev, Sov. Phys. JETP **12**, 1014 (1961).

[54] E. Alt, P. Grassberger, and W. Sandhas, Nucl. Phys. B **2**, 167 (1967).

[55] M. Kamimura *et al.*, Prog. Theor. Phys. Suppl. **89**, 1 (1986).

[56] N. Austern *et al.*, Physics Reports **154**, 125 (1987).

[57] M. Yahiro, K. Ogata, T. Matsumoto, and K. Minomo, Prog. Theor. Exp. Phys. **2012**, 01A206 (2012).

[58] A. M. Moro, Phys. Rev. C **92**, 044605 (2015).

[59] M. Gómez-Ramos, J. Casal, and A. Moro, Phys. Lett. B **772**, 115 (2017).

[60] T. Wakasa, K. Ogata, and T. Noro, Prog. Part. Nucl. Phys. **96**, 32 (2017).

[61] A. Kerman, H. McManus, and R. Thaler, Annals of Physics **8**, 551 (1959).

[62] M. A. Franey and W. G. Love, Phys. Rev. C **31**, 488 (1985).

[63] K. Amos *et al.*, Advances in Nuclear Physics **25**, 276 (2000).

[64] R. D. Koshel, Nucl. Phys. A **260**, 401 (1976).

[65] D. A. Varshalovich, A. N. Moskalev, and V. K. Khersonskii, *Quantum theory of angular momemtum* (World Scientific Publishing Company, 1988).

[66] Y. L. Luo and M. Kawai, Phys. Rev. C **43**, 2367 (1991).

[67] K. Ogata, G. C. Hillhouse, and B. I. S. van der Ventel, Phys. Rev. C **76**, 021602(R) (2007).

[68] Y. Watanabe *et al.*, Phys. Rev. C **59**, 2136 (1999).

[69] K. Minomo *et al.*, Journal of Physics G: Nuclear and Particle Physics **37**, 085011 (2010).

[70] M. Jacob and G. Wick, Annals of Physics **7**, 404 (1959).

[71] J. Raynal, Nucl. Phys. A **97**, 572 (1967).

[72] I. J. Thompson, Computer Physics Reports **7**, 167 (1988).

[73] K. Yoshida, M. Gómez-Ramos, K. Ogata, and A. M. Moro, Phys. Rev. C **97**, 024608 (2018).

[74] V. G. J. Stoks, R. A. M. Klomp, C. P. F. Terheggen, and J. J. de Swart, Phys. Rev. C **49**, 2950 (1994).

[75] R. V. Reid, Annals of Physics **50**, 411 (1968).

[76] S. Hama *et al.*, Phys. Rev. C **41**, 2737 (1990).

[77] E. D. Cooper, S. Hama, B. C. Clark, and R. L. Mercer, Phys. Rev. C **47**, 297 (1993).

[78] A. Koning and J. Delaroche, Nucl. Phys. A **713**, 231 (2003).

[79] R. Machleidt, Phys. Rev. C **63**, 024001 (2001).

[80] T. Yamaya *et al.*, Prog. Theor. Phys. Suppl. **132**, 73 (1998).

[81] J. Jänecke, F. Becchetti, and C. Thorn, Nucl. Phys. A **325**, 337 (1979).

[82] M. Toyokawa, K. Minomo, and M. Yahiro, Phys. Rev. C **88**, 054602 (2013).

[83] M. Yoshimura *et al.*, Phys. Rev. C **63**, 034618 (2001).

[84] S. M. Sterbenz *et al.*, Phys. Rev. C **45**, 2578 (1992).

[85] K. Egashira *et al.*, Phys. Rev. C **89**, 064611 (2014).

[86] M. Nolte, H. Machner, and J. Bojowald, Phys. Rev. C **36**, 1312 (1987).

[87] G. Grégoire, K. Grotowski, and U. catholique de Louvain (1970-). Institut Interuniversitaire des Sciences Nucléaires, *The alpha-nucleus interaction: proceedings of the 2nd louvain-cracow seminar* (Institut Interuniversitaire des Sciences Nucléaires, Université de Louvain, 1978).

[88] S. Ohkubo and Y. Hirabayashi, Phys. Rev. C **70**, 041602 (2004).

[89] T. Furumoto and Y. Sakuragi, Phys. Rev. C **74**, 034606 (2006).

[90] D. C. Cuong, D. T. Khoa, and G. Colò, Nucl. Phys. A **836**, 11 (2010).

[91] F. Perey and B. Buck, Nucl. Phys. **32**, 353 (1962).

[92] M. Igarashi, *TWOFNR user manual*, `https://people.nscl.msu.edu/~brown/reaction-codes/twofnr/twofnr.pdf`, 1977.

[93] T. Fukui *et al.*, Phys. Rev. C **93**, 034606 (2016).

[94] S. Penny and G. Satchler, Nucl. Phys. **53**, 145 (1964).

[95] P. J. Iano and N. Austern, Phys. Rev. **151**, 853 (1966).

[96] D. L. Hill and J. A. Wheeler, Phys. Rev. **89**, 1102 (1953).

[97] J. J. Griffin and J. A. Wheeler, Phys. Rev. **108**, 311 (1957).

[98] D. M. Brink, in *Proceedings of the International School of Physics "Enrico Fermi", Course 36, Varenna*, edited by C. Bloch (Academic Press, New York 1966), p. 247.

[99] K. Yoshida, K. Ogata, and Y. Kanada-En'yo, Phys. Rev. C **98**, 024614 (2018).

[100] A. Bohr and B. Mottelson, *Nuclear structure* (World Scientific Publishing, 1998).

[101] S. Okabe, Y. Abe, and H. Tanaka, Prog. Theor. Phys. **57**, 866 (1977).

[102] M. Seya, M. Kohno, and S. Nagata, Prog. Theor. Phys. **65**, 204 (1981).

[103] P. Descouvemont, Phys. Rev. C **39**, 1557 (1989).

[104] W. von Oertzen, Z. Phys. A **354**, 37 (1996).

[105] K. Arai, Y. Ogawa, Y. Suzuki, and K. Varga, Phys. Rev. C **54**, 132 (1996).

[106] A. Doté, H. Horiuchi, and Y. Kanada-En'yo, Phys. Rev. C **56**, 1844 (1997).

[107] Y. Kanada-En'yo, H. Horiuchi, and A. Doté, Phys. Rev. C **60**, 064304 (1999).

[108] Y. Ogawa, K. Arai, Y. Suzuki, and K. Varga, Nucl. Phys. A **673**, 122 (2000).

[109] N. Itagaki and S. Okabe, Phys. Rev. C **61**, 044306 (2000).

[110] P. Descouvemont, Nucl. Phys. A **699**, 463 (2002).

[111] M. Ito, K. Kato, and K. Ikeda, Phys. Lett. B **588**, 43 (2004).

[112] W. von Oertzen, M. Freer, and Y. Kanada-En'yo, Physics Reports **432**, 43 (2006).

[113] F. Kobayashi and Y. Kanada-En'yo, Phys. Rev. C **86**, 064303 (2012).

[114] M. Ito and K. Ikeda, Reports on Progress in Physics **77**, 096301 (2014).

[115] M. Lyu *et al.*, Phys. Rev. C **91**, 014313 (2015).

[116] M. Lyu *et al.*, Phys. Rev. C **93**, 054308 (2016).

[117] Y. Funaki, Phys. Rev. C **92**, 021302 (2015).

[118] Y. Funaki, Phys. Rev. C **94**, 024344 (2016).

[119] M. Lyu, K. Yoshida, Y. Kanada-En'yo, and K. Ogata, Phys. Rev. C **97**, 044612 (2018).

[120] P. Ring and P. Schuck, *The nuclear many-body problem* (Springer, 1980).

[121] Y. Kanada-En'yo, T. Suhara, and Y. Taniguchi, Prog. Theor. Exp. Phys. **2014**, 073D02 (2014).

[122] A. Volkov, Nucl. Phys. **74**, 33 (1965).

[123] N. Yamaguchi, T. Kasahara, S. Nagata, and Y. Akaishi, Prog. Theor. Phys. **62**, 1018 (1979).

[124] W. Nörtershäuser *et al.*, Phys. Rev. Lett. **102**, 062503 (2009).

[125] T. A. J. Maris, Nucl. Phys. **9**, 577 (1958).

[126] G. Jacob, T. A. Maris, C. Schneider, and M. Teodoro, Nucl. Phys. A **257**, 517 (1976).

[127] T. Maris, M. Teodoro, and C. Vasconcellos, Nucl. Phys. A **322**, 461 (1979).

[128] G. Krein, T. A. J. Maris, B. B. Rodrigues, and E. A. Veit, Phys. Rev. C **51**, 2646 (1995).

[129] T. Suda *et al.*, Phys. Rev. Lett. **102**, 102501 (2009).

[130] T. Suda *et al.*, Prog. Theor. Exp. Phys. **2012**, 03C008 (2012).

[131] K. Tsukada *et al.*, Phys. Rev. Lett. **118**, 262501 (2017).

[132] G. Kramer, H. Blok, and L. Lapikás, Nucl. Phys. A **679**, 267 (2001).

[133] T. Noro *et al.*, Journal of Physics: Conference Series **20**, 101 (2005).

[134] T. Noro, private communication.

[135] G. V. D. Steenhoven *et al.*, Nucl. Phys. A **480**, 547 (1988).

[136] A. Gade *et al.*, Phys. Rev. C **77**, 044306 (2008).

[137] J. A. Tostevin and A. Gade, Phys. Rev. C **90**, 057602 (2014).

[138] S. Kawase *et al.*, Prog. Theor. Exp. Phys. **2018**, 021D01 (2018).

[139] M. Leuschner *et al.*, Phys. Rev. C **49**, 955 (1994).

[140] Z. Y. Sun *et al.*, Phys. Rev. C **90**, 037601 (2014).

[141] E. Epelbaum, W. Glöckle, and U.-G. Meißner, Nucl. Phys. A **747**, 362 (2005).

[142] M. Kohno, Phys. Rev. C **88**, 064005 (2013).

[143] L. Elton and A. Swift, Nucl. Phys. A **94**, 52 (1967).

[144] A. Messiah, *Quantum mechanics*, Dover Books on Physics (Dover Publications, 2014).

[145] A. Shalit and I. Talmi, *Nuclear shell theory*, Pure and applied physics (Academic Press, 1963).

[146] K. Hatanaka *et al.*, Phys. Rev. Lett. **78**, 1014 (1997).

[147] T. Noro, H. Sakaguchi, H. Sakai, and T. Wakasa, *Proceedings of the rcnp international symposium on nuclear responses and medium effects* (Universal Academy Press, 1999).